ALMA MATER STUDIORUM
UNIVERSITÀ DI BOLOGNA

DEPARTMENT OF PHYSICS AND ASTRONOMY "A. RIGHI"

SECOND CYCLE DEGREE

PHYSICS

Quantum information tools at the LHC: top-quark pair studies and toponium extraction

Supervisor
Dr. Federica Fabbri

Co-supervisor
Dr. Déliot Frédéric

Defended by
Laura Antozzi

Graduation Session 03/2026

Academic Year 2024/2025

Ai miei genitori.

Abstract

This thesis explores spin correlations and quantum information observables in top quark pair production at the LHC, treating the $t\bar{t}$ system as an ideal two-qubit laboratory. A flexible framework is implemented to reconstruct the spin density matrix in $t\bar{t}$ events in multiple channels at parton level, with extension to particle-level studies for semileptonic final states. From the spin density matrix, quantum observables related to the $t\bar{t}$ system are reconstructed. The framework is then applied to investigate the sensitivity of kinematic, spin and quantum observables to toponium formation near threshold, using both event-averaged and per-event variables. Bound-state effects are found to modify the spin correlation matrix, enhancing entanglement measures while reducing quantum magic. Among per-event observables, kinematic variables provide the strongest discrimination, with the top quark momentum in the $t\bar{t}$ rest frame emerging as the most sensitive to toponium effects. A BDT combining kinematic and quantum-information-inspired variables further improves separation compared to any single observable, with QI-inspired variables providing a mild but non-negligible improvement to the separation performance. Detector-level-like cuts have been applied to the events to obtain a more realistic analysis, resulting in only a modest reduction of performance. Overall, this work establishes a solid foundation for future ATLAS and CMS measurements of quantum properties and bound-state effects in $t\bar{t}$ production.

Contents

List of Figures

List of Tables

Introduction

The top quark is the heaviest known fundamental particle. It was discovered in 1995 at Fermilab [1, 2], completing the third quark generation as the weak isospin partner of the bottom quark. With a mass of approximately 172.5 GeV, close to the electroweak symmetry breaking scale, it occupies a unique position in the Standard Model, serving as powerful probe of its internal consistency and of possible new physics. Unlike lighter quarks, it has an extremely short lifetime of about $5 \cdot 10^{-25}$ s, causing it to decay before hadronizing and ensuring that its spin information is preserved and directly encoded in the angular distributions of its decay products. This exceptional feature offers a unique opportunity to study the properties of a "bare" quark and has enabled precise measurements of top quark spin polarization and spin correlations in $t\bar{t}$ production by the ATLAS and CMS collaborations [3–7].

Most notably, these efforts recently led to the observation of quantum entanglement in top-antitop pairs at threshold by ATLAS and CMS at the LHC [8, 9], marking the highest-energy observation of entanglement to date and the first among a pair of quarks. This breakthrough establishes the $t\bar{t}$ system as an ideal two-qubit laboratory at the TeV scale and demonstrates that high-energy colliders provide a unique relativistic environment for probing fundamental aspects of quantum mechanics, opening a new research frontier at the intersection of high-energy physics (HEP) and quantum information (QI) science. This result has therefore paved the way for exploring quantum observables at colliders. Among these, quantum magic, a property of quantum states used in quantum computing to quantify the advantage of representing a state on a quantum computer rather than a classical one, has recently been measured for the first time in top quark pairs by the CMS collaboration [10].

The threshold region has received considerable attention recently in the context of quantum entanglement and has simultaneously gained renewed interest due to experimental hints [11, 12] of toponium, a $t\bar{t}$ quasi-bound state predicted by QCD. Although long thought unobservable due to the top quark's rapid decay, remnants of bound-state behaviour can still produce tiny threshold enhancements in $t\bar{t}$ spectra, which can be described using non-relativistic QCD. While the modeling of the threshold region has improved significantly [13], achieving the sensitivity needed to confirm such a state has remained challenging. This has inspired the idea of exploiting spin correlations and quantum observables to enhance sensitivity to such excesses, with theoretical studies exploring this possibility [14]. Recent measurements by the CMS [15] and ATLAS [16] collaborations, using angular observables sensitive to spin correlations and entanglement, have observed enhancements compatible with toponium, suggesting to go in this direction.

This thesis is set in this context, focusing on the study of spin correlation coefficients, entanglement and quantum magic in top quark pairs, and exploring how these observables can be used to distinguish between conventional $t\bar{t}$ production and toponium bound states. The work is structured as follows:

- Chapter 1 provides an overview of the theoretical framework and experimental context underlying this thesis work, introducing the Standard Model of particle physics and deepening the discussion for the top quark properties, its production and decay mechanisms and toponium formation, along with the main features of the LHC and the ATLAS detector relevant for the analysis.

- Chapter 2 introduces the basic concepts of quantum information relevant to this work, with a particular focus on two-qubit systems and quantum observables such as entanglement and magic in the $t\bar{t}$ context. It describes the quantum state tomography approach used to reconstruct the spin density matrix of $t\bar{t}$ pairs from their decay products and reviews the current status of spin correlations, entanglement and magic measurements in top quark pairs, including recent results on toponium.

- Chapter 3 presents the implementation of an analysis routine to reconstruct spin correlation coefficients in $t\bar{t}$ pairs from their decay products in the semileptonic and dileptonic channels, both at parton and particle level. The resulting spin density matrix is then employed to compute the quantum magic observable.

- Chapter 4 investigates whether spin and quantum observables can discriminate between standard $t\bar{t}$ production and toponium formation near threshold, building on the reconstruction of $t\bar{t}$ spin density matrix in the dilepton channel at parton level developed in Chapter 4. Both event-averaged and per-event observables are studied. The distributions of the latter are evaluated for their separation power and subsequently added to kinematic variables in a BDT to enhance sensitivity. The single variables and BDT performance is assessed using standard metrics both on the full event sample and after applying realistic event selections. The work presented in this chapter forms the core of the paper *Extracting a Toponium Signal at the LHC with Spin and Quantum Information Tools* now published on arXiv `https://arxiv.org/abs/2602.23426v1`.

1 Top quark physics at colliders

Over the course of the twentieth century, the observation of an increasing number of particles, the so-called *particle zoo*, highlighted the need for a unifying theoretical framework, ultimately leading to the formulation of the Standard Model (SM). The SM is a gauge theory that describes the electromagnetic, weak and strong interactions among elementary particles, and whose predictions have been extensively confirmed by experiments, most notably with the discovery of the Higgs boson in 2012 [17]. Within the SM, the top quark is the heaviest known elementary particle, with a mass close to the electroweak symmetry-breaking scale. Its extremely short lifetime causes it to decay before hadronization, allowing direct access to its bare-quark properties and making it a unique probe of the SM and potential physics beyond it. For this reason, precise measurements of top quark production and decay at high-energy colliders, including searches for $t\bar{t}$ bound-states, represent a central component of the current experimental program in particle physics. In this section, a brief overview of the theoretical framework and experimental context is provided, including a description of the ATLAS detector at the Large Hadron Collider (LHC) at CERN.

1.1 The Standard Model of particle physics

The SM of particle physics provides a comprehensive theoretical framework describing the fundamental constituents of matter and their interactions. Since its development, it has successfully explained numerous phenomena and has been repeatedly confirmed by precise experimental evidence. In the following, a brief introduction is presented.

1.1.1 Fundamental particles

The development of particle physics traces back to the discovery of the electron by Thomson in 1897, marking the beginning of a progressive exploration of the fundamental constituents of matter. The foundations of the quark model were established in 1964, when Murray Gell-Mann and George Zweig independently proposed that hadrons are composed of more fundamental spin-1/2 constituents, called *quarks* [18, 19]. Experimental evidence for the existence of point-like constituents inside nucleons was later provided by deep inelastic scattering experiments at SLAC in 1968 [20]. At that time, only three quark flavors, namely up (u), down (d) and strange (s), were known. The remaining quarks were discovered experimentally in the following years: the charm quark (c) in 1974 [21, 22], the bottom quark (b) in 1977 [23] and finally the top quark (t) in 1995 at Tevatron at

Fermilab (see Section 1.2), confirming the theoretical predictions.

Subsequent discoveries also in the lepton sector led to the actual SM classification, which divides all known particles into two main categories according to their spin: fermions, which have spin-1/2 and obey Fermi–Dirac statistics, and bosons, which have integer spin and obey Bose–Einstein statistics. These two classes differ fundamentally in their quantum behavior: fermions are subject to the Pauli exclusion principle, which prevents identical fermions from occupying the same quantum state, while multiple bosons can occupy the same quantum state. Fermions compose ordinary matter and are organized into two groups, quarks and leptons, both divided in three generations (or families) and grouped in doublets. For quarks,

$$\begin{pmatrix} u \\ d \end{pmatrix} \quad \begin{pmatrix} c \\ s \end{pmatrix} \quad \begin{pmatrix} t \\ b \end{pmatrix} \tag{1.1.1}$$

whereas for leptons

$$\begin{pmatrix} \nu_e \\ e \end{pmatrix} \quad \begin{pmatrix} \nu_\mu \\ \mu \end{pmatrix} \quad \begin{pmatrix} \nu_\tau \\ \tau \end{pmatrix}. \tag{1.1.2}$$

For both sectors, the corresponding antiparticles have same mass but opposite electric charge. Quarks carry fractional electric charge, either $+2/3e$ for the *up-type* quarks (u, c, t), or $-1/3e$ for the *down-type* ones, where $e = -1.60217662 \cdot 10^{19}$ C. In addition to electric charge, quarks possess two other internal charges: *flavor*, which distinguishes the six quark types (u, d, c, s, t, b) and *color charge* (red, green, blue and anti-red, anti-green, anti-blue for the anti-particles), which is responsible for the strong interaction. Leptons include three charged particles, the electron (e), muon (μ) and tau (τ), and their corresponding neutrinos (ν_e, ν_μ, ν_τ). Charged leptons have electric charge -1, while neutrinos are electrically neutral.

In addition to fermions, the SM includes several bosons which mediate the fundamental interactions: the photon (γ), 8 gluons (g) and the W^+, W^-, Z bosons act as carriers of the electromagnetic, strong and weak interactions, respectively, and are all spin-1 particles. The Higgs boson ϕ, instead, is a fundamental scalar particle (spin-0) associated with the mechanism responsible for the generation of particle masses, as briefly discussed in the next section. Among these, the only massive bosons are $W^\pm, Z, \phi$, with masses $m_W \approx 80.35$ GeV, $m_Z \approx 91.19$ GeV and $m_\phi = 125.1$ GeV, expressed in natural units ($\hbar = c = 1$). The complete particle picture is illustrated in Figure 1.1.1.

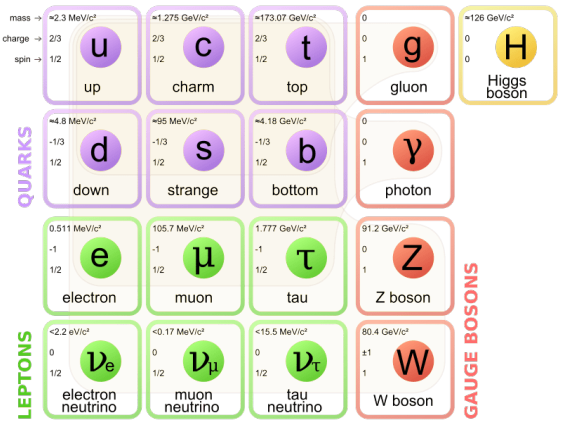

Figure 1.1.1: Scheme of the SM fundamental particles.

1.1.2 Interactions

The SM describes three of the four fundamental interactions existing in nature: strong, electromagnetic and weak, each mediated by spin-1 bosons as discussed in the previous section. Formally, it is a Quantum Field Theory (QFT) based on the gauge symmetry group

$$SU(3)_C \otimes SU(2)_L \otimes U(1)_Y \,,$$

where each group is associated with a fundamental interaction and its corresponding conserved charge. $SU(3)_C$ is a non-Abelian[1] symmetry group associated with the strong interaction, formulated in the framework of Quantum Chromodynamics (QCD). This interaction is exerted among color charges, which are carried only by quarks and gluons, and its eight generators correspond to the eight gluon fields that mediate the force. The electromagnetic and weak interactions, identified by $U(1)_Y$ and $SU(2)_L$, were unified in the 1960s by Glashow, Weinberg and Salam in the electroweak (EW) theory [24–26], based on the symmetry subgroup $SU(2)_L \otimes U(1)_Y$. The Abelian group $U(1)_Y$ is associated with the weak hypercharge Y, while the non-Abelian group $SU(2)_L$ is associated with weak isospin, whose generators are given by $I_i = \frac{\sigma^i}{2}$ $(i = 1, 2, 3)$, with σ^i being the Pauli matrices. In this framework, the electric charge Q is related to the weak isospin and hypercharge through the Gell-Mann–Nishijima relation:

$$Q = I_3 + \frac{Y}{2} \,.$$

A fundamental feature of the weak interaction is that it couples exclusively to left-handed fermions and right-handed antifermions. These terms are related to

[1] An Abelian group is a group with a commutative group operation. In contrast, non-Abelian groups have non-commuting generators, leading to self-interacting gauge bosons.

chirality, an intrinsic property of fermion fields defined by the projection operators

$$P_L = \frac{1-\gamma^5}{2}\,, \qquad P_R = \frac{1+\gamma^5}{2}\,, \tag{1.1.3}$$

where γ^5 is a Dirac matrix. These operators allow the decomposition of a fermion field ψ into its left-handed and right-handed components, as $\psi = \psi_L + \psi_R$, with $\psi_{L,R} = P_{L,R}\,\psi$. A related concept is *helicity*, defined as the projection of the particle spin $\vec{S}$ along its direction of motion $\vec{p}$, $h = \vec{S}\cdot\vec{p}/|\vec{p}|$. For massless particles, chirality and helicity coincide, while for massive particles they are distinct quantities, since helicity depends on the reference frame. The subscript L in $SU(2)_L$ reflects this chiral structure: in the SM, fermions are organised into left-handed doublets and right-handed singlets. For each generation $i = 1, 2, 3$, the quark and lepton fields are arranged as

$$\begin{aligned} Q_{L,i} &= \begin{pmatrix} u_i \\ d_i \end{pmatrix}_L\,, \qquad u_{R,i}\,, \qquad d_{R,i}\,, \\ L_{L,i} &= \begin{pmatrix} \nu_i \\ \ell_i \end{pmatrix}_L\,, \qquad \nu_{R,i}, \qquad \ell_{R,i}. \end{aligned} \tag{1.1.4}$$

Here, u_i and d_i denote the up-type and down-type quarks of the i-th generation, while ν_i and ℓ_i represent the corresponding neutrino and charged lepton. Right-handed neutrinos are not included in the SM, as they have not been experimentally observed.

The three generations of quarks and leptons, presented in Eq. 1.1.1 and Eq. 1.1.2, have identical transformation properties under the gauge symmetry group: they only differ in their masses, which arise from the Brout-Englert-Higgs (BEH) mechanism [27]. Through spontaneous breaking of the $SU(2)_L \otimes U(1)_Y$ symmetry down to $U(1)_{\text{em}}$, which represents the residual gauge symmetry of electromagnetism associated with the electric charge Q, the Higgs field acquires a vacuum expectation value $v \approx 246$ GeV, generating masses for fermions via Yukawa couplings,

$$m_f = \frac{y_f\, v}{\sqrt{2}}\,, \tag{1.1.5}$$

where y_f is the Yukawa coupling constant specific to each fermion. The $W^\pm$ and Z boson masses are generated through the same mechanism, giving

$$m_W = \frac{g\, v}{2}\,, \qquad m_Z = \frac{\sqrt{g^2 + g'^2}\, v}{2}\,, \tag{1.1.6}$$

where g and g' are the $SU(2)_L$ and $U(1)_Y$ gauge coupling constants, respectively. The photon and gluons remain massless, as required by the unbroken $U(1)_{\text{em}}$ and $SU(3)_C$ symmetries.

Among the SM particles, quarks interact via all forces, charged leptons via weak and electromagnetic interactions, while neutrinos only weakly. The relative strength and range of each force is illustrated in Table 1.

Interaction	Relative strength	Range (m)	Mediator
Strong	1	10^{-13}	gluons (8)
Electromagnetic	10^{-2}	∞	photon (1)
Weak	10^{-5}	$< 10^{-15}$	$W^{\pm}, Z$ (3)

Table 1: Relative strength and range of the Standard Model interactions.

For the purpose of this thesis, the strong and weak interactions are the most relevant ones, playing a central role in the production and decay of the top quark at colliders. Their dynamics are encoded in the corresponding terms of the SM Lagrangian. Specifically, the QCD Lagrangian reduced to quark terms is given by

$$\mathcal{L}_{\text{QCD}} = \sum_{q} \bar{\psi}_{q,a}(i\gamma^{\mu} D_{\mu} - m_q)\psi_{q,b} \tag{1.1.7}$$

where $\psi_{q,a}$ is a quark field spinor of color index a and $D_{\mu} = \partial_{\mu} + ig_S T^a G^a_{\mu}$ is the covariant derivative, with G^a_{μ} being the gluon fields and T^a the generators of $SU(3)_C$. The gauge coupling between the quarks and gluons is given by g_S, which is related to the strong coupling constant α_S by $g_S = 4\pi\alpha_S$. An important feature of this parameter is its scale dependence, which determines the main characteristics of the strong interaction. In particular, α_S depends on the squared momentum transfer Q^2 of the process, leading to two opposite regimes:

- *asymptotic freedom*: at large momentum transfer ($Q^2 \gg \Lambda_{QCD}$, where $\Lambda_{QCD} \sim 10^2$ MeV denotes the QCD scale parameter), $\alpha_S(Q^2)$ tends to zero and the quarks behave as quasi-free particles. This property allows QCD to be treated perturbatively at high energies, as in hadron collider processes;

- *confinement*: at low exchanged momentum ($Q^2 \to 0 \Rightarrow \alpha_S \to \infty$), the strong interaction becomes non-perturbative. Quarks and gluons cannot exist as free asymptotic states, but are confined into color-neutral combinations (color singlets), called *hadrons*, which are classified as *baryons* (qqq) and *mesons* ($q\bar{q}$). As a consequence, direct observation of isolated colored particles is not possible. In high-energy scattering processes, the formation of colorless hadrons from colored quark constituents is called *hadronization*.

This behavior of the strong coupling constant is due to the non-Abelian nature of the $SU(3)_C$ symmetry group, which implies the presence of self-interaction among the gluons.

Considering now the weak interaction part, the relevant term is given by the charged current (CC) interaction Lagrangian

$$\mathcal{L}_{CC} = -\frac{g}{\sqrt{2}}(\bar{u}_L^i V_{\text{CKM}}^{ij} d_L^j) W_\mu^+ + \text{h.c.} \tag{1.1.8}$$

where $u_i = (u, c, t)$ and $d_j = (d, s, b)$. Here, g is the weak coupling constant and V_{CKM} is the 3×3 Cabibbo–Kobayashi–Maskawa (CKM) unitary matrix [28, 29] describing the mixing between quark families in CC interactions, defined as

$$V_{\text{CKM}} = \begin{pmatrix} V_{ud} & V_{us} & V_{ub} \\ V_{cd} & V_{cs} & V_{cb} \\ V_{td} & V_{ts} & V_{tb} \end{pmatrix} \tag{1.1.9}$$

Specifically, the quantity $|V_{ij}|^2$ is proportional to the probability (or branching fraction) for a flavour-u_i quark to decay into a flavour-d_j quark via a $W^\pm$ boson.

In QFT, interactions are conveniently described through Feynman diagrams, which provide a systematic way to compute the transition probability between initial and final states. In these diagrams, time flows along the horizontal axis, straight lines represent fermions and wavy or curly lines represent bosons; arrows pointing in the positive (negative) time direction denote fermions (antifermions). Each vertex corresponds to an interaction, and contributes a factor $\sqrt{\alpha} \propto g$ to the amplitude, where g is the coupling constant of the interaction. The transition probability is proportional to the square of the total amplitude, obtained by summing over all diagrams contributing to a given process. Since each additional vertex introduces a further power of α, diagrams with more vertices or loops are suppressed with respect to simpler ones. In perturbation theory, where $\alpha < 1$, one therefore truncates this expansion at a given order: including only the lowest-order diagrams defines the leading-order (LO) approximation, with higher-order corrections improving the precision of the calculation. Examples of Feynman diagrams specific to the top quark will be given in Section 1.2.2.

1.2 Top quark physics

The top quark belongs to the third generation of quarks, whose existence was predicted by Kobayashi and Maskawa in 1973 [29] to account for CP violation in weak interactions. The top quark was discovered in 1995 at the Fermilab Tevatron collider by the CDF and DØ collaborations, thereby completing the quark sector of the Standard Model. At the Tevatron, protons and antiprotons were collided at a center of mass energy $\sqrt{s} = 1.8$ TeV, with the two experiments searching for top–antitop pair production and their subsequent decays. The reconstructed invariant mass of the top candidates, obtained independently by CDF and DØ, showed clear excesses consistent with a heavy quark, with measured masses of $176 \pm 8(\text{stat}) \pm 10(\text{syst})$ GeV [2] and $199^{+19}_{-21}(\text{stat}) \pm 22(\text{syst})$ GeV [1] respectively. These results constituted the first top quark mass measurement in history. In the following sections, top quark properties, together with its production and decay mechanisms, are presented.

1.2.1 Top quark properties

The top quark is the heaviest known fundamental particle in the SM. Its mass has been measured with high precision to be

$$m_t = 172.52 \pm 0.14\,(\text{stat}) \pm 0.30\,(\text{syst})\,\text{GeV}$$

according to the most recent combined results from the ATLAS and CMS measurements [30]. This exceptionally large mass determines to a large extent the unique phenomenology of this quark. Because its mass exceeds that of the W boson, the top quark is the only quark that decays via weak interaction into an on-shell W boson and a down-type quark. The dominant mode is $t \to Wb$, with a branching fraction for this process given by

$$B_{tW} = \frac{|V_{tb}|^2}{|V_{tb}|^2 + |V_{ts}|^2 + |V_{td}|^2} \tag{1.2.1}$$

where $V_{tq}(q = d, s, b)$ denote the relevant elements of the CKM matrix (Eq.1.1.9). Given that $|V_{tb}| \approx 0.998 \gg |V_{ts}|, |V_{td}|$, this branching fraction is close to unity, making $t \to Wb$ essentially the exclusive decay channel of the top quark. As a consequence, this particle has an extremely short lifetime $\tau \approx 5 \cdot 10^{-25}$ s, corresponding to a decay width of $\Gamma_t = 1.42^{+0.19}_{-0.15}$ GeV [30] (with $\tau = \hbar/\Gamma$). This lifetime is significantly shorter than two characteristic timescales: the timescale of hadronisation ($\sim 10^{-23}$ s) and the one of spin-decorrelation ($m_t/\Lambda^2_{QCD} \sim 10^{-21}$). The first property implies that the top quark decays before forming bound hadronic states, although non-relativistic QCD interactions near the $t\bar{t}$ production threshold can give rise to toponium-like effects (see Section 1.2.4). The second one determines

that it decays well before the strong interaction could alter its spin properties, ensuring that the spin information of the top quark is directly transferred to its decay products. As a result of these unique features and thanks to its abundant production at the LHC, the top quark provides direct access to its fundamental properties with unprecedented experimental precision.

In addition, the top quark mass m_t is a fundamental parameter of the SM. From Eq. 1.1.5, its large value implies a Yukawa coupling to the Higgs boson close to unity ($y_t \approx 1$), suggesting a deep connection between this particle and electroweak symmetry breaking and offering sensitivity to possible effects of physics beyond the Standard Model. Furthermore, through radiative corrections, m_t affects the theoretical prediction of the W boson mass and a combined measurement of m_W and m_t allows to constrain the Higgs boson mass and, after its discovery, to test the global consistency of the SM. Moreover, the stability of the electroweak vacuum is highly sensitive to the precise value of m_t, as it determines whether the SM vacuum is stable, metastable or unstable up to the Planck scale.

Given the central role of the top quark mass in both its phenomenology and the internal consistency of the SM, its precise determination has been a primary objective of the experimental programs of the ATLAS and CMS collaborations.

1.2.2 Top quark production in hadron colliders

In hadron colliders, protons (and antiprotons), which are composite objects made of quarks and gluons, are accelerated to very high energies and brought into collision. At these scales, asymptotic freedom ensures that collisions do not occur between the hadrons as a whole, but rather between their constituents partons, which behave as quasi-free particles. These partons undergo a *hard scattering* process, which is defined as a short-distance interaction at large momentum transfer $Q^2 \gg \Lambda^2_{\text{QCD}}$ and can be calculated using perturbative QCD. Given that the timescale of the hard interaction is well separated from the subsequent hadronization timescale, the total cross section of the process $pp \to X$ can be factorised into a perturbatively calculable partonic cross section $\hat{\sigma}_{ab\to X}$ and the non-perturbative Parton Distribution Functions (PDFs) [31], as

$$\sigma_{p^A\, p^B \to X} = \sum_{a,b} \int dx_a\, dx_b\, f_{a/A}(x_a, Q^2)\, f_{b/B}(x_b, Q^2)\, \hat{\sigma}_{ab\to X}\,, \tag{1.2.2}$$

where $f_{a/A}(x_a, Q^2)$ gives the probability of finding parton a carrying a momentum fraction x_a of the proton p^A at a scale Q^2. This process is illustrated in Figure 1.2.1, which also reports the gluon and valence quark (u, d for the proton) PDFs obtained by measurements at different colliders. The PDFs reflect the underlying dynamic structure of the proton, where gluons and sea quarks are continuously

generated through QCD processes. In particular, QCD interactions among valence quarks lead to the emission of gluons, typically softer than the emitting quark, which can further split into $q\bar{q}$ pairs populating the proton with a dense sea of partons carrying small momentum fractions, thus increasing the probability of finding a parton at low x. This is evident from Figure 1.2.1 (right panel), where gluon and sea quarks contribution dominates at low x, while the valence quarks peak around $x \approx 1/3$. When increasing the energy scale, the gluon and sea quark distributions grow significantly at small x due to enhanced parton radiation and gluon splitting processes. The PDFs are extracted from experimental data and are process-independent.

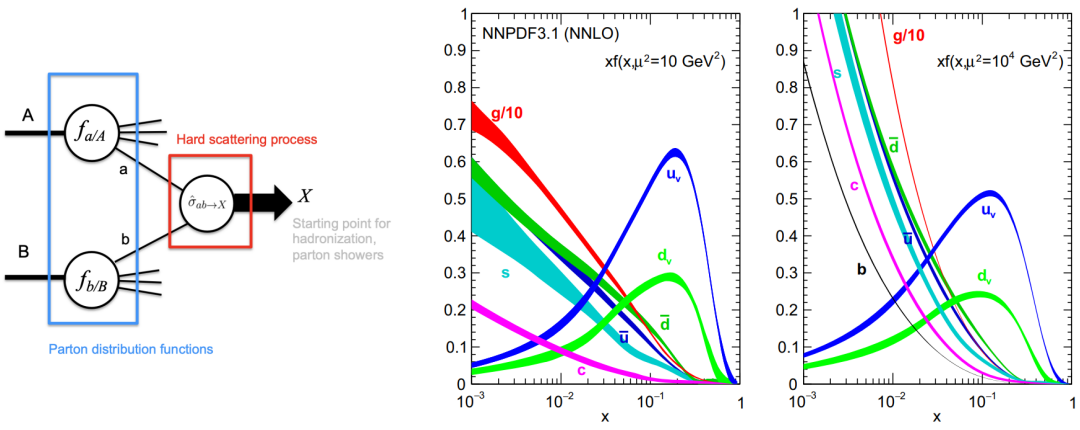

Figure 1.2.1: Illustration of an hard scattering process (left). Quark and gluon PDFs of the proton at two different energy scales, obtained by the NNPDF collaboration using measurements performed at several collider experiments [32] (right).

Following the hard scattering, outgoing and incoming partons radiate gluons via bremsstrahlung, which in turn emit further radiation, generating *parton showers*. These showers represent higher-order corrections to the hard process, primarily associated with soft and collinear gluon emissions, and can occur both in the initial and final state. As the shower evolves and the energy scale decreases, perturbative calculations are no longer applicable and the system enters the non-perturbative regime of hadronization.

In hadron colliders, top quarks are produced either in $t\bar{t}$ pairs via the strong interaction or as single top quarks via electroweak interactions. Among these mechanisms, top quark pair production represents the dominant mode at both the Tevatron and the LHC. At leading order (LO) in perturbative QCD, $t\bar{t}$ pairs can be produced either via quark-antiquark annihilation ($q\bar{q} \to t\bar{t}$) or gluon-gluon fusion ($gg \to t\bar{t}$). The corresponding Feynman diagrams for these processes are

shown in Figure 1.2.2.

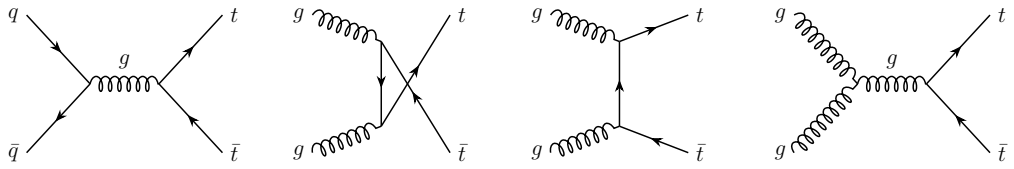

Figure 1.2.2: Representative LO diagrams for the $t\bar{t}$ pair production at the LHC. From left to right: $q\bar{q}$ annihilation, gluon fusion in the u, t, s-channels.

The relative contribution of the $t\bar{t}$ production modes is governed by the PDFs inside the colliding hadrons and therefore depends both on the collider type and the center-of-mass energy. At the Tevatron, a proton-antiproton ($p\bar{p}$) collider operating at $\sqrt{s} = 1.96$ GeV, valence quark-antiquark annihilation accounts for approximately 85% of $t\bar{t}$ production cross section. In contrast, at the LHC, where pp collisions take place at significantly higher energies, most of the production involves sea partons and the dominant contribution arises from gluon-gluon fusion. In particular, gluon-induced processes produce about 90% $t\bar{t}$ pairs at $\sqrt{s} = 13$ TeV.

Accurate predictions of the $t\bar{t}$ production cross section require the inclusion of higher-order corrections in perturbative QCD, beyond the LO diagrams. Table 2 reports the theoretical prediction at next-to-next leading order (NNLO) of the $t\bar{t}$ pair production cross-section and the measured value for various center-of-mass energies, as obtained by the ATLAS and CMS collaborations in different analyses.

$\sqrt{s}$	Predicted $\sigma_{t\bar{t}}$ [pb]	Measured $\sigma_{t\bar{t}}$ [pb]
7 TeV	$179.6^{+9.5}_{-10.2}$	178.5 ± 4.7 (combined)
8 TeV	$256^{+12.9}_{-14.0}$	$243.3^{+6.0}_{-5.9}$ (combined)
13 TeV	$832^{+37.4}_{-43.0}$	$830 \pm 0.4\,(\text{stat}) \pm 36\,(\text{syst}) \pm 14\,(\text{lumi})$

Table 2: Summary of selected $t\bar{t}$ production cross section measurements by ATLAS and CMS compared with theoretical predictions at NNLO, including soft-gluon resummation to next-to-next-to-leading-log order [33], obtained assuming $m_{\text{top}} = 172.5$ GeV. Uncertainties on the predictions include scale, PDF and mass contributions. *Combined* refers to the legacy combined cross section measured by ATLAS and CMS [34]. The measurement at 13 TeV is performed by ATLAS and uses a Run 2 dataset corresponding to an integrated luminosity of 139 fb^{-1} [35].

A detailed summary of ATLAS and CMS $t\bar{t}$ cross section measurements at $\sqrt{s} = 13$ TeV using different decay channels (see Section 1.2.3) is illustrated in Figure 1.2.3.

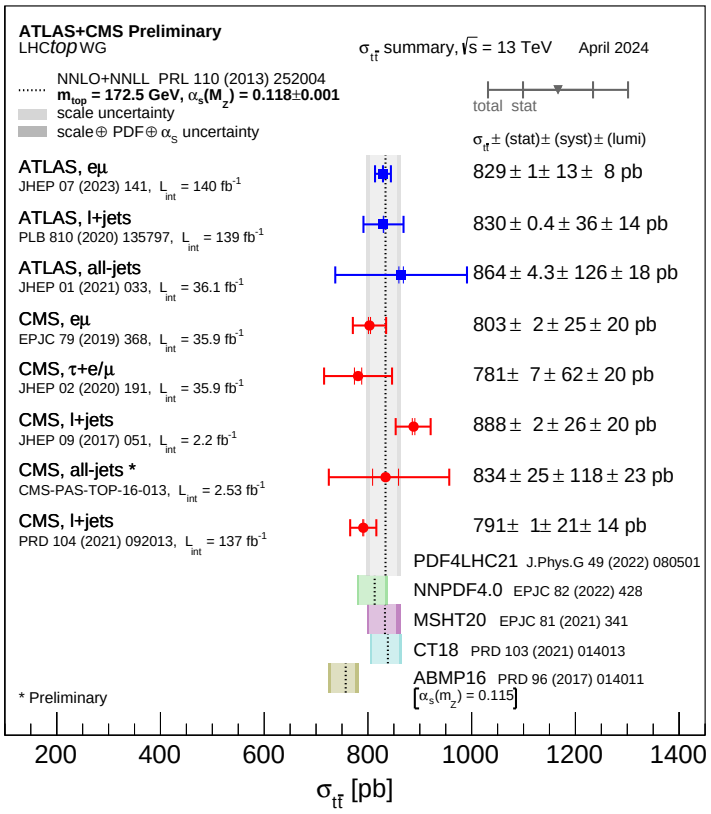

Figure 1.2.3: Summary of measurements of the $t\bar{t}$ production cross section at 13 TeV compared to the exact NNLO QCD calculation complemented with NNLL resummation [33], with the gray band representing theoretical uncertainties. The calculations assume $m_t = 172.5$ GeV [36].

Compared to $t\bar{t}$ pair production, single top quark production occurs at a lower rate because it is governed by the smaller electroweak coupling ($\alpha_{EW} \ll \alpha_S$), resulting in an overall suppression of roughly a factor of three. It proceeds via the exchange of virtual W bosons in the s- and t-channels, or via W-associated production (Wt). The corresponding Feynman diagrams at LO are shown in Figure 1.2.4.

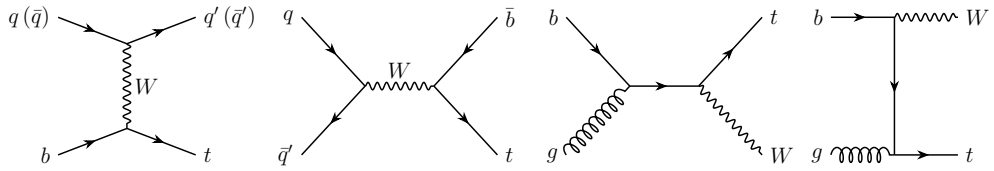

Figure 1.2.4: Representative LO diagrams for single top quark production at the LHC. From left to right: t-channel, s-channel and tW associated production.

Among these processes, the t-channel is kinematically favored and provides the largest cross section at both the Tevatron and the LHC. At LHC energies, the tW-channel represents the second most significant contribution. However, this process also constitutes an important background in measurements of the $t\bar{t}$ cross section, as its final state closely mimics that of $t\bar{t}$ events. This is worsened by the fact that the NLO diagrams for tW production are identical to the LO $t\bar{t}$ production ones. Several methods have been developed to correctly account for the overlap between these diagrams in NLO σ_{tW} calculation [37].

1.2.3 Top quark pair decay

The dominant decay mode of the top quark is into a W boson and a bottom quark ($t \to Wb$), with a branching fraction BR_{tW} very close to unity (see Section 1.2.1). Therefore, $t\bar{t}$ decay events can be classified according to the decay modes of the two W bosons from the top and antitop quarks:

- *Di-leptonic* (BR: 10.5%): both W bosons decay leptonically into a charged lepton and a neutrino ($t\bar{t} \to W^+bW^-\bar{b} \to l^+\nu b l^-\bar{\nu}\bar{b}$). The detector signature of this channel consists of two high-p_T isolated leptons, two jets originating from b-quark hadronization and significant missing transverse energy due to the presence of two neutrinos, which escape detection. Owing to the presence of two charged leptons, this channel offers a clean experimental signature and allows for efficient discrimination of the signal from background processes.

- *All-hadronic* (BR: 45.7%): both W bosons decay hadronically into quark–antiquark pairs ($t\bar{t} \to W^+bW^-\bar{b} \to q\bar{q}'bq\bar{q}'\bar{b}$), producing only jets in the final state. Therefore, the detector signature of this channel consists of six jets arising from the hadronization of the quarks, including two b-tagged jets. Despite having the largest branching fraction, this channel suffers from a poor signal-to-background ratio due to the overwhelming contribution from multijet QCD background, making the discrimination of $t\bar{t}$ events particularly challenging.

- *Semi-leptonic* (BR: 43.8%): one W boson decays leptonically, the other decays hadronically ($t\bar{t} \to W^+bW^-\bar{b} \to q\bar{q'}bl^-\bar{\nu}\bar{b}$ or $l^+\nu bq\bar{q'}\bar{b}$). The detector signature of this channel consists of one high-p_T, isolated lepton, significant missing transverse energy due to the neutrino and four jets originating from quark hadronization, including two b-tagged jets. This is often referred to as the *golden channel*, since the presence of a charged lepton allows for efficient event triggering and effective discrimination of the signal from the multi-jet background, while maintaining a high event statisics. Furthermore, the presence of a single neutrino enables a full reconstruction of the event kinematics by imposing the W-boson mass constraint on the lepton-neutrino system. The branching ratio of this channel is reducedy by $\sim 15\%$ when considering only final states with μ or e.

The dileptonic and semileptonic decay modes are illustrated in Figure 1.2.5.

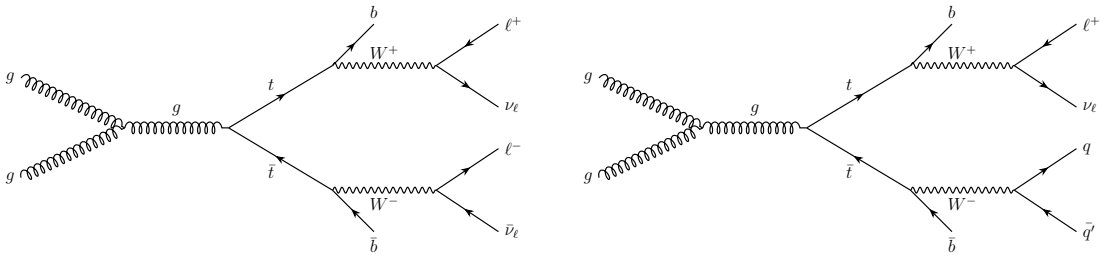

Figure 1.2.5: Feynman diagrams at LO for the dileptonic (a) and semileptonic (b) channels after $t\bar{t}$ production via gg fusion.

1.2.4 Toponium

The formation of toponium, a quasi-bound state of a top and an antitop quark, was predicted by Fadin and Khoze [38] long before the top quark discovery, studying $t\bar{t}$ pair production near the energy threshold in e^+e^- collisions.

The concept of *quarkonia*, bound states of a heavy quark and its antiquark held together by the strong force, has played a central role in establishing QCD as the theory of the strong interaction, with the discoveries of charmonium ($c\bar{c}$, the J/Ψ) in 1974 [21, 22] and of bottomonium ($b\bar{b}$, the Υ) in 1977 [23] providing some of the earliest and most compelling confirmations of its predictions, revealing the existence of the fundamental particles c and b. These states appear as sharp, narrow resonances in the invariant mass spectrum of their decay products, with well-defined masses, quantum numbers and decay widths that can be predicted by QCD. By analogy, a $t\bar{t}$ bound state was expected to be the heavy counterpart of

these systems, classified as any other meson ($q\bar{q}$) through a specific set of quantum numbers. Since both the top quark and the antitop quark have spin 1/2, their spins can combine either into a singlet configuration with $S = 0$ (anti-aligned spins) or into a triplet configuration with $S = 1$ (aligned spins). Combined with the orbital angular momentum L, the state is characterized by the total angular momentum $J = L + S$, parity $P = (-1)^{L+1}$ and charge conjugation $C = (-1)^{L+S}$, collectively denoted as J^{PC}. In particular, for S-wave states ($L = 0$), one simply has $J = S$ and the possible toponium states can be classified as:

- η_t: the spin-singlet $^1S_0$ state ($S = 0$, $J = 0$), with $J^{PC} = 0^{-+}$, corresponding to a pseudoscalar meson;
- Θ_t: the spin-triplet $^3S_1$ state ($S = 1$, $J = 1$), with $J^{PC} = 1^{--}$, corresponding to a vector meson, analogous to the J/Ψ and the Υ.

In addition to the spin quantum numbers, the $t\bar{t}$ system can also exist in different color configurations. In analogy with the spin singlet and triplet, the two quarks can form either a color-singlet state, carrying no net color charge, or a color-octet state. At the LHC, $t\bar{t}$ production proceeds predominantly via gluon fusion. Near the production threshold, the lowest-energy configuration ($L = 0$) dominates, making the pseudoscalar color-singlet η_t state the most relevant in this region, as can be seen by Figure 1.2.6.

The top quark, however, differs fundamentally from the charm and bottom quarks. Owing to its very large mass, its extremely short lifetime causes it to weakly decay ($t \to Wb$) well before the strong interaction has time to form a stable bound state (Section 1.2.1). The corresponding large decay width, $\Gamma_t \sim 1$ GeV, acts as a natural smearing of the would-be sharp toponium resonance, preventing the formation of narrow resonances as observed in charmonium and bottomonium systems. Nevertheless, it has been recognized that near-threshold dynamics remain governed by non-relativistic QCD (NRQCD) [13, 40, 41], and remnants of the bound-state behavior, such as threshold enhancements and quasi-resonant structures, can persist even in the presence of the top quark's rapid decay. An excess of events in the near-threshold region with respect to fixed-order perturbative QCD predictions would therefore constitute the experimental signature of toponium. For a long time, these effects have been considered unobservable at hadron colliders, with expected contributions to the $t\bar{t}$ production cross section accounting for less than 1% [13], as shown in Table 3, and a width well below the current achievable resolution. Moreover, the difficult modeling of the threshold region has made their experimental observation even more challenging.

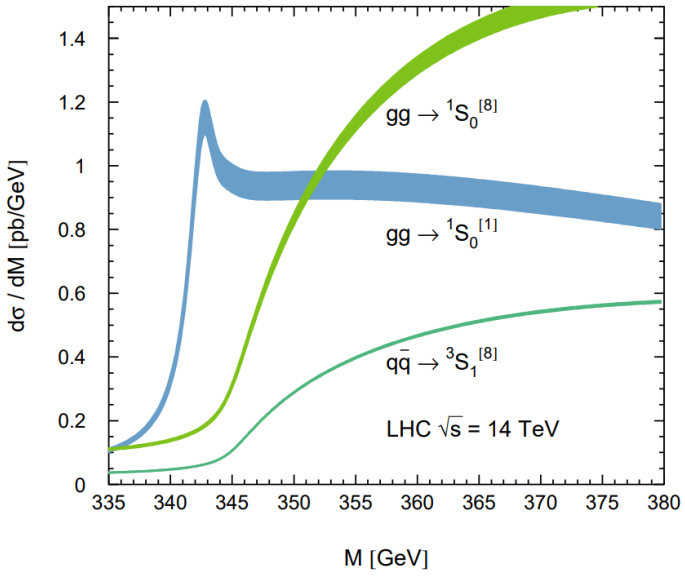

Figure 1.2.6: Differential $t\bar{t}$ production cross section as a function of the invariant mass M near threshold at the LHC at $\sqrt{s} = 14$ TeV. Shown are the color-singlet gluon fusion contribution $gg \to {}^1S_0^{[1]}$ (blue), the color-octet gluon fusion contribution $gg \to {}^1S_0^{[8]}$ (dark green), and the $q\bar{q} \to {}^3S_1^{[8]}$ contribution (light green) [39].

$\sqrt{s}$	σ_{η_t} (pb)	$\sigma_{t\bar{t}}$ (pb)	$\sigma_{\eta_t}/\sigma_{t\bar{t}}$
7 TeV	1.55	172	0.0090
8 TeV	2.19	246	0.0089
13 TeV	6.43	810	0.0079
14 TeV	7.54	954	0.0079

Table 3: Cross sections for η_t and $t\bar{t}$ production at different LHC center-of-mass energies $\sqrt{s}$ [42].

However, in the last years, excesses at threshold in several distribution of $t\bar{t}$ events by have been observed by the ATLAS and CMS collaborations, which could be consistent with toponium formation. Representative distributions are shown in Figure 1.2.7. Recently, observations by the same collaborations have provided the first indications of cross section enhancements compatible with the production of a color-singlet pseudoscalar toponium state. These results will be discussed in Section 2.5.7, as they are associated to the spin correlations of the top and anti-top quarks at threshold. Moreover, recent theoretical developments in modeling $t\bar{t}$ production near threshold, including NRQCD-based calculations [13], offer a more accurate description of bound-state effects than previous simplified models, improving the prospects for experimentally observing toponium resonances.

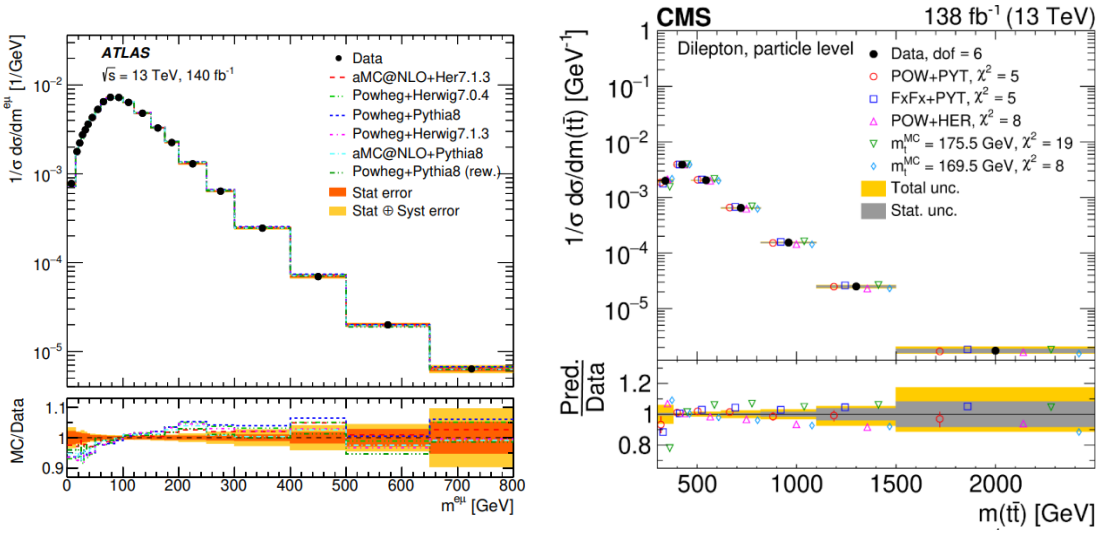

Figure 1.2.7: Normalised differential cross-sections as a function of the invariant mass $m_{e\mu}$ and $m_{t\bar{t}}$ as measured, respectively, by the ATLAS [12] (left) and CMS [11] (right) collaborations. It presents the evidence for excesses at threshold.

1.3 The LHC

The Large Hadron Collider (LHC) is the world's largest and most powerful particle accelerator, built at CERN (European Organization for Nuclear Research), the international laboratory for particle physics founded in 1954 and located on the Franco-Swiss border near Geneva. The LHC is installed in the 26.7 km circumference tunnel previously hosting the Large Electron Positron collider (LEP), approximately 100 m underground.

The LHC is a two-ring hadron collider in which two proton beams circulate in opposite directions, designed to reach center-of-mass energies of $\sqrt{s} = 14$ TeV, with a peak instantaneous luminosity of $\mathcal{L} = 10^{34}$ cm^{-2}s^{-1} (Eq.1.3.1). First operational in November 2009, it ran at $\sqrt{s} = 7$ and 8 TeV until 2012. After a major upgrade, it resumed operation in 2015 at $\sqrt{s} = 13$ TeV, with the highest energy achieved to date being 13.6 TeV during Run 3. The acceleration of protons to full energy is performed in stages. In particular, before entering the LHC pipes, the beams are accelerated up to 450 GeV by a chain of injectors, illustrated in Figure 1.3.1: the Linear accelerator 4 (Linac4), the Proton Synchrotron Booster (PSB), the Proton Synchrotron (PS) and the Super Proton Synchrotron (SPS). The LHC acceleration system consists of of 16 superconducting radiofrequency cav-

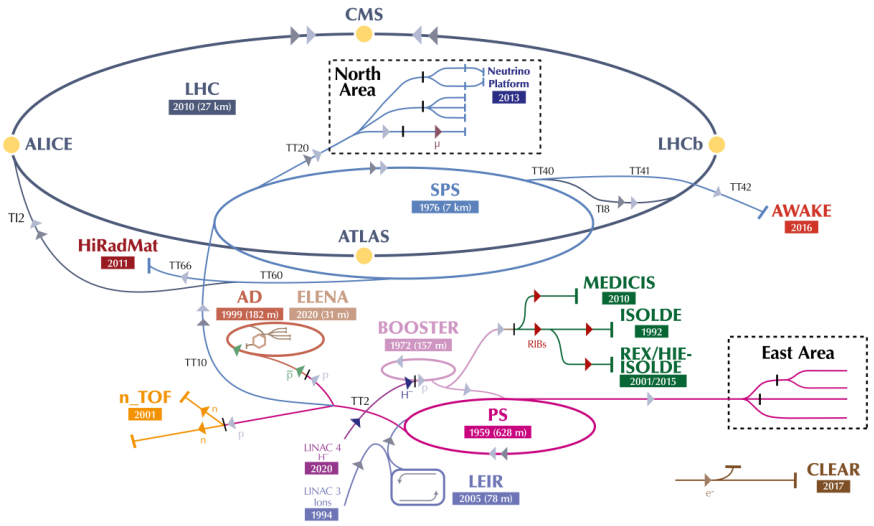

Figure 1.3.1: Illustration of the CERN complex, showing the LHC accelerator injection chain and experiments.

ities providing a maximum electric field of 5.5 MV/m. Given an effective bending radius of approximately 2.7 Km, the nominal LHC operation requires a magnetic field of about 8.5 T to keep the proton beams on their circular trajectory. This is provided by 1232 superconducting dipole magnets, each 15 m long and operating

at 1.9 K, while beam focusing is performed by 392 superconducting quadrupole magnets, $5 - 7$ m long and producing a field of 6.8 T.

The two colliding beams are brought into collision at four interaction points (IPs), each hosting a major experiment: **ATLAS** (A Toroidal LHC ApparatuS) and **CMS** (Compact Muon Solenoid) are general-purpose detectors designed to perform precise SM measurements and search for new physics; **LHCb** (Large Hadron Collider beauty) is optimised for flavour physics and CP-violation studies in b- and c-hadron decays; **ALICE** (A Large Ion Collider Experiment) is dedicated to the study of the quark-gluon plasma in heavy-ion collisions.

At each IP, the two beams collide inside special X-shaped beam pipes, with a crossing angle of approximately 1.5°. The number of events per second generated in the collision is given by the rate $R = \mathcal{L}\,\sigma$, where σ is the cross section of the process under study and $\mathcal{L}$ is the instantaneous luminosity. The latter depends only on the beam parameters and is given by

$$\mathcal{L} = \frac{N_b^2\, n_b\, f_{\text{rev}}\, \gamma}{4\pi\, \epsilon\, \beta^*} F\,, \tag{1.3.1}$$

where N_b is the number of particles per bunch ($\approx 10^{11}$ protons), n_b the number of bunches per beam, $f_{\text{rev}} = 11.25$ kHz the LHC revolution frequency, γ the relativistic factor, ϵ the normalised transverse beam emittance, β^* the beta function at the collision point and F a geometric reduction factor accounting for the crossing angle between the two beams. In particular, the emittance is related to the beam quality, while β^* is a beam optics quantity that characterizes how strongly the quadrupole magnets focus the beam at the IP. Together with γ_r, they are related to the beam width σ_b at the IP by $\sigma_b = \beta^*\epsilon/\gamma$. The total amount of data collected over a period of time is quantified by the integrated luminosity $L = \int \mathcal{L}\, dt$, which determines the total number of events produced for a process with cross section σ via $N = L\,\sigma$.

1.3.1 The ATLAS Detector

This section presents the ATLAS a general-purpose particle detector, designed to reconstruct a wide variety of physics processes generated from pp collisions, performing precise SM measurements and searching for new physics. It is described as the analysis-like selections applied to $t\bar{t}$ final states in Chapter 3 are designed to match the acceptance requirement of this detector.

With a total length of 42 m, a radius of 11 m and a weight of approximately 7000 tons, ATLAS is the largest experiment at the LHC. It features a forward-backward symmetric cylindrical geometry, nearly full 4π coverage in solid angle, and is designed to operate under the high pile-up and luminosity conditions of the LHC.

Coordinate system To describe the detector geometry and define selection criteria used in analyses, a right-handed coordinate system $\{x, y, z\}$ is adopted, with its origin at the pp interaction point. The z-axis is oriented along the beam direction, while (x, y) plane defines the transverse plane with respect to the beam. The component of the particle's momentum $\vec{p}$ within the (x, y) plane is called *transverse momentum* p_T, defined as $p_T = \sqrt{p_x^2 + p_y^2}$. The angle between $\vec{p}$ and the beam direction is the polar angle θ, with $0 \leq \theta \leq \pi$. The azimuthal angle ϕ is instead defined as the angle between p_T and the x axis within the transverse plane. Instead of the polar angle, analyses commonly use the pseudorapidity, defined as

$$\eta = -\ln \tan\left(\frac{\theta}{2}\right). \tag{1.3.2}$$

Small variations in θ near the beam axis correspond to large changes in η, making pseudorapidity a convenient variable for describing particle production at small polar angles. A schematic representation of the coordinate system used in the ATLAS detector, together with pseudorapidity for various polar angles, is shown in Figure 1.3.2. Finally, ΔR represents the angular separation between two particles

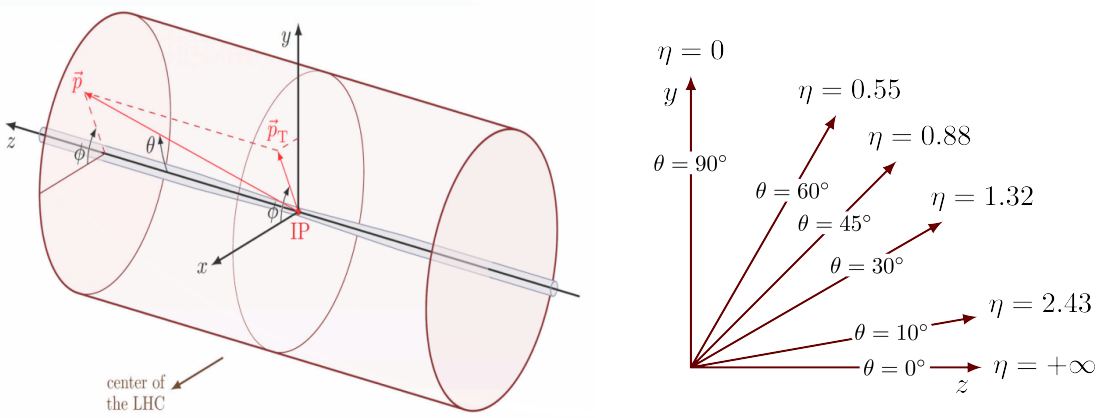

Figure 1.3.2: Illustration of the coordinate system used in the ATLAS detector (left) and pseudorapidity values shown on a polar plot (right).

in the $(\eta - \phi)$ plane. It is defined as $\Delta R = \sqrt{(\Delta\eta)^2 + (\Delta\phi)^2}$, where $\Delta\eta$ and $\Delta\phi$ denote the differences in pseudorapidity and azimuthal angle, respectively. The quantity ΔR is commonly used to define clustering cones in jet reconstruction algorithms.

As shown in Figure 1.3.3, ATLAS consists of several sub-detectors [43], each designed to perform specific functions in reconstructing the different particles that pass through the detector. Moving radially outward from the interaction point, the following components are encountered:

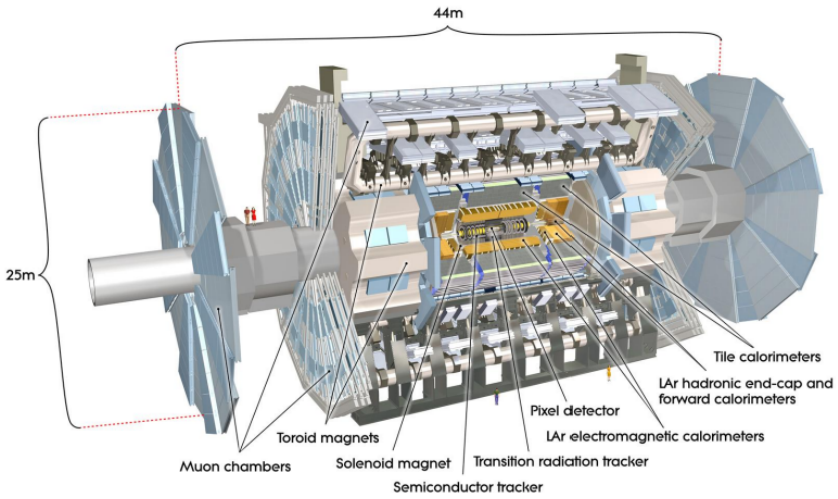

Figure 1.3.3: Overview of the ATLAS detector.

- The inner tracking detector (ID), immersed in a 2 T axial magnetic field provided by a thin superconducting solenoid, covers the pseudorapidity range $|\eta| < 2.5$ and is composed of a silicon pixel detector, a silicon microstrip tracker and a transition radiation tracker. The magnetic field bends the trajectories of charged particles, allowing precise determination of their momentum from the measured curvature. The fine spatial granularity of the silicon detectors provides impact parameter resolutions at the level of $\sim 10\,\mu$m, enabling precise reconstruction of charged-particle tracks and primary and secondary vertices. This feature is essential for identifying displaced decay vertices from heavy-flavour hadrons. The fiducial region $|\eta| < 2.5$ therefore defines the optimal acceptance for precise reconstruction of charged particles, motivating the pseudorapidity requirements applied to the final-state objects described in Section 4.1.1;

- the calorimeter system covers $|\eta| < 4.9$ and measures the energy deposited by particles through electromagnetic and hadronic showers. It is essential for reconstructing electrons, photons and jets, as well as for measuring missing transverse energy $E_{\mathrm{T}}^{\mathrm{miss}}$, which provides indirect evidence for neutrinos. It is divided into two subsystems, both sampling detectors composed of alternating absorber and active layers, optimised for the two distinct types of particle showers:

  - The electromagnetic calorimeter (ECal) is designed to contain EM showers, initiated by electrons and photons, characterised by a compact longitudinal and transverse profile. It uses lead absorber and liquid-argon

(LAr) active medium, covering $|\eta| < 3.2$ over the full azimuth, complemented by a presampler up to $|\eta| < 1.8$ to recover energy lost upstream. It achieves a sampling term of $\sim 10\%/\sqrt{E}$[2] and a constant term well below 1%, providing excellent resolution for charged leptons and photons.

– The hadronic calorimeter (HCal) consists of three subsystems: the central tile calorimeter ($|\eta| < 1.7$, steel/scintillator), the hadronic end-cap calorimeter (HEC, $|\eta| < 3.2$, copper/LAr) and the forward calorimeter (FCal, $3.1 < |\eta| < 4.9$, copper and tungsten absorbers). It is designed to contain hadronic showers, which develop over much larger distances and involve more complex interactions, allowing the HCal to achieve a significantly worse jet energy resolution of $\sigma_E/E = 40\%/\sqrt{E} \oplus 2.5\% \oplus 5\%/E$.

Jets are reconstructed by combining ECal and HCal deposits, but they suffer from limited resolution with respect to charged leptons and photons; flavor tagging exploits ID tracking to identify b- and c-quark jets via displaced vertices. Up to date, no flavor-tagging algorithms exist for light quarks (u, d, s), whose jets remain experimentally indistinguishable.

- The muon spectrometer (MS), based on superconducting air-core toroidal magnets providing a field integral of 2.0-6.0 T·m, with precision tracking up to $|\eta| < 2.7$ and triggering up to $|\eta| < 2.4$. Combined with the ID, it enables highly accurate reconstruction of muons, which traverse the calorimeters with minimal energy loss.

Finally, a two-level trigger system selects events. Triggers are systems or algorithms designed to rapidly assess the basic content and properties of each collision event in real time: events satisfying some predefined criteria are accepted by the trigger and recorded for subsequent analysis. Specifically, a hardware-based first-level trigger reduces the 40 MHz bunch crossing rate to below 100 kHz, after which a software-based high-level trigger further reduces the rate to approximately 1 kHz for permanent storage. The actual lepton transverse momentum criteria used in ATLAS motivates the transverse momentum requirements applied to final-state objects in the analysis (Section 4.1.1), which mimics the trigger selection, thus reducing the event rate to limit storage.

[2]The energy resolution of a calorimeter follows $\frac{\sigma(E)}{E} = \frac{a}{\sqrt{E}} \oplus \frac{b}{E} \oplus c$, where a is the sampling term, b the noise term and c the constant term accounting for local non-uniformities in the calorimeter response.

2 Quantum information in top quark physics

Quantum Information (QI) studies how information is encoded, manipulated and measured in physical systems governed by the principles of quantum mechanics [44]. The fundamental unit is the *qubit*, which is the quantum version of the classical binary *bit*. Within this framework, elementary particles can act as carriers of quantum information via their intrinsic degrees of freedom, such as spin or polarization. In this context, the spin states of $t\bar{t}$ pairs produced at colliders constitute a two-qubit system, providing a unique laboratory to investigate quantum observables in high-energy processes.

2.1 The Qubit

In classical information theory, the fundamental unit is the *bit*, which can assume one of two mutually exclusive values, 0 or 1. The quantum analogue of the classcical bit is the *quantum bit*, or *qubit*, which constitutes the basic unit of quantum information and describes the simplest non-trivial quantum system.

According to the first postulate of quantum mechanics, any isolated physical system S is associated with a complex Hilbert space $\mathcal{H}_S$ and is completely described by a state vector $|\psi_s\rangle$, represented by a unit vector in $\mathcal{H}_S$. The dimension of the Hilbert space depends on the physical system under consideration and may be either finite or infinite.

The simplest *qubit* corresponds to a two-dimensional complex Hilbert space $\mathcal{H} \cong \mathbb{C}^2$. By choosing an orthonormal basis $\{|0\rangle, |1\rangle\}$, commonly referred to as the *computational basis*, the most general state of a qubit can be expressed as a linear combination

$$|\psi\rangle = \alpha\,|0\rangle + \beta\,|1\rangle\,, \qquad \alpha, \beta \in \mathbb{C} \tag{2.1.1}$$

with $\mathcal{H} = \text{span}(|0\rangle, |1\rangle)$. The normalisation condition $\langle\psi|\psi\rangle = |\alpha|^2 + |\beta|^2 = 1$ must be satisfied. Similarly, a qu*d*it is defined as a d-level system with $\mathcal{H} = \text{span}(|0\rangle, |1\rangle, ..., |d-1\rangle)$. Unlike the classical bit, which can only take one of two values, the qubit exists in a superposition of both basis states. When a measurement is performed in the computational basis, the qubit state $|\psi\rangle$ collapses to one of the basis states $|0\rangle$ or $|1\rangle$ with probability $|\alpha|^2$ or $|\beta|^2$. After the measurement, the qubit is no longer in the initial superposition but is found in the specific state corresponding to the measurement outcome. This property is another key distinction between classical and quantum information: while reading a classical bit leaves its value unchanged, measuring a qubit collapses its wavefunction, fundamentally altering its state.

Figure 2.1.1 compares a classical bit with a qubit and introduces the Bloch sphere, an intuitive geometric representation of single-qubit states. Any qubit state can be parameterized, up to an global phase, as

$$|\psi\rangle = \cos\frac{\theta}{2}|0\rangle + e^{i\phi}\cos\frac{\theta}{2}|1\rangle \tag{2.1.2}$$

where $\theta \in [0, \pi]$ and $\phi \in [0, 2\pi)$ are spherical coordinates on the Bloch sphere. This geometric interpretation arises from the normalization condition $|\alpha|^2 + |\beta|^2 = 1$, which constrains the state vector to the surface of a unit sphere. As will be discussed in Section 2.2, pure qubit states correspond to points on the surface, while points in the interior of the sphere are mixed.

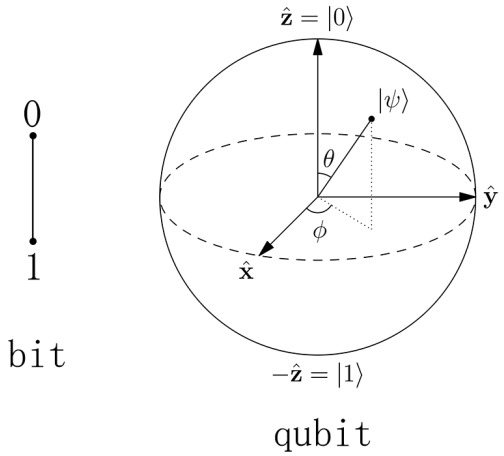

Figure 2.1.1: Geometric representation of information units. The classical bit (left) is restricted to the discrete poles of the z-axis (0 or 1). The qubit is visualized via the Bloch sphere, which considers all possible superpositions between $|0\rangle$ and $|1\rangle$ as points on the surface.

The abstract concept of the qubit admits many physical representations, allowing the same theoretical framework to be applied across different experimental systems. In particle physics, mediators and fundamental particles can be seen indeed as physical realizations of qubits, because some of their intrinsic properties naturally form two-level quantum systems. For example, photons admit two orthogonal polarization states, while spin-1/2 fermions have two possible spin projections along a given quantization axis. Instead, spin-1 bosons have three possible spin projections and can be represented as qu*tr*its, which are quantum superpositions of three orthonormal states. In this framework, the quantum information carried by the particles is encoded in their spin degrees of freedom. This motivates the study of quantum observables at colliders, where the central experimental chal-

lenge is the reconstruction of particle spin states from their decay products. In this thesis, the focus is on the top quark.

2.2 The density operator

In collider experiments, quantum systems are typically produced in statistical mixtures rather than in well-defined pure states. An example is given by top quark production at the LHC, which occurs through two indistinguishable mechanisms: gg fusion and $q\bar{q}$ annihilation (Section 1.2.2). As a consequence, the resulting quantum state must be treated as a statistical mixture, naturally described by a density operator.

Before defining this operator, it is useful to recall how expectation values of observables are computed in quantum mechanics, as well as how a state changes after a measurement. The expectation value represents the statistical average of measurement outcomes obtained from many identical preparations of the same quantum state. It therefore provides the physically accessible quantity that connects the mathematical operator formalism to experimental observations. Consider a quantum system described by a state $|\psi\rangle$ in a Hilbert space $\mathcal{H}$, which is assumed to have finite dimension d. Observables are represented by Hermitian operators $A = A^\dagger$, which admit spectral decomposition

$$A = \sum_{i=1}^{d} \lambda_i \, |e_i\rangle \, \langle e_i| \tag{2.2.1}$$

where $\{e_i\}_{i=1}^d$ is an orthogonal basis of $\mathcal{H}$ and $\lambda_i \in \mathbb{R}$ are the corresponding eigenvalues. In the presence of degeneracies, it is convenient to group eigenstates associated with the same eigenvalue. Denoting by a_j the distinct eigenvalues, the operator A can be written as

$$A = \sum_j a_j P_{a_j}, \tag{2.2.2}$$

where $P_{a_j} = \sum_{k:\, \lambda_k = a_j} |e_k\rangle \, \langle e_k|$ is the projector onto the eigenspace corresponding to a_j. The expectation value of A in the state $|\psi\rangle$ is then given by

$$\langle A \rangle \equiv \langle \psi | \, A \, | \psi \rangle = \sum_j a_j \, \langle \psi | \, P_{a_j} \, | \psi \rangle \, . \tag{2.2.3}$$

The measurement of the observable on the state $|\psi\rangle$ causes the state to collapse onto the eigenspace associated with the eigenvalue a_j (*projective* measurement),

$$|\psi\rangle \to |\psi'\rangle = \frac{P_{a_j} \, |\psi\rangle}{\sqrt{\langle \psi | \, P_{a_j} \, | \psi \rangle}} \tag{2.2.4}$$

where $\langle\psi| P_{a_j} |\psi\rangle$ is the probability associated with the outcome a_j.
Now suppose the system is prepared in a state $|\psi_i\rangle$ with probability p_i and that the procedure is repeated many times. This produces a statistical ensemble $\{p_i, |\psi_i\rangle\}$, representing the possible states of the system and their classical probabilities. The expectation value for the observable becomes

$$\langle A\rangle = \sum_i p_i \langle\psi_i| A |\psi_i\rangle := \mathrm{tr}[\rho A] \tag{2.2.5}$$

where

$$\rho := \sum_i p_i |\psi_i\rangle \langle\psi_i|, \qquad \sum_i p_i = 1, \quad p_i \geq 0. \tag{2.2.6}$$

The quantity ρ is called *density operator* and fully describes the statistical state of the system. It is a linear operator on $\mathcal{H}$ and satisfies the following properties:

$$\rho = \rho^\dagger, \qquad \mathrm{tr}[\rho] = 1, \qquad \rho \geq 0$$

where the positivity requirement means that $\langle\phi| \rho |\phi\rangle \geq 0 \ \forall |\phi\rangle \in \mathcal{H}$. In this case, the post-measurement state can be expressed as

$$\rho \to \rho' = \frac{P_{a_j} \rho P_{a_j}}{\mathrm{tr}[\rho P_{a_j}]} \tag{2.2.7}$$

where the denominator represents the probability of obtaining the measurement outcome a_j. Using the density matrix formalism, quantum states can be classified as pure or mixed:

- for a *pure state*, the density operator has the form $\rho = |\psi\rangle\langle\psi|$ for some $|\psi\rangle \in \mathcal{H}$ (e.g., $p_i = 1, p_{j\neq i} = 0$) and it satisfies $\mathrm{tr}[\rho^2] = 1$,
- for a *mixed state*, ρ is expressed as in Eq. 2.2.6, with $0 < p_i < 1$ for at least two states, and it satisfies $\mathrm{tr}[\rho^2] < 1$.

The quantity $\mathrm{tr}[\rho^2]$ indeed provides a measure of the *purity* of the state. For a Hilbert space of dimension d,

$$\frac{1}{d} \leq \mathrm{tr}[\rho^2] \leq 1 \tag{2.2.8}$$

where the lower bound corresponds to a maximally mixed state. In the case of a qubit ($d = 2$), the maximally mixed state is given by

$$\rho_{\mathrm{mix}} = \frac{1}{2}\mathbb{I}_2. \tag{2.2.9}$$

It is relevant to notice that pure states are uniquely associated to the ensemble $\{p_i, |\psi_i\rangle\}$, while mixed states can be represented with different statistical ensembles.

Any qubit can be parametrized using the Bloch-sphere representation, which was introduced for pure states in Section 2.1. In general,

$$\rho = \frac{1}{2}\left(\mathbb{I}_2 + \sum_{i=1}^{3} B_i \sigma^i\right) \tag{2.2.10}$$

where $B_i \in \mathbb{R}$ are the components of the Bloch vector $\vec{B} = k(\sin\theta\cos\phi, \sin\theta\sin\phi, \cos\theta)$, with $k \leq 1$, and σ^i are the Pauli matrices, defined as

$$\sigma^1 = \begin{pmatrix} 0 & 1 \\ 1 & 0 \end{pmatrix}, \quad \sigma^2 = \begin{pmatrix} 0 & -i \\ i & 0 \end{pmatrix}, \quad \sigma^3 = \begin{pmatrix} 1 & 0 \\ 0 & -1 \end{pmatrix}. \tag{2.2.11}$$

The set $\{\mathbb{I}_2, \sigma^x, \sigma^y, \sigma^z\}$ forms a basis of linear operators for $\mathbb{C}^2$. Pure states are characterized by $|\vec{B}| = 1$, thus corresponding to points on the surface of the sphere. Mixed states correspond to $|\vec{B}| < 1$ and live inside the sphere.

In general, a density operator acting on a d-dimensional Hilbert space is characterized by $d^2 - 1$ real parameters. Consequently, for a qubit ($d = 2$) the three coefficients B_i completely determine the quantum state of the system. For a spin-$\frac{1}{2}$ particle, such as the top quark, these coefficients represent the spin polarizations.

2.3 Two-qubit systems

Two-qubit systems play a central role in quantum information theory, as they constitute the simplest scenario in which non-classical correlations, such as quantum entanglement, can appear.

A two-qubit system is a bipartite quantum system, described by the tensor product of the Hilbert spaces of the individual qubits, $\mathcal{H} = \mathcal{H}_A \otimes \mathcal{H}_B \cong \mathbb{C}^4$. A standard basis choice for this space is the computational set $\{|00\rangle, |01\rangle, |10\rangle, |11\rangle\}$, where $|ij\rangle = |i\rangle \otimes |j\rangle$ with $i, j \in \{0, 1\}$. Consequently, any two-qubit state can be expressed as the linear combination

$$|\psi\rangle = \sum_{i,j=0}^{1} c_{ij} |ij\rangle, \qquad \sum_{i,j} |c_{ij}|^2 = 1 \tag{2.3.1}$$

where $|c_{ij}|^2$ represents the probability of observing the system in the state $|ij\rangle$ upon measurement. An important set of two-qubit states arising from particular values of the coefficients c_{ij} is given by the *Bell basis*, defined as

$$\begin{aligned} \left|\Phi^0\right\rangle &= \frac{|00\rangle + |11\rangle}{\sqrt{2}} \qquad \left|\Phi^1\right\rangle = \frac{|00\rangle - |11\rangle}{\sqrt{2}} \\ \left|\Psi^2\right\rangle &= \frac{|01\rangle + |10\rangle}{\sqrt{2}} \qquad \left|\Psi^3\right\rangle = \frac{|01\rangle - |10\rangle}{\sqrt{2}} \end{aligned} \tag{2.3.2}$$

where $|\Phi^\alpha\rangle \in \mathbb{C}^2 \otimes \mathbb{C}^2$, $|\Phi^\alpha\rangle = (\sigma^\alpha \otimes \mathbb{I}_2)\,|\Phi^0\rangle$ and $\langle\Phi^\alpha|\,\Phi^\beta\rangle = \delta_{\alpha\beta}$. As will be seen in Section 2.3.1, these states constitute an example of maximally entangled states.

Generalizing the Eq. 2.2.10 for a single qubit, the density matrix ρ of a pair of qubits A and B can be can be decomposed in the spaces of the individual qubits as

$$\rho = \frac{I_4 + \sum_i (B_i^A \sigma^i \otimes I_2 + B_i^B I_2 \otimes \sigma^i) + \sum_{i,j} C_{ij} \sigma^i \otimes \sigma^j}{4} \tag{2.3.3}$$

where $i, j = 1, 2, 3$ and σ^i are the Pauli matrices. Given that the dimension of the composite Hilbert space is four, this matrix depends on $4^2 - 1 = 15$ real independent parameters: 3 from B_i^A, 3 from B_i^B and 9 from the 3×3 correlation matrix C_{ij}, which encodes the correlations between the two qubits. This parametrization is referred to as the *Pauli* (or *Fano-Bloch*) expansion and is chosen for its transparent physical interpretation. In fact, for spin-$\frac{1}{2}$ particles, these coefficients represent their spin polarizations (B_i^A, B_i^B) and their spin correlations (C_{ij}).

This formalism can be extended to bipartite systems with arbitrary Hilbert-space dimensions [45]. It is used, for example, to study qutrit systems, such as massive bosons at colliders.

In this thesis, the focus is on $t\bar{t}$ pairs, whose spins provide an effective realization of a two-qubit system, enabling direct access to spin correlations and the study of quantum observables in high-energy processes.

2.3.1 Entanglement

Quantum entanglement is a fundamental feature of quantum mechanics in which the joint quantum state of two or more particles cannot be factorized into independent states for each particle, even when the particles are spatially separated. In an entangled system, measurements performed on one particle are correlated with measurements performed on the other in a way that cannot be explained classically.

The existence of such correlations implies a violation of the principle of *local realism*, which is based on two assumptions: locality, meaning that a measurement performed on one system cannot produce an instantaneous effect on another spatially separated system, and realism, meaning that physical properties have

definite values prior to measurement. In 1964, John Bell demonstrated that any theory based on local realism must satisfy certain mathematical constraints, known as Bell inequalities [46]. Quantum mechanics predicts scenarios in which these inequalities are violated. Such violations have been experimentally confirmed, most notably by Alain Aspect and collaborators [47], establishing entanglement as a physical phenomenon fully consistent with quantum mechanics.

The correlations observed in entangled systems can be rigorously described using the density matrix formalism. In this framework, the state of a bipartite system is represented by a density operator ρ belonging to the set of states $\mathcal{S}(\mathcal{H}_A \otimes \mathcal{H}_B) \subset \mathcal{L}(\mathcal{H}_A \otimes \mathcal{H}_B)$, where $\mathcal{L}(\mathcal{H}_\mathcal{A} \otimes \mathcal{H}_\mathcal{B})$ denotes the linear operators acting on on the composite Hilbert space of the two qubits. The reduced density operators of the subsystems A and B are obtained by taking the partial trace over the complementary subsystem,

$$\rho^A = \mathrm{tr}_B[\rho], \qquad \rho^B = \mathrm{tr}_A[\rho] \tag{2.3.4}$$

where $\rho^A \in \mathcal{S}(\mathcal{H}_A)$ and $\rho^B \in \mathcal{S}(\mathcal{H}_B)$. Within this framework, a state ρ is called *separable* if and only if it can be written as a convex sum of product states

$$\rho = \sum_n p_n \rho_n^A \otimes \rho_n^B, \qquad \sum_n p_n = 1, p_n \geq 0 \tag{2.3.5}$$

where $\rho_n^A \in \mathcal{S}(\mathcal{H}_\mathcal{A})$ and $\rho_n^B \in \mathcal{S}(\mathcal{H}_\mathcal{B})$ are density operators associated with subsystems A and B, respectively. Any state that cannot be decomposed as a classical mixture of product states is called *entangled*. In particular, a two-qubit state is maximally entangled if and only if the reduced density matrix of each subsystem is maximally mixed, which occurs as in Eq. 2.2.9 when

$$\rho^A = \rho^B = \frac{1}{2}\mathbb{I}_2 \quad \Rightarrow \quad \mathrm{tr}[{\rho^A}^2] = \mathrm{tr}[{\rho^B}^2] = \frac{1}{2}. \tag{2.3.6}$$

This means that tracing out one of the two subsystems causes the loss of information about the global state, implying that the two partial systems are correlated. An example of maximally entangled states is given by the Bell basis of Eq. 2.3.2, since for any state $|\Phi\rangle$ of the set

$$\rho^A = \mathrm{tr}_B[|\Phi\rangle\langle\Phi|] = \frac{1}{2}\mathbb{I}_2, \quad \rho^B = \mathrm{tr}_A[|\Phi\rangle\langle\Phi|] = \frac{1}{2}\mathbb{I}_2. \tag{2.3.7}$$

It is relevant to note that the Bell states are globally pure, $\mathrm{tr}[|\Phi\rangle\langle\Phi|] = 1$, which means that the total state is completely known. Nevertheless, due to entanglement, information about the subsystems is encoded in the correlations between them, so each subsystem is in a mixed state and cannot be fully described on its own. In general, a state can be pure while its parts appear mixed.

There are several theoretical criteria that can be used to detect entanglement in two-qubit states. The most widely used is the *Peres-Horodecki* criterion [48–50], which provides a necessary condition for a given quantum system to be separable. It states that, if a state ρ is separable, then its partial transpose with respect to the second subsystem, defined as

$$\rho^{\mathrm{T}_B} = \sum_n p_n \rho_n^A \otimes (\rho_n^B)^{\mathrm{T}} \tag{2.3.8}$$

must remain a positive semi-definite operator, namely $\rho^{\mathrm{T}_B} \geq 0$. Conversely, if ρ^{T_B} has at least one negative eigenvalue the state is entangled. The statement equivalently holds for the partial transpose of the first subsystem. For two-qubit (2×2) and qubit-qutrit (2×3) systems, the Peres-Horodecki criterion is both a necessary and sufficient condition for separability and it's possible to completely characterize entanglement.

Another sufficient condition for entanglement [51] can be derived by expanding Eq. 2.3.3 and applying the Peres–Horodecki criterion. It is given in terms of the elements of the correlation matrix C, specifically

$$\Delta \equiv -C_{33} + |C_{11} + C_{22}| - 1 > 0. \tag{2.3.9}$$

As a consequence, also $-\mathrm{tr}[C] > 1$ provides a sufficient condition for entanglement. While the previous criteria provide tests to determine whether a state is entangled, they do not quantify the amount of entanglement present. A quantitative measure of entanglement is given by the *concurrence*, defined as

$$\mathcal{C}[\rho] = \max(0, \lambda_1 - \lambda_2 - \lambda_3 - \lambda_4) \tag{2.3.10}$$

where λ_i are the eigenvalues, from the biggest to the smallest, of the matrix

$$\sqrt{\sqrt{\rho}(\sigma^2 \otimes \sigma^2)\rho^*(\sigma^2 \otimes \sigma^2)\sqrt{\rho}} \tag{2.3.11}$$

where ρ^* is the complex-conjugate of the density matrix ρ. For a pair of qubits, $0 \leq \mathcal{C}[\rho] \leq 1$ and the necessary and sufficient condition for entanglement is given by $\mathcal{C}[\rho] > 0$. This implies that ρ is maximally entangled if $\mathcal{C}[\rho] = 1$.

2.3.2 Magic

Quantum magic is a quantity that is introduced in the context of quantum computation. In this field, fundamental processing units are *quantum circuits*, which are structured as sequences of unitary operations $\mathcal{U}$, acting on an initial state $|\psi_{in}\rangle$ of

n input qubits as $\mathcal{U}|\psi_{in}\rangle = |\psi_{in}\rangle$. This multi-qubit state $|\psi_{in}\rangle$ is defined in a 2^n-dimensional Hilbert space and built from the tensor product of individual qubits $|\psi_i\rangle$ as

$$|\Psi_{in}\rangle = |\psi_1\rangle \otimes |\psi_2\rangle \otimes \cdots \otimes |\psi_n\rangle. \tag{2.3.12}$$

The unitaries $\mathcal{U}$, commonly referred to as *quantum gates*, are the building blocks of any *quantum algorithm*, which is a sequence of operations designed to solve computational problems encoded within the input qubits. The key feature of such an algorithm is to exploit quantum superposition and entanglement, which are manipulated to generate correlations that cannot be reproduced classically and may lead to a computational advantage. An example is the *Shor's algorithm* [52], which provides an exponential speedup for integer factorization compared to classical supercomputers.

However, it has been observed that entanglement alone is not sufficient to guarantee a computational advantage. In fact, according to the *Gottesman-Knill theorem* [53], certain maximally entangled states, known as *stabiliser* states, can be efficiently simulated classically and therefore do not provide any improvement in computational efficiency. Stabiliser states are multi-qubit states $|\psi\rangle$ that give a simple spectrum for a restricted set of operators, known as *Pauli strings*[3] and defined as

$$\mathcal{P}_n = P_1 \otimes P_2 \otimes \cdots \otimes P_n, \qquad P_i \in \{\mathbb{I}_2, \sigma^1, \sigma^2, \sigma^3\} \tag{2.3.13}$$

where each P_i acts on a qubit. For a n-qubit state, the number of Pauli strings is 4^n. The *Pauli spectrum* for a generic multi-qubit state $|\phi\rangle$ is given by

$$\text{spec}(|\phi\rangle) \equiv \{\langle\phi| P |\phi\rangle, P \in \mathcal{P}_n\} \tag{2.3.14}$$

with 4^n total elements. For a stabiliser state $|\psi\rangle$, the expectation values $\langle\psi| P |\psi\rangle$ are restricted to the discrete set $\{0, \pm 1\}$, with 2^n non-zero values.

The "extra" ingredient needed for efficient quantum computing has been referred to as *magic* and quantifies the *non-stabiliserness* of a quantum state, thereby quantifying the potential computational advantage over classical states. One widely used definition is given by the *Stabiliser Rényi Entropies (SREs)* [54], defined as

$$M_q \equiv \frac{1}{1-q} \log_2(\zeta_q), \qquad \zeta_q \equiv \sum_{P \in \mathcal{P}_n} \frac{\langle\psi| P |\psi\rangle^{2q}}{2^n} \tag{2.3.15}$$

where $q \geq 2$ is an integer that indicates the specific Rényi entropy of the set. For a stabiliser state, $\zeta_q = 1$, which implies $M_q = 0$. In Section 2.5.6, the focus will be on the *Second Stabiliser Rényi Entropiy* M_2, which is sufficient to quantify non-zero

[3]Formally, a Pauli string is an element of the *Pauli group*, which includes the phase factors $\{\pm 1, \pm i\}$.

magic. Given that $\langle\psi|\, P\, |\psi\rangle = \mathrm{tr}[P\rho]$, it can be expressed for a mixed two-qubit state ($n = 2$) as

$$M_2(\rho) = -\log_2\left(\frac{\sum_{P\in\mathcal{P}_2}\mathrm{tr}^4[P\rho]}{\sum_{P\in\mathcal{P}_2}\mathrm{tr}^2[P\rho]}\right), \tag{2.3.16}$$

where the set of Pauli strings $\mathcal{P}_2$ contains $4^2 = 16$ elements and is defined as

$$\mathcal{P}_2 = \{\mathbb{I}_2\otimes\mathbb{I}_2, \mathbb{I}_2\otimes\sigma^i, \sigma^j\otimes\mathbb{I}_2, \sigma^i\otimes\sigma^j \mid i,j = 1,2,3\}. \tag{2.3.17}$$

The quantity M_2 is bounded by $0 \leq M_2(\rho) \leq \log_2(2^n+1)|_{n=2} = 1.32$ [55], where $M_2 = 0$ if ρ is a stabiliser state.

2.4 Quantum state tomography

The evaluation of expectation values of arbitrary quantum observables generally requires complete knowledge of the quantum state.

In classical information, the output of a measurement corresponds to a definite value and the information is stored in bits, which represent well-defined states. In contrast, quantum information is encoded in the coefficients of the linear superposition appearing in Eq. 2.1.1. Given that the act of measurement causes the state to collapse to one of the basis states, as discussed in Section 2.2, the output is obtained only probabilistically. As a consequence, the coefficients of the superposition, which fully characterize the state, cannot be assessed in a single measurement, but must be inferred from repeated measurement on an ensemble of identically prepared states.

This reconstruction procedure is known as *quantum state tomography* and relies on a carefully chosen set of observables, whose measurement statistics provide sufficient information to determine all the independent parameters of the density matrix. The concept is first introduced here through a general formalism for a single qubit, followed by the two-qubit case using the specific parametrization of the Fano-Bloch expansion.

For a single qubit, Eq. 2.2.10 can be rewritten as

$$\rho = \sum_{\alpha=0}^{3} c_\alpha\sigma^\alpha \tag{2.4.1}$$

where the set $\{\sigma^\alpha\}_{\alpha=0}^3$, with $\sigma^0 = \mathbb{I}_2$, forms a complete basis of operators for $\mathbb{C}^2$. The Pauli matrices satisfy the orthogonality relation $\mathrm{tr}[\sigma^\alpha\sigma^\beta] = \delta_{\alpha\beta}$, which allows the coefficients c_α to be expressed in terms of the expectation value $\langle\sigma^\alpha\rangle$ of the basis operators, which from Eq. 2.2.5 is given by $\mathrm{tr}[\rho\sigma^\alpha]$. Indeed

$$\mathrm{tr}[\rho\sigma^\alpha] = \mathrm{tr}\left[\sum_{\beta=0}^{3} c_\beta\sigma^\beta\sigma^\alpha\right] = 2c_\alpha \qquad \Rightarrow \qquad c_\alpha = \frac{\mathrm{tr}[\rho\sigma^\alpha]}{2}. \tag{2.4.2}$$

In practice, the expectation values $\langle\sigma^\alpha\rangle$ can be estimated as statistical averages of the measurements outcomes of the observables σ^α, where the measurements are performed on an ensemble of identically prepared copies of the state ρ. In this way, the coefficients c_α can be determined, allowing for the complete reconstruction of the density matrix ρ. In particular, the Bloch vector components in Eq. 2.2.10 are given by $B_i = \langle\sigma^i\rangle = \mathrm{tr}[\rho\sigma^i]$ and, for a spin-$\frac{1}{2}$ particle, represent the spin polarizations and completely define the quantum state.

This idea can be easily generalized for the case of two qubits. Starting from Eq. 2.3.3, the coefficients B_i^A, B_i^B and C_{ij} are directly measured as expectation values of local and bilocal Pauli operators. The corresponding expressions are given by

$$\begin{aligned} B_i^A &= \langle\sigma^i \otimes \mathbb{I}_2\rangle = \mathrm{tr}[(\sigma^i \otimes \mathbb{I}_2)\rho] \\ B_i^B &= \langle\mathbb{I}_2 \otimes \sigma^i\rangle = \mathrm{tr}[(\mathbb{I}_2 \otimes \sigma^i)\rho] \\ C_{ij} &= \langle\sigma^i \otimes \sigma^j\rangle = \mathrm{tr}[(\sigma^i \otimes \sigma^j)\rho] \end{aligned} \tag{2.4.3}$$

where the set of observables of interest is $\{\sigma^i \otimes \mathbb{I}_2, \mathbb{I}_2 \otimes \sigma^i, \sigma^i \otimes \sigma^j\}$. Measuring these observables on identically prepared two-qubit states, and averaging over the outcomes, enables the reconstruction of the density matrix ρ. In the context of the $t\bar{t}$ system, as discussed in Section 2.3, the B_i terms represent the individual spin polarizations of top and antitop quarks, while the C_{ij} are the spin correlation coefficients. Specifically, the spin operators for qubit states are defined as

$$S_1 = \frac{1}{2}\sigma_1, \qquad S_2 = \frac{1}{2}\sigma_2, \qquad S_3 = \frac{1}{2}\sigma_3, \tag{2.4.4}$$

which means that

$$\langle S_A\rangle = \frac{1}{2}B^A, \qquad \langle S_B\rangle = \frac{1}{2}B^B, \qquad \langle S_A S_B\rangle = \frac{1}{4}C, \tag{2.4.5}$$

where $\langle S\rangle \equiv \langle S \otimes \mathbb{I}_2\rangle$ and S_A, S_B are the spin operators of the qubits A,B respectively.

2.5 Quantum tomography applied to the $t\bar{t}$ system

The top quark, being a spin-1/2 particle, can be described as a qubit (Section 2.1). Its unique properties, presented in Section 1.2, allow direct experimental access to its spin information, making the $t\bar{t}$ system an ideal two-qubit system to study at the TeV scale. This section presents the theoretical framework of the $t\bar{t}$ spin density matrix and its reconstruction from the angular distributions of the decay products using the quantum tomography technique discussed in Section 2.4. Spin correlation coefficients are then used to construct entanglement measures for the $t\bar{t}$ system and related quantum observables.

2.5.1 Top quark polarization and $t\bar{t}$ spin correlations

One of the unique features of the top quark is that it decays before its spin properties can be altered by QCD interactions, so that spin information is preserved and encoded in the angular distributions of its decay products. In this section, the spin polarization and spin correlations quantities are introduced, as these concepts will be used throughout the following parts.

The polarization of the top quark describes the average orientation of its spin along a chosen quantization axis and is defined as

$$P = \frac{N_\uparrow - N_\downarrow}{N_\uparrow + N_\downarrow} \tag{2.5.1}$$

where $N_{\uparrow,\downarrow}$ denotes the number of events with spin aligned and anti-aligned with the reference axis, respectively. At the LHC, top quarks produced via QCD interactions are essentially unpolarized at leading order in the Standard Model, although polarization can arise in some new physics scenarios.

Any observable sensitive to the top quark polarization is referred to as a *polarimeter*. Experimentally, the polarization of the top quark is accessed through the angular distribution its daughter particles, as will be explained more deeply in Section 2.5.3. In this context, the decay products of the top quark serve as natural polarimeters, as their emission directions are correlated with the spin of the parent quark. The strength of this correlation is quantified by a parameter known as *spin analyzing power* α, which ranges from -1 to $+1$, corresponding to maximal anti-alignment and maximal alignment with the spin direction, respectively. Charged leptons arising from $t \to Wb \to \ell\nu b$ are perfect polarimeters, as their spin analyzing power is given by ($\alpha_{\ell^\pm} \approx \pm 1$). The same holds for the d, s quarks from hadronic W decay. The spin analyzing power for different decay products of the top quark are summarized in Table 4.

Particle	α
b	-0.3925
W^+	0.3925
ℓ^+	0.999
$\bar{d}, \bar{s}$	0.9664
u, c	-0.3167

Table 4: Spin analyzing power α for different decay products of the top quark. The sign of α flips for the respective antiparticles.

Although $t\bar{t}$ pairs produced in hadron collisions at the LHC are unpolarized, the spins of the top and antitop are correlated. Near production threshold, QCD

predicts that $q\bar{q}$ annihilation produces a spin-triplet ${}^3S_1$ state with aligned spins, while gg fusion yields a spin-singlet ${}^1S_0$ state with opposite spin alignment. At the LHC, where gg fusion is the dominant production mechanism, antiparallel configurations prevail near threshold. These spin correlations are also relevant in the context of toponium for which, as discussed in Section 1.2.4, the spin-singlet η_t is expected to be the dominant $t\bar{t}$ bound state in this region. At large $t\bar{t}$ invariant masses at the LHC, however, production is mainly driven by gluons with opposite helicities, giving rise to spin-aligned top pairs analogous to those from $q\bar{q}$ annihilation [56].

The spins of the top and antitop quarks are correlated with a strength depending on the spin quantisation axis. The spin correlation coefficients C_{ij} are defined as

$$C_{ij} = \frac{N_{\uparrow\uparrow} + N_{\downarrow\downarrow} - N_{\uparrow\downarrow} - N_{\downarrow\uparrow}}{N_{\uparrow\uparrow} + N_{\downarrow\downarrow} + N_{\uparrow\downarrow} + N_{\downarrow\uparrow}} \tag{2.5.2}$$

where the first arrow represents the alignment ($\uparrow$) or disalignment ($\downarrow$) of the top quark spin along a chosen quantization axis (such as i), and the second arrow represents the same for the antitop quark. Therefore, they quantify the correlation between the i-th component of the top spin and the j-th component of the antitop spin and are bounded by $-1 \leq C_{ij} \leq 1$. They are fully encoded in a 3×3 matrix C, which depends on the $t\bar{t}$ production mechanism, on $m_{t\bar{t}}$ and on the top quark scattering angle, as will be seen in Section 2.5.2.

2.5.2 Spin density matrix

The quantum state of the $t\bar{t}$ pair produced at hadron colliders depends on the kinematics of the system. The production is fully characterized by the invariant mass $m_{t\bar{t}}$ and the direction $\hat{k}$ of the top quark in the $t\bar{t}$ rest frame. Momentum conservation implies that the top and antitop four-momenta can be written as

$$k_t^\mu = (E_t, \vec{k}), \qquad k_{\bar{t}}^\mu = (E_t, -\vec{k}). \tag{2.5.3}$$

Both particles satisfy the on-shell condition $k_t^2 = k_{\bar{t}}^2 = m_t^2$, where $k^2 \equiv k^\mu k_\mu$. The invariant mass of the pair in the $t\bar{t}$ rest frame is given by

$$m_{t\bar{t}}^2 = (k_t^\mu + k_{\bar{t}}^\mu)^2 = 4E_t^2 = 4(m_t^2 + \vec{k}^2)\,. \tag{2.5.4}$$

By relating the top quark momentum to its velocity β through

$$|\vec{k}| = \frac{m_t \beta}{\sqrt{1-\beta^2}}\,, \tag{2.5.5}$$

it is possible to obtain

$$\beta = \sqrt{1 - \frac{4m_t^2}{m_{t\bar{t}}^2}}\,, \tag{2.5.6}$$

where $\beta = 0$ ($m_{t\bar{t}} = 2m_t$) corresponds to the production at threshold.

For fixed $(m_{t\bar{t}}, \hat{k})$ kinematics, the spin density matrix of $t\bar{t}$ production can be decomposed into the corresponding top and antitop subspaces as

$$R(m_{t\bar{t}}, \hat{k}) = \tilde{A}\,\mathbb{I}_4 + \sum_i \left(\tilde{B}_i^+\,\sigma^i \otimes \mathbb{I}_2 \;+\; \tilde{B}_i^-\,\mathbb{I}_2 \otimes \sigma^i \right) \;+\; \sum_{i,j} \tilde{C}_{ij}\,\sigma^i \otimes \sigma^j \qquad (2.5.7)$$

where the i, j indices represent the axes with respect to the projection of the spin is evaluated and $\{\tilde{A}, \tilde{B}_i^{\pm}, \tilde{C}_{ij}\}$ are called *Fano* coefficients, which depend on the kinematics of the process and on the choice of the spin quantization basis. This form is clearly similar to the two-qubit state ρ in Eq. 2.3.3. However, while ρ depends on 15 independent parameters, the production matrix R is characterized by 16 parameters since the normalization condition is not satisfied. Indeed, $\mathrm{tr}[R] = 4\tilde{A}$, where $\tilde{A}$ is the additional coefficient. Specifically, it determines the differential cross section for a given energy and top quark direction,

$$\frac{d\sigma}{d\Omega_{\hat{k}} dm_{t\bar{t}}} = \frac{\alpha_s^2 \beta}{m_{t\bar{t}}^2} \tilde{A}(m_{t\bar{t}}, \hat{k}) \qquad (2.5.8)$$

where $\Omega_{\hat{k}}$ is the solid angle associated to $\hat{k}$ direction and α_S the strong coupling constant. Upon normalization, the properly defined density matrix $\rho(m_{t\bar{t}}, \hat{k})$ is recovered, together with the correct spin polarization and correlation coefficients:

$$\rho(m_{t\bar{t}}, \hat{k}) = \frac{R}{\mathrm{tr}(R)} = \frac{R}{4\tilde{A}}\,, \qquad B_i^{\pm} = \frac{\tilde{B}_i^{\pm}}{\tilde{A}}, \qquad C_{ij} = \frac{\tilde{C}_{ij}}{\tilde{A}}. \qquad (2.5.9)$$

In this form, the density matrix is directly related to measurable quantities: $B_i^{\pm}, C_{ij}$. Here, $B_i^{\pm}$ represents the spin polarization along the axis i, while the ij-entry of the matrix C represents the spin correlation between the i-th component of the top quark spin and the j-th component of the antitop quark spin.

At hadron colliders, $t\bar{t}$ production proceeds through different initial partonic channels. Consequently, even for fixed kinematics $(m_{t\bar{t}}, \hat{k})$, the spin state of the $t\bar{t}$ system is a statistical mixture of the contributions from these channels,

$$\rho(m_{t\bar{t}}, \hat{k}) = \sum_{I=q\bar{q},gg} w_I(m_{t\bar{t}}, \hat{k})\,\rho^I(m_{t\bar{t}}, \hat{k}) \qquad (2.5.10)$$

where the weights w_I encode the information on the parton distribution functions and are determined by the corresponding partonic luminosities [51]. The total quantum state in a finite region Π of phase-space can be reconstructed as

$$\rho = \int_{\Pi} dm_{t\bar{t}}\, d\Omega\, p(m_{t\bar{t}}, \hat{k})\,\rho(m_{t\bar{t}}, \hat{k}) \qquad (2.5.11)$$

where $p(m_{t\bar{t}}, \hat{k})$ is the is normalized differential production cross section, defined as

$$p(m_{t\bar{t}}, \hat{k}) = \frac{1}{\sigma_\Pi} \frac{d\sigma}{d\Omega dm_{t\bar{t}}}, \qquad \sigma_\Pi \equiv \int d\Omega dm_{t\bar{t}} \frac{d\sigma}{d\Omega dm_{t\bar{t}}}. \tag{2.5.12}$$

2.5.3 Reconstruction of the spin density matrix from decay products

This section establishes the connection between the spin quantum state of the $t\bar{t}$ system and measurable kinematic distributions, together with the extraction of the spin correlation coefficients. Experimentally, although the spin of the top quark cannot be directly measured, its extremely short lifetime ensures that it decays before hadronizing and well before QCD effects can alter its spin state (Section 1.2). Consequently, its spin information is immediately transferred to the decay products and can be inferred from their angular distributions, in which it is encoded.

As discussed in the previous sections, a quantum measurement of a single event does not provide sufficient information to determine the underlying spin state. Therefore, to fully reconstruct the two-qubit spin density matrix of the $t\bar{t}$ system, a statistical analysis over many pp collision events is required. This reconstruction is performed using quantum tomography (Section 2.4), which allows the matrix elements to be extracted as expectation values of angular observables defined in the top quark rest frame.

To relate the production spin density matrix to measurable quantities, it must be combined with the decay spin density matrices of the top and antitop quarks. In the narrow-width approximation ($\Gamma_t \sim 1\,\text{GeV} \ll m_t$) and at a fixed center-of-mass energy $\sqrt{s}$, the differential cross section for the full process

$$pp \to t\bar{t} \to F\bar{F}$$

can be factorized into production and decay contributions as [57, 58]

$$d\sigma_{F\bar{F}} \sim \sum_{\alpha\alpha',\beta\beta'} R_{\alpha\beta,\alpha'\beta'}(m_{t\bar{t}}, \hat{k}) \Gamma^F_{\alpha'\alpha} \bar{\Gamma}^{\bar{F}}_{\beta'\beta} = \text{tr}\left[\left(\Gamma^F \otimes \bar{\Gamma}^{\bar{F}}\right) R(m_{t\bar{t}}, \hat{k})\right]. \tag{2.5.13}$$

Here, $\Gamma^F_{\alpha'\alpha}$ and $\bar{\Gamma}^{\bar{F}}_{\beta'\beta}$ denote the decay spin density matrices of the top and antitop quarks, evaluated in the respective rest frames. The indices $\alpha(\alpha')$ and $\beta(\beta')$ label the respective spin in the production (decay) state, while $F(\bar{F})$ represents the specific final state of the top (antitop) decay. The information contained in $R(m_{t\bar{t}}, \hat{k})$ (Eq. 2.5.7) is therefore encoded in the joint angular distributions of the decay products. If all final-state degrees of freedom are integrated out except for the direction of a selected daughter particle, denoted with a for the top and with

b for the antitop, the decay density matrices can be expressed as [56]

$$\begin{aligned}\Gamma^F \to \Gamma^a &= \frac{1}{2}\left(\mathbb{I}_2 + \alpha_a \sum_i \hat{q}_a^i \sigma^i\right) \\ \bar{\Gamma}^{\bar{F}} \to \bar{\Gamma}^b &= \frac{1}{2}\left(\mathbb{I}_2 + \alpha_b \sum_i \hat{q}_b^i \sigma^i\right)\end{aligned} \tag{2.5.14}$$

where σ^i are the Pauli matrices, $\hat{q}_{a,b}$ are the unit vectors specifying the directions of the decay products in the respective parent rest frames and $\alpha_{a,b}$ are the corresponding spin analyzing powers defined in Section 2.5.1. In this form, once inserted into the full factorized cross section, the decay matrices project the top and antitop spin states onto the directions $\hat{q_a}$ and $\hat{q}_b$, thereby translating the spin information into measurable angular observables. For fixed kinematics $(dm_{t\bar{t}}, d\Omega_{\hat{k}})$, the differential cross section describing the joint angular distribution of a and b can indeed be written as

$$\begin{aligned}\frac{d\sigma}{d\Omega_a d\Omega_b dm_{t\bar{t}} d\Omega_{\hat{k}}} &\sim \frac{\alpha_S^2 \beta}{m_{t\bar{t}}^2} \mathrm{tr}\left[\left(\Gamma^a \otimes \bar{\Gamma}^b\right) R(m_{t\bar{t}}, \hat{k})\right] \\ &\sim \frac{\alpha_S^2 \beta}{m_{t\bar{t}}^2} [\tilde{A} + \alpha_a \tilde{B}^+ \cdot \hat{q}_a + \alpha_b \tilde{B}^- \cdot \hat{q}_b + \alpha_a \alpha_b \hat{q_a} \cdot \tilde{C} \cdot \hat{q}_b]\end{aligned} \tag{2.5.15}$$

where $\Omega_{a,b}, \Omega_{\hat{k}}$ denote the solid angles associated with the directions $\hat{q}_{a,b}, \hat{k}$, respectively. Finally, integrating over all possible top directions and center-of-mass energies yields the normalized total differential cross section

$$\frac{1}{\sigma}\frac{d\sigma}{d\Omega_a d\Omega_b} = \frac{1 + \alpha_a B^+ \cdot \hat{q}_a + \alpha_b B^- \cdot \hat{q}_b + \alpha_a \alpha_b \hat{q_a} \cdot C \cdot \hat{q}_b}{(4\pi)^2} \tag{2.5.16}$$

which describes the angular distribution of the $t\bar{t}$ decay products. The vectors $B^\pm$ and the matrix C represent the kinematically averaged counterparts of the quantities $\tilde{B}^\pm$ and $\tilde{C}$ introduced at fixed $(m_{t\bar{t}}, \hat{k})$ and correspond to the physically observable polarization vectors and spin correlations matrix of the top and antitop quarks. This expression makes explicit how these coefficients can be extracted from measured angular distributions, thereby enabling the reconstruction of the $t\bar{t}$ spin density matrix from experimental data.

The solid angle element $d\Omega_{a,b}$ is defined as $d\Omega_x = d\cos\theta_x \, d\phi_x$ (with $x = a, b$), where θ_x is the polar angle of the decay product x in the parent rest frame, defined with respect to a certain direction $\hat{i}$ through

$$\cos\theta_x^i \equiv \hat{q}_x \cdot \hat{i} \tag{2.5.17}$$

while $d\phi_x$ is the corresponding azimuthal angle. By integrating over the azimuthal angle, one obtains the relation

$$\frac{1}{\sigma}\frac{d^2\sigma}{d(\cos\theta_a^i)d(\cos\theta_b^j)} = \frac{1}{4}(1+\alpha_a B_i^+\cos\theta_a^i + \alpha_b B_j^-\cos\theta_b^j + \alpha_a\alpha_b C_{ij}\cos\theta_a^i\cos\theta_b^j). \tag{2.5.18}$$

Further integration over one of the angles yields the single-differential cross sections with respect to $\cos\theta_a^i$, $\cos\theta_b^i$ and the product $\cos\theta_a^i\cos\theta_b^j$:

$$\begin{aligned}
\frac{1}{\sigma}\frac{d\sigma}{d(\cos\theta_a^i)} &= \frac{1}{2}(1+\alpha_a B_i^+\cos\theta_a^i) \\
\frac{1}{\sigma}\frac{d\sigma}{d(\cos\theta_b^i)} &= \frac{1}{2}(1+\alpha_b B_i^+\cos\theta_b^i) \\
\frac{1}{\sigma}\frac{d\sigma}{d(\cos\theta_a^i\cos\theta_b^j)} &= -\frac{1}{2}(1+\alpha_a\alpha_b C_{ij}\cos\theta_a^i\cos\theta_b^j)\log|\cos\theta_a^i\cos\theta_b^j|.
\end{aligned} \tag{2.5.19}$$

Finally, the coefficients $B_i^\pm, C_{ij}$ can be extracted from the angular distributions of Eq. 2.5.19 through suitable expectation values. Defining the expectation value of a variable x as

$$\langle x\rangle = \int_{-1}^{1} dx \frac{1}{\sigma}\frac{d\sigma}{dx}x \tag{2.5.20}$$

the polarization coefficients for the top and antitop quarks are obtained as

$$B_i^+ = \frac{3}{\alpha_a}\langle\cos\theta_a^i\rangle, \qquad B_i^- = \frac{3}{\alpha_b}\langle\cos\theta_b^i\rangle, \tag{2.5.21}$$

where $-1 \leq B_i^\pm \leq 1$. Similarly, the spin correlation coefficients for the $t\bar{t}$ pair are given by

$$C_{ij} = \frac{9}{\alpha_a\alpha_b}\langle\cos\theta_a^i\cos\theta_b^j\rangle \tag{2.5.22}$$

where $-1 \leq C_{ij} \leq 1$. Therefore, through the kinematic reconstruction of the $t\bar{t}$ system, the angular observables $\cos\theta_x^i$ can be measured, allowing the extraction of the coefficients $B_i^\pm, C_{ij}$ and thus the determination of the spin properties of the $t\bar{t}$ system. The use of this technique is well-established and has been employed by the ATLAS, CMS and previous collaborations to perform the measurement of the coefficients, as shown in Section 2.5.1.

2.5.4 The helicity basis

In 2.5.7 the indices i, j label the spatial directions along which the spin projections are defined. The explicit determination of the spin polarization and correlation coefficients, $B_i^\pm$ and C_{ij}, requires the choice of a specific spin quantization basis.

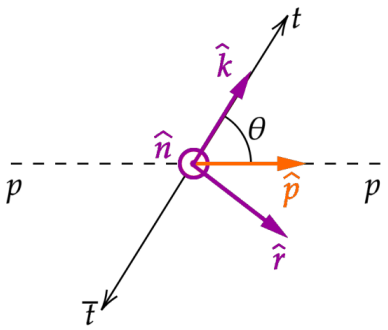

Figure 2.5.1: Geometry of $t\bar{t}$ production in the pair's rest frame. The helicity basis is shown: $\hat{k}$ lies along the top quark momentum, $\hat{n}$ is normal to the production plane $(\hat{k}, \hat{p})$ and $\hat{r}$ is orthogonal to $\hat{k}$ within the $(\hat{k}, \hat{p})$ plane. The angle θ denotes the scattering angle relative to the beam axis $\hat{p}$.

A natural and convenient choice is the orthonormal *helicity basis*, defined in the $t\bar{t}$ rest frame co-moving with the top quark. It is a right-handed coordinate system given by the set of unit vectors $\{\hat{k}, \hat{r}, \hat{n}\}$, defined as

$$\begin{cases} \hat{k} = \text{direction of the top quark in the } t\bar{t} \text{ rest frame} \\ \hat{r} = \dfrac{1}{r}(\hat{p} - y\,\hat{k}) \\ \hat{n} = \hat{k} \times \hat{r} \end{cases} \tag{2.5.23}$$

where $\hat{p}$ is the direction of one of the proton beams, $r = \text{sgn}(y)\sqrt{1-y^2}$ and $y = \hat{k} \cdot \hat{p} = \cos\theta$ gives the top scattering angle with respect to the beam. A schematic representation of this basis is provided in Figure 2.5.1. This choice simplifies the spin density matrix $R(m_{t\bar{t}}, \hat{k})$, whose dependence is reduced to θ and β only, where the latter is the velocity of the top quark in the $t\bar{t}$ rest frame.

The advantage of the helicity basis lies in its invariance under boosts along the particle momentum directions. Although top and antitop spins are strictly defined in their rest frames, they can be related to those in the $t\bar{t}$ center-of-mass frame via a Lorentz boost along the top momentum direction $\hat{k}$, which preserves the orientation of the helicity axis. This is very useful when computing the angular observables of Eq. 2.5.17, defined in the top rest frame. For this reason, it is adopted in this thesis, as discussed in Section 3.2.3.

2.5.5 Entanglement in $t\bar{t}$ production

In pair production, top and antitop quarks exhibit spin correlation patterns. Although correlations can in principle be explained by classical physics, certain

stronger forms of correlations, specifically entanglement, cannot. These quantum correlations can be investigated through the spin density matrix defined in Eq. 2.5.9 and they are entirely encoded in the matrix C, which is used to compute the quantum observables of interest. It is relevant to note that, according to the separability condition in Eq. 2.3.5, if all substates $\rho(m_{t\bar{t}}, \hat{k})$ are separable, then the total quantum state defined in Eq. 2.5.11 is also separable.

The spin density matrix can be simplified at LO as already discussed in Section 2.5.1. First, the top and antitop quarks at LO are produced unpolarized, namely $B_i^{\pm} = 0$, reducing the structure to

$$\rho = \frac{1}{4}\left(I_4 + \sum_{i,j=1}^{3} C_{ij}\,\sigma^i \otimes \sigma^j\right). \tag{2.5.24}$$

Then, C is symmetric at LO, namely $C_{ij} = C_{ji}$. Hence by means of local rotations in spin space, it can be diagonalized without affecting entanglement properties. Under these assumptions, the number of independent parameters is reduced from 15 to 6. Furthermore, at the LHC, it is a good approximation to consider only the diagonal elements and one off-diagonal ($C_{12} = C_{21}$, even though of $\sim \mathcal{O}(10)$ smaller) as non-zero, which reduces the number of relevant parameters even further to 4 [59]. The diagonal elements of the spin correlation matrix, evaluated in the helicity basis, are illustrated in the $(m_{t\bar{t}}, \cos\theta)$ plane in Figure 2.5.2. As evident, spin correlations are stronger in two regions: at threshold and at very high invariant masses for $|\cos\theta| \lesssim 0.4$.

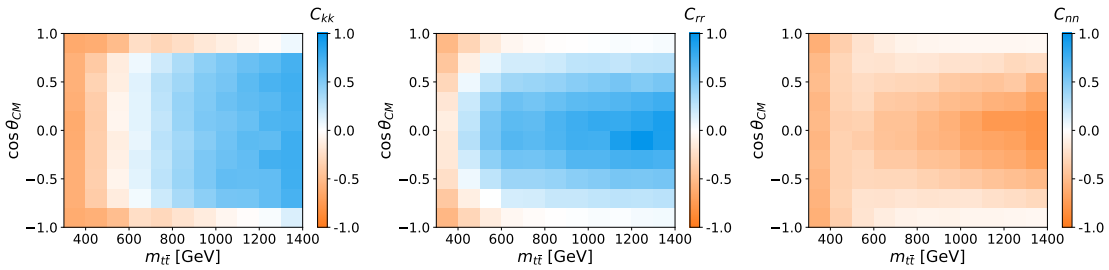

Figure 2.5.2: Parton-level distributions of the spin correlation coefficients C_{kk} (left), C_{rr} (center) and C_{nn} (right) in the helicity frame as functions of $(m_{t\bar{t}}, \cos\theta_{\mathrm{CM}} \equiv \cos\theta)$ [60].

With the simplified structure of the $t\bar{t}$ spin density matrix, Eq.2.3.9 becomes a sufficient and necessary criterion for entanglement. In the helicity basis it is expressed as

$$\Delta \equiv -C_{nn} + |C_{kk} + C_{rr}| - 1 > 0 \tag{2.5.25}$$

with the concurrence (2.3.10) simply given by

$$\mathcal{C}[\rho] = \frac{\max(\Delta, 0)}{2}. \tag{2.5.26}$$

Two quantities similar to Eq. 2.5.25 can be derived for the initial partonic substates $\rho^I(m_{t\bar{t}}, \hat{k})$. For gg fusion [51],

$$\Delta^{gg} = \begin{cases} \dfrac{2 - 4\beta^2(1+\sin^2\theta) + 2\beta^4(1+\sin^4\theta)}{1 + 2\beta^2\sin^2\theta - \beta^4(1+\sin^4\theta)}, & \text{if } \beta^2(1+\sin^2\theta) < 1 \\ \dfrac{2\beta^4(1+\sin^4\theta) - 2}{1 + 2\beta^2\sin^2\theta - \beta^4(1+\sin^4\theta)}, & \text{if } \beta^2(1+\sin^2\theta) \geq 1 \end{cases} \tag{2.5.27}$$

This condition defines two boundaries in phase space that separate the regions of separability and entanglement. As a result, $\rho^{gg}(m_{t\bar{t}}, \hat{k})$ is separable in a finite region of phase space, while entanglement is present at $t\bar{t}$ production threshold and at very high energies, as shown in the first plot (a) in Figure 2.5.3. The origin

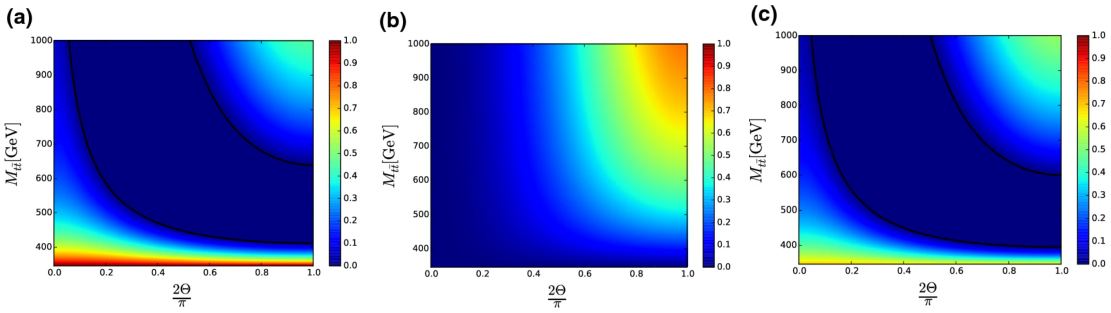

Figure 2.5.3: Entanglement as a function of $m_{t\bar{t}}$ and the production angle θ in the $t\bar{t}$ rest frame, quantified by the concurrence (Eq. (2.5.26)) of the spin density matrix $\rho^I(m_{t\bar{t}}, \hat{k})$ for a) gg fusion and b) $q\bar{q}$ annihilation. Concurrence of the spin density matrix $\rho(m_{t\bar{t}}, \hat{k})$ with both partonic contributions is shown in c). Black lines represent the boundaries between separability and entanglement. All plots are symmetric under the transformation $\theta \to \pi - \theta$ [51].

of this behavior lies in the spin polarizations of the initial gluon pair, that can align in different directions, thereby producing the $t\bar{t}$ pairs in distinct spin states:

- spin-singlet states at threshold, maximally entangled:

$$\rho^{gg}(2m_t, \hat{k}) = |\phi_0\rangle\langle\phi_0|, \qquad |\phi_0\rangle = \frac{|\uparrow\downarrow\rangle - |\downarrow\uparrow\rangle}{\sqrt{2}}$$

- spin-triplet states at very high energies, maximally entangled:

$$\rho^{gg}(\infty, \hat{n}\times\hat{p}) = |\phi_\infty\rangle\langle\phi_\infty|, \qquad |\phi_\infty\rangle = \frac{|\uparrow\downarrow\rangle + |\downarrow\uparrow\rangle}{\sqrt{2}}$$

where the $\uparrow, \downarrow$ indicate the alignment or anti-alignment of the spin with respect to $\hat{n}$ direction. For $q\bar{q}$ annihilation, a similar condition $\Delta^{q\bar{q}}$ is obtained,

$$\Delta^{q\bar{q}} = \frac{\beta^2 \sin^2\theta}{2 - \beta^2 \sin^2\theta} \geq 0 \tag{2.5.28}$$

In this case, entanglement is found in the very high energy regime, as shown in the second plot (b) in Figure 2.5.3, together with plot (c) studying entanglement for the spin density matrix $\rho(m_{t\bar{t}}, \hat{k})$ (see Eq. (2.5.10)), where both contributions are considered. Given the dominance of gg fusion in $t\bar{t}$ production at the LHC, namely $w_{gg}(m_{t\bar{t}}, \hat{k}) \gg w_{q\bar{q}}(m_{t\bar{t}}, \hat{k})$, plots (a) and (c) are very similar.

The application of the Peres-Horodecki separability criterion (Eq. (2.3.8)) to the $t\bar{t}$ spin density matrix leads to four sufficient conditions for entanglement involving the diagonal spin correlation coefficients [59]. Specifically, four entanglement markers can be defined accordingly as in Ref. [14]

$$D^{(1)} = \frac{1}{3}(C_{kk} + C_{rr} + C_{nn}) \tag{2.5.29}$$

$$D^{(k)} = \frac{1}{3}(C_{kk} - C_{rr} - C_{nn}) \tag{2.5.30}$$

$$D^{(r)} = \frac{1}{3}(-C_{kk} + C_{rr} - C_{nn}) \tag{2.5.31}$$

$$D^{(n)} = \frac{1}{3}(-C_{kk} - C_{rr} + C_{nn}) \tag{2.5.32}$$

where $D^{(1)}$ and $D^{(n)}$ are optimal entanglement markers at threshold and in the high-energy regime, respectively. From Eq. 2.3.10, the concurrence can be expressed as

$$\mathcal{C}[\rho] = \frac{\max(0, -1 - 3D_{\min})}{2} \tag{2.5.33}$$

with $D_{\min}$ being the smallest coefficient of the four. Entanglement is present if any of the markers satisfies $D < -\frac{1}{3}$. The conditions for entanglement involving $D^{(1)}$ and $D^{(n)}$ are equivalent to Eq. (2.5.25).

The quantities $D^{(1)}$ and $D^{(n)}$ can be probed in an alternative way rather than from the spin correlation coefficients. In particular, they can be directly measured from the differential cross section characterizing the angular separation between the decay products of the $t\bar{t}$ pair as

$$\frac{1}{\sigma}\frac{d\sigma}{d\cos\theta_{ab}} = \frac{1}{2}(1 + \alpha_a\alpha_b D^{(1)}\cos\theta_{ab}) \tag{2.5.34}$$

$$\frac{1}{\sigma}\frac{d\sigma}{d\cos\theta'_{ab}} = \frac{1}{2}(1 + \alpha_a\alpha_b D^{(n)}\cos\theta'_{ab}). \tag{2.5.35}$$

Here, θ_{ab} is the opening angle between the directions of the daughter particles ($\cos\theta_{ab} = \hat{q_a}\cdot\hat{q_b}$), each defined in the respective parent rest frame. The variable θ'_{ab} represents, instead, the opening angle between the direction $\hat{q}_a$ and a reflection of $\hat{q}_b$ in $(\hat{k},\hat{r})$ plane, defined as $P_{\hat{n}} = \mathrm{diag}(-1,-1,1)$. It is therefore given by $\cos\theta'_{ab} = \hat{q_a}\cdot P_{\hat{n}}\hat{q}_b$ and implies that $D^{(n)} = P_{\hat{n}}D^{(1)}$. Experimentally, both entanglement measures can be obtained as averages over the corresponding angular distributions, namely

$$D^{(1)} = \frac{3}{\alpha_a\alpha_b}\langle\cos\theta_{ab}\rangle, \qquad D^{(n)} = \frac{3}{\alpha_a\alpha_b}\langle\cos\theta'_{ab}\rangle \tag{2.5.36}$$

following the quantum state tomography approach used for $B^{\pm}$ and C in Section 2.5.3.

2.5.6 Magic in $t\bar{t}$ production

In this section, the quantum magic observable presented in Section 2.3.2 is considered in the context of $t\bar{t}$ pair production. To quantify the non-stabilizerness of the $t\bar{t}$ system spin state, M_2 for two-qubit mixed states (see Eq. (2.3.16)) is adopted. It is relevant to recall that this quantity is bounded by $0 \leq M_2(\rho) \leq 1.32$ and that $M_2 = 0$ if ρ is a stabiliser state. Starting from the $t\bar{t}$ spin density matrix of Eq. (2.5.9) and using the Pauli strings defined above, the numerator of Eq. 2.3.16 is computed as

$$\sum_{P\in\mathcal{P}_2}\mathrm{tr}^4[P\rho] = \mathrm{tr}^4[\rho] + \sum_{i=1}^{3}\mathrm{tr}^4[(\sigma_i\otimes\mathbb{I}_2)\rho] + \sum_{j=1}^{3}\mathrm{tr}^4[(\mathbb{I}_2\otimes\sigma_j)\rho] + \sum_{i,j=1}^{3}\mathrm{tr}^4[(\sigma_i\otimes\sigma_j)\rho], \tag{2.5.37}$$

which using the identities in Eq.2.4.3 becomes

$$\sum_{P\in\mathcal{P}_2}\mathrm{tr}^4[P\rho] = 1 + \sum_{i=1}^{3}\left((B_i^+)^4 + (B_i^-)^4\right) + \sum_{i,j=1}^{3}(C_{ij})^4. \tag{2.5.38}$$

The denominator is derived using the same procedure, yielding the final expression for magic as

$$M_2(\rho) = -\log_2\left(\frac{1+\sum_{i=1}^{3}\left[(B_i^+)^4+(B_i^-)^4\right]+\sum_{i,j=1}^{3}(C_{ij})^4}{1+\sum_{i=1}^{3}\left[(B_i^+)^2+(B_i^-)^2\right]+\sum_{i,j=1}^{3}(C_{ij})^2}\right). \tag{2.5.39}$$

At LO in QCD, the same assumptions on the polarization vectors of Section 2.5.5 can be taken, reducing the previous expression to

$$M_2(\rho) = -\log_2\left(\frac{1+\sum_{i,j=1}^{3}(C_{ij})^4}{1+\sum_{i,j=1}^{3}(C_{ij})^2}\right). \tag{2.5.40}$$

Since the $t\bar{t}$ spin density matrix is constructed from the additive contributions of the underlying partonic production mechanisms (2.5.10), the magic observable $M_2(\rho)$ of Eq. 2.5.39 can be evaluated for each initial state $I \in \{gg, q\bar{q}\}$ independently, as previously done for entanglement. This makes it possible to see how each specific interaction contributes to the non-stabilizerness of the system, recalling that at the LHC the dominant contribution is from gg fusion. The distribution of M_2 in the $(\cos\theta, \beta)$ plane for both production modes is shown in Figure 2.5.4. In both cases, the distribution of magic across the phase space differs significantly

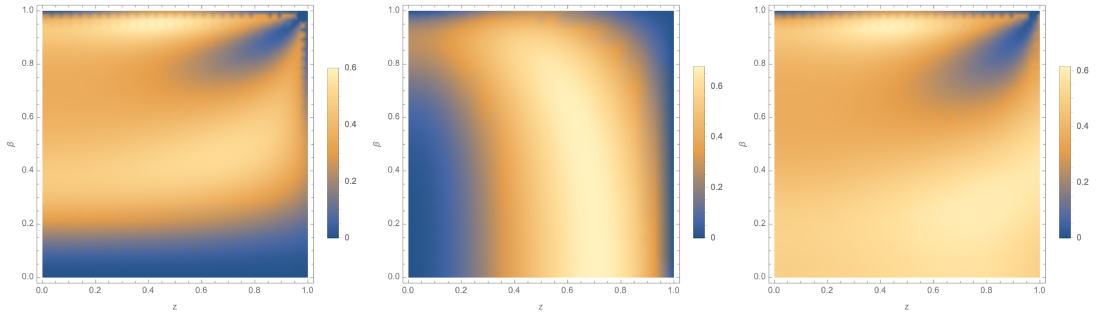

Figure 2.5.4: Magic as a function of β and $z = \cos\theta$, with θ being the production angle, in the $t\bar{t}$ rest frame for gg fusion (left), $q\bar{q}$ annihilation (middle) and both partonic contributions (right) [61].

from that of concurrence, shown in Figure 2.5.3. Specifically, magic is concentrated away from extreme kinematic limits, such as threshold and high-energy regions. This behavior reflects the tendency of the $t\bar{t}$ final state to approach stabilizer states, which are either separable or maximally entangled. Consequently, regions of high magic often correspond to low concurrence, expressing the necessity of both quantities for quantum computational advantage. Given that magic is a non-linear quantity, its distribution across phase space for the combined gg and $q\bar{q}$ initial states (Figure 2.5.4, right panel) cannot be obtained as a simple weighted sum of the individual contributions, unlike concurrence or other linear measures of entanglement. The combined pattern indicates that the final state is non-stabiliser, and thus has non-zero magic, although this quantity still vanishing in the region of high-invariant mass and forward production, similar to the gg channel result.

The study of magic in $t\bar{t}$ production proves that magic top quarks can be produced at colliders. Although stabiliser states, and consequently magic, do not have a clear meaning for particle physics yet, the LHC offers a unique laboratory to investigate this quantity at high energies and, in general, to explore fundamental properties of quantum mechanics that play a crucial role in quantum computation.

2.5.7 Current status of spin and quantum measurements

Spin correlation coefficients Measurements of $t\bar{t}$ spin correlations have been performed at both the Tevatron and the LHC over the past decade, extracting the spin information from the angular distribution of the decay products as discussed in Section 2.5.3. At the Tevatron, the D0 and CDF collaborations provided the first evidence for non-zero spin correlations in $p\bar{p}$ collisions [62–65]. At the LHC, the ATLAS and CMS collaborations have performed increasingly precise measurements in pp collisions in both dileptonic [3–5, 7, 66, 67] and semileptonic channels, confirming the Standard Model predictions up to next-to-leading order (NLO) in QCD. The lepton+jets channel has been explored only recently by CMS [6], using the full Run 2 dataset at $\sqrt{s} = 13$ TeV with and integrated luminosity of 138 fb^{-1}. The analysis has been performed both inclusively and differentially as a function of the $t\bar{t}$ invariant mass, the scattering angle $|\cos\theta|$ and the transverse momentum of the top quark p_T. These observables, with appropriate selections, allow targeting phase-space regions sensitive to entanglement and quantum magic (Figures 2.5.3, 2.5.4). The results in the inclusive case are shown in Figure 2.5.5 as compared to SM predictions at NLO using different Monte Carlo generators.

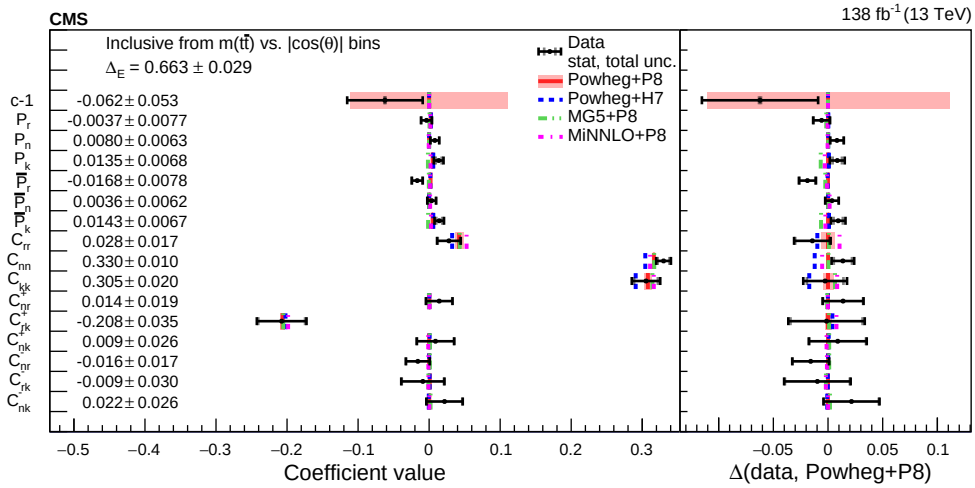

Figure 2.5.5: CMS results of the inclusive full spin density matrix measurement in the semileptonic channel, compared to predictions from various Monte Carlo SM predictions [6].

Magic The previous results have also been recently interpreted by the CMS collaboration to derive the first measurement of magic in $t\bar{t}$ pairs at colliders [10]. The results, in different kinematic regions defined by $m_{t\bar{t}}$ and $|\cos\theta|$, are shown in Figure 2.5.6. Considering only the binning in $m_{t\bar{t}}$, the highest M_2 is observed at

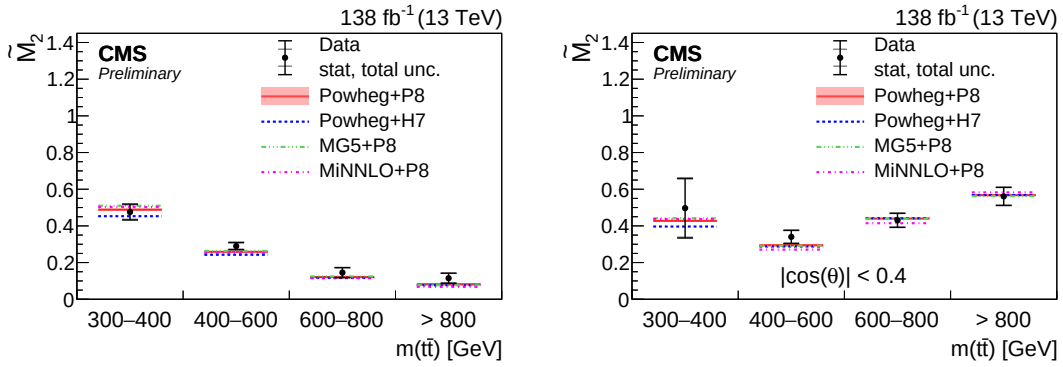

Figure 2.5.6: First observations of magic $M_2 \equiv \tilde{M}_2$ 2.5.39 in top quark pairs by the CMS collaboration [10]. Results of M_2 in bins of $m_{t\bar{t}}$ (left) and in bins of $m_{t\bar{t}}$ with $|\cos\theta| < 0.4$ (right) are shown together with predictions from different MC generators.

the $t\bar{t}$ production threshold and gradually decreases for higher invariant masses. When imposing also $|\cos\theta| < 0.4$, the highest M_2 is found in the boosted region.

Entanglement Spin correlations alone do not necessarily imply the presence of quantum entanglement, as correlations may also arise from classical statistical mixtures. Only recently has it been recognized that the same observables used to measure spin correlations can be interpreted within the framework of quantum information theory, allowing direct tests of entanglement in the $t\bar{t}$ system. The first observation of quantum entanglement between top and antitop quarks at the LHC was reported by the ATLAS collaboration, using dilepton final states from pp collisions at $\sqrt{s} = 13$ TeV with 140 fb^{-1} of integrated luminosity [8]. The measurement, probing the $D^{(1)}$ observable (Eq. 2.5.34), was performed in a narrow interval of the $t\bar{t}$ invariant mass near the production threshold, $340 < m_{t\bar{t}} < 380$ GeV, where entanglement is predicted to be maximal (Figure 2.5.3). This restriction was necessary to enhance the sensitivity to entanglement effects since previous inclusive measurements of the CMS collaboration, averaged over all the phase space, yielded values well above the entanglement limit, namely $D^{(1)} = -0.237 \pm 0.011 > -1/3$ [7]. Figure 2.5.7 (left panel) shows the ATLAS results for $D^{(1)}$ at particle level for three kinematic regions, together with the SM predictions calculated with different MC generators. The entanglement limit shown is a conversion from its parton-level value of $D = -1/3$ to the corresponding value at particle level, in which the $\cos\theta_{ab}$ angle (2.5.34) is modified by hadronization and showering effects. In the threshold region, the measured value is

$$D^{(1)} = -0.537 \pm 0.002\,(\text{stat}) \pm 0.019\,(\text{stat})$$

lying well below the separability bound and indicating entanglement with a very high significance, exceeding 5σ. The regions $380 < m_{t\bar{t}} < 500$ GeV and $m_{t\bar{t}} < 500$ GeV serve as validation regions to test the MC modeling of signal and background and to test the analysis method to remove detector effects and reconstruct the system. As expected, they do not signal entanglement. Regarding the high-boosted

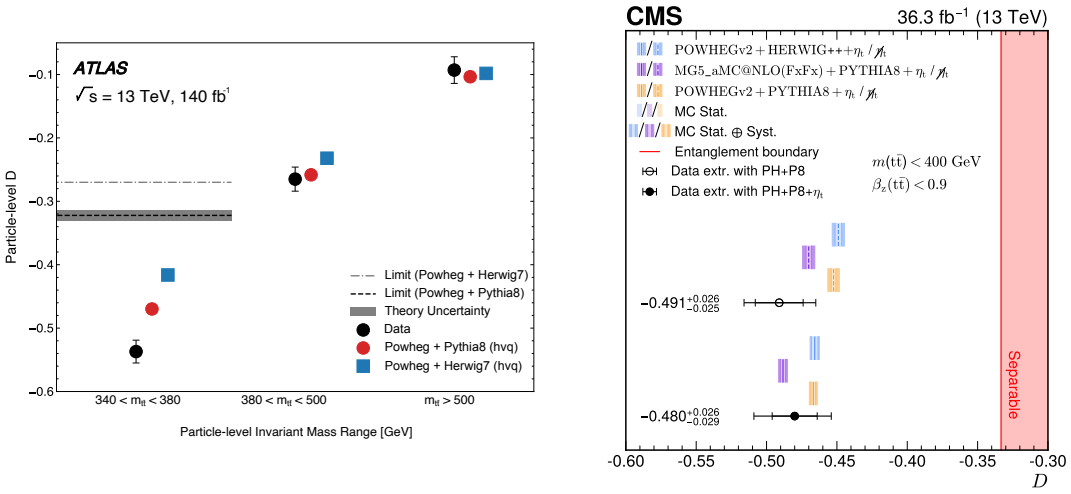

Figure 2.5.7: First observation of entanglement in $t\bar{t}$ pairs by the ATLAS collaboration, showing particle-level results for $D^{(1)}$ compared to SM predictions (left) [8]. Measured entanglement $D^{(1)}$ values compared to MC predictions with and without the inclusion of $t\bar{t}$ bound-state (toponium) effects, performed by the CMS collaboration (right) [9].

region ($m_{t\bar{t}} > 800$ GeV), it was the CMS collaboration that performed the first measurement of quantum entanglement in $t\bar{t}$ pairs [6], completing the picture in both kinematic extremes.

Near threshold, the ATLAS results exhibits a discrepancy between the two generators, as well as a tension between the data and SM predictions that is not present at higher invariant masses, indicating stronger correlations than expected. This suggests that the current modeling does not fully capture the dynamics of $t\bar{t}$ production in this region, requiring a more complete theoretical description at threshold (Section 1.2.4). Building on this, CMS performed a measurement of entanglement for $m_{t\bar{t}} < 340$ GeV using $t\bar{t}$ dileptonic events accounting for $t\bar{t}$ quasi-bound state effects in this region, modeled as a pseudoscalar resonance η_t [9]. The corresponding results are displayed in Figure 2.5.7 (right panel), showing the measured values of $D^{(1)}$ and the predictions with and without the η_t contribution. In both cases, entanglement is observed with a significance exceeding 5σ, but agreement between data and predictions improves when the bound-state effects

are included.

Building on the CMS results of Figure 2.5.7 and the excesses observed at threshold in the differential cross section measurements by ATLAS and CMS (Section 1.2.4), dedicated studies of the $t\bar{t}$ system in this region have been performed by the two collaborations searching for evidences compatible with toponium formation. These analyses exploit angular observables sensitive to the spin correlations and quantum entanglement of the $t\bar{t}$ system. In particular, the observables used are c_{hel} and c_{han}, which correspond to $\cos\theta_{ab}$ defined in Eq. 2.5.34 and $\cos\theta'_{ab}$ defined Eq. 2.5.35, respectively. The c_{hel} distribution has a maximum slope for spin-singlet states, being therefore useful to separate pseudoscalar effects from other contributions. By contrast, c_{han} has a maximum slope for a spin-triplet state. Both collaborations have focused on dileptonic final states.

The CMS collaboration reported the observation of a cross section enhancement near threshold compatible with the production of a colour-singlet pseudoscalar state, as predicted by non-relativistic QCD [15]. The measured production cross section is $\sigma(\eta_t) = 8.8^{+1.2}_{-1.4}$ pb, corresponding to a significance exceeding 5σ. Figure 2.5.8 reports the observed $m_{t\bar{t}}$ distributions in three representative $(c_{\text{hel}}, c_{\text{han}})$ bins out of the nine considered in the analysis, showing agreement between data and fixed-order perturbative QCD (FO pQCD) prediction of $t\bar{t}$ that includes the η_t signal model.

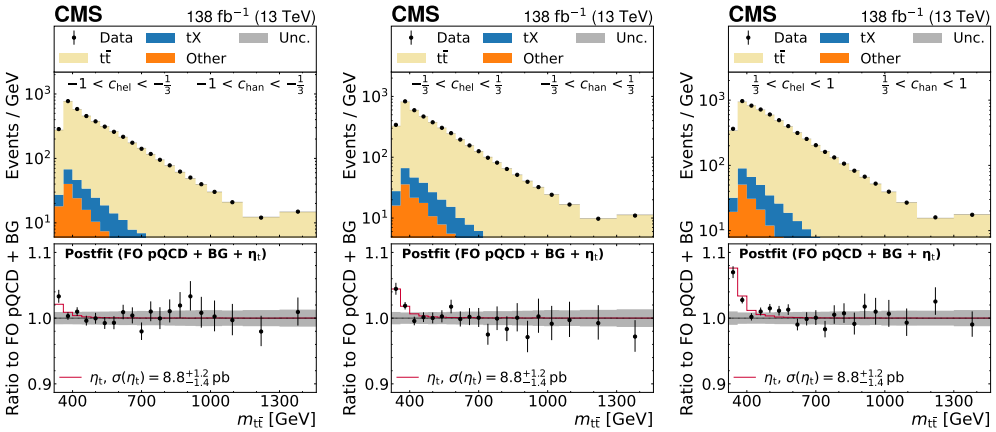

Figure 2.5.8: Reconstructed $m_{t\bar{t}}$ distributions in three representative $(c_{\text{hel}}, c_{\text{han}})$ bins, as measured by the CMS collaboration. The data are shown as points with statistical uncertainties, while the histograms represent the predicted contributions from $t\bar{t}$ production and background processes after the fit. The lower panels show the ratio of the data to the prediction, with the fitted η_t signal contribution overlaid (red line). The gray band indicates the post-fit uncertainty [15].

More recently, the ATLAS collaboration has reported consistent results, observing a similar threshold enhancement compatible with the formation of the same

bound state [16]. The ATLAS analysis focuses on the region $300 < m_{t\bar{t}} < 500$ GeV and uses a more complete model from NRQCD calculation. The corresponding post-fit results are reported in Figure 2.5.9, showing the $m_{t\bar{t}}$ distribution in 9 bins of (c_{hel},c_{han}), with an excess of observed events in the lowest $m_{t\bar{t}}$ bins, particularly at large values of the angular variable c_{hel}. In this case, ATLAS measured a cross section $\sigma(\eta_t) = 9.3^{+1.4}_{-1.3}$ pb, with a significance exceeding 8σ. The results from the two collaborations are in good agreement with each other and with theoretical predictions, providing strong evidence for the formation of a colour-singlet pseudoscalar toponium state near the production threshold.

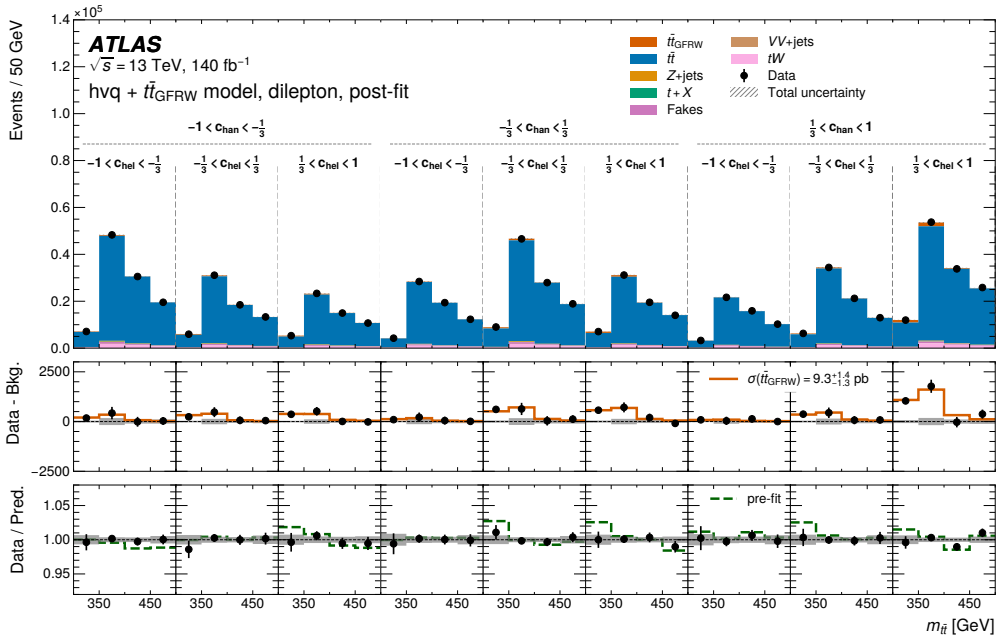

Figure 2.5.9: Post-fit distributions of the reconstructed $m_{t\bar{t}}$ invariant mass in the nine signal regions. The data are compared with the signal and background predictions. The lower panels show the data-background difference and the data-to-prediction ratio [16].

All these results highlight the potential of collider experiments as a unique testing ground for fundamental properties of quantum mechanics, connecting high-energy physics with quantum information and computation fields and motivating further studies to refine measurements and explore other aspects.

3 Analysis of Spin Correlations in the $t\bar{t}$ system

This chapter presents the analysis performed for the first part of the thesis. This stage focuses on the implementation of an analysis routine to reconstruct top and antitop quarks from their decay products in the semileptonic and dileptonic channels, both at parton and particle level. The analysis is applied to simulated $t\bar{t}$ Monte Carlo events. From the reconstructed events, the spin correlation coefficients of the $t\bar{t}$ system are extracted and the quantum magic observable is built from them.

3.1 Monte Carlo simulation

The dataset used in this analysis is generated using Monte Carlo (MC) simulation, a computational method used to generate particle collision events according to theoretical predictions. Detector smearing effects are not included in the simulation.

The $t\bar{t}$ sample is simulated at NLO in QCD using the `POWHEG BOX v2` generator [68–70], a versatile software for simulating hard-scattering processes within both the Standard Model and Beyond Standard Model (BSM) phenomenology. The generated events are subsequently interfaced with `Pythia` [71], a program for the simulation of parton showering, hadronisation processes and decay of unstable particles. This stage is essential for obtaining a realistic description of the final state as observed in real experiments. `Pythia` models both gluon emission and electroweak radiation. The emission of virtual gluon from the coloured partons involved in the hard scattering initiates parton showers, where each gluon can subsequently radiate further gluons or split into $q\bar{q}$ pairs. Electroweak radiation is simulated by modelling photon emission from charged particles, which may generate additional leptons or quark pairs. The partons produced after the showering stage are then bound into colourless hadrons through the hadronisation process. The full event record is passed to the Rivet framework [72], as described in Section 3.2, which processes the events and computes observables at generator level.

The generated sample used in this study consists of approximately 110 000 events of hard scattered $t\bar{t}$ pairs produced from pp collisions at the LHC with a center-of-mass energy of $\sqrt{s} = 13$ TeV. These $t\bar{t}$ pairs in turn decay in either semileptonic or dileptonic final states (see Section 1.2.3). An additional $t\bar{t}$ sample including 690 000 dileptonic-only final states is generated with the same method, to have more statistics in the dileptonic channel. For all samples, the top and antitop quarks considered during the analysis are the last ones in the `Phytia` event record,

taken after gluon radiation and right before their decay.

3.2 Rivet analysis implementation

This section describes the event selection and reconstruction strategy implemented within the Rivet framework [72]. Rivet is a `C++` framework that reads Monte Carlo event records in the HEPMC format and provides the tools required to define physics objects and apply analysis-level selection criteria.

The analysis workflow implemented in Rivet can be summarised as follows. Events are first selected and classified based on their decay topology and according to kinematic and fiducial requirements. The $t\bar{t}$ system is then reconstructed at parton or particle levels (see below). All relevant quantities of the top, antitop and $t\bar{t}$ system are finally written to `ROOT` [73] files, to be used in subsequent stages of the $t\bar{t}$ analysis. For example, distributions of angular observables related to the spin properties of the top and antitop quarks are employed for the extraction of spin correlation coefficients and the computation of quantum observables, such as magic and entanglement.

The analysis is performed at two levels of Monte Carlo simulation: parton level and particle level. At parton level, observables are directly reconstructed from the top quarks and and their decay products taken from the generator event record, after showering, without acceptance requirements on the final states, thus allowing the full phase space to be explored. At particle level, the top quarks, and consequently the observables, are built from semi-stable final-state particles after hadronisation but prior to detector simulation. Physics objects, such as leptons and jets, are reconstructed within a fiducial phase space using selection criteria that closely mimic those applied in the experimental analysis (Section 3.2.1). This ensures that particle-level results incorporate the effects of event selection and reconstruction, while remaining directly comparable with parton-level predictions. A comparison of the invariant mass of the $t\bar{t}$ system between the parton and particle level is shown in Figure 3.2.1.

In the analysis, semileptonic $t\bar{t}$ final states are reconstructed both at parton and particle level, while dileptonic final states are considered only at parton level. For the semileptonic channel, the analysis is further split between the boosted and resolved topologies that will be defined below.

3.2.1 Particle-level object definition

At particle level, physics objects, such as electrons, muons, jets and missing transverse energy, are defined using semi-stable final-state particles from the Monte Carlo event record. Kinematic acceptance requirements are chosen to reflect the typical fiducial coverage of general-purpose LHC detectors, specifically ATLAS,

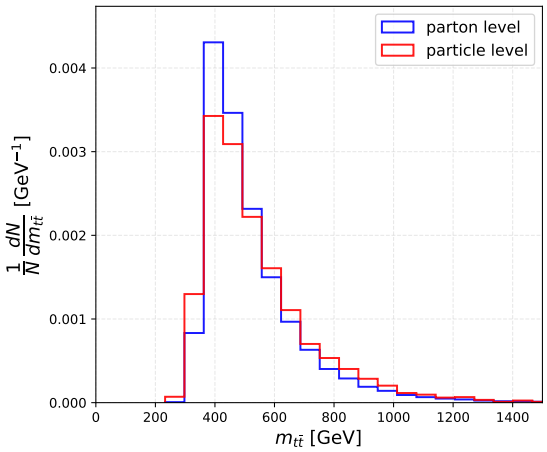

Figure 3.2.1: Distribution of the invariant mass of the $t\bar{t}$ system at parton and particle level.

imposing selection criteria on the transverse momentum p_T, the pseudorapidity η and the angular separation ΔR between two particles in a detector (see Section 1.3.1).

Electrons and muons are reconstructed using the *PromptFinalState* projection in Rivet, which selects leptons originating from the hard scattering process and excludes those from hadron decays. Selected leptons are required to have a transverse momentum $p_T > 27$ GeV and lie within a pseudorapidity range of $|\eta| < 2.5$. To account for final-state QED radiation, leptons are dressed by adding the four-momentum of nearby prompt photons within a radius $\Delta R = 0.1$. This provides a more accurate representation of the lepton kinematics at particle level.

Jets are reconstructed by clustering all stable final-state particles using the *anti-k_T algorithm* [74] with a radius parameter of $R = 0.4$ and are required to have $p_T > 26$ GeV and $|\eta| \leq 2.5$. Jets originating from b-quarks are identified via b-tagging, requiring the presence of a b-hadron with $p_T > 5$ GeV.

For high-momentum (boosted) hadronic top quarks, the decay products are collimated and cannot be fully resolved using small-R jets. The angular separation ΔR of the decay products of a heavy particle with mass m and transverse momentum p_T can be approximated as

$$\Delta R \approx \frac{2m}{p_T}.$$

This implies that, for top quarks with $p_T \gtrsim 300$ GeV, the decay products can be contained within a single jet of radius $R = 1.0$. To reconstruct such large-R jets, small-R jets (with $p_T > 30$ GeV) are reclustered into $R = 1.0$ jets using the anti-k_T

algorithm. The b-tagging information from the small-R constituents is transferred to the large-R jet.

To emulate the overlap removal procedure applied at detector level, leptons found within ΔR of a jet with $p_T > 25$ GeV are removed, ensuring a unique identification of each object as either a jet or a lepton.

The missing transverse energy E_T^{miss} is computed from all visible particles in the event and represents the momentum carried away by neutrinos, which escape the detection. It is defined as

$$E_T^{miss} = -\sum_i p_{T,i}$$

where $p_{T,i}$ is the transverse momentum of the i-th detected particle. This quantity is essential for reconstructing leptonic W boson decays and for estimating the neutrino's longitudinal momentum, which in turn is crucial for accurately reconstructing the leptonic top quark kinematics, as discussed in Section 3.2.2.

3.2.2 Event selection and reconstruction of the $t\bar{t}$ system

At parton level, events are required to contain exactly two top quarks (one t, one $\bar{t}$) and are classified into three decay topologies according to the number of prompt leptons n_{lep} among the decay products: all-hadronic if $n_{lep} = 0$, semileptonic if $n_{lep} = 1$ and dileptonic if $n_{lep} = 2$. All-hadronic events are rejected and not considered in the analysis. These prompt leptons are identified directly in the generator-level event record, which tracks the life of the top quark from its production through various stages of radiation and decay. This ensures an unambiguous assignment to the parent top or antitop. In semileptonic events, the top quark whose decay contains the charged lepton is identified as the leptonic top, while the other top quark is taken to be the hadronic one. Once the final states have been classified, the four-momenta of the top and antitop quarks are then taken from the parton-level record and the $t\bar{t}$ system is reconstructed as the sum of their four-momenta.

At particle level, the classification of the decay mode is taken from the parton level and the physics objects defined in Section 3.2.1 are used to identify and reconstruct the $t\bar{t}$ system. The analysis is implemented for the semileptonic channel with two selection strategies, which correspond to different kinematic regimes. The first is optimized for the *boosted* topology (or *merged* topology), where high-momentum top quarks produce collimated hadronic decay products that merge into a single large-R jet (see Section 3.2.1). The second is designed for the *resolved* topology, in which the three (or four) jets originating from the hadronic top quark decay are sufficiently separated to be individually reconstructed. This strategy maximizes

the reconstruction efficiency of $t\bar{t}$ events across the full kinematic range. This is also relevant for quantum entanglement studies: in $t\bar{t}$ production, entanglement is indeed expected to be present both near threshold and at high energies (see Figure 2.5.3), making both the resolved and boosted topologies essential for its observation. The two topologies are illustrated in Figure 3.2.2.

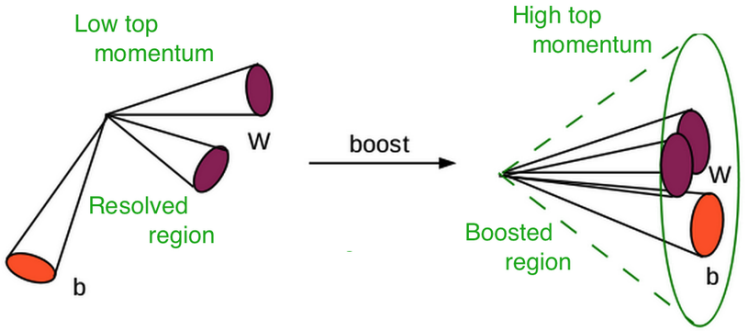

Figure 3.2.2: Resolved and boosted topologies in the hadronic top quark decay.

Firstly, a common pre-selection is applied. On the hadronic side, there must be at least two small-R jets with $p_T > 26$ GeV and $|\eta| < 2.5$. On the leptonic side, all events are required to contain exactly one isolated charged lepton ℓ and satisfy the following criteria:

- $E_T^{miss} > 20$ GeV;
- $E_T^{miss} + m_T(\ell, E_{\mathrm{T}}^{\mathrm{miss}}) > 60$ GeV;
- $m(\ell, b_{lep}) < 180$ GeV

where b_{lep} is the b-tagged jet closest in ΔR to the lepton and m_T is the transverse mass of the lepton-neutrino system, given by $m_T = \sqrt{2p_{\mathrm{T}}^{\ell} E_{\mathrm{T}}^{\mathrm{miss}}(1 - \cos\Delta\phi(\ell, E_{\mathrm{T}}^{\mathrm{miss}}))}$.

After this preliminary selection, the reconstruction of the $t\bar{t}$ system proceeds by checking if the event meets the boosted topology, which targets events with one small-R, b-tagged jet close to the lepton and at least one large-R jet. The latter jet must satisfy all boosted top-tagging criteria: $p_T > 350$ GeV, $|\eta| < 2.0$, $120 < m_{jet} < 220$ GeV and it must contain at least one b-tagged subjet. A separation requirement of $\Delta R(\text{large-R jet}, \ell) > 1.0$ is imposed to avoid overlap with the leptonically decaying top quark. The four-momentum of the large-R jet reconstructs the hadronic top candidate in this topology.

Events failing the boosted selection criteria are evaluated using the resolved topology, which requires explicit reconstruction of the hadronic W boson and top

quark from individual jets. In this case, each event must contain at least four small-R jets, of which exactly two must be b-tagged: the one closest to the lepton is assigned to the leptonic side (b_{lep}) and the other to the hadronic side (b_{had}). The hadronic W boson is reconstructed from light jets (not b-tagged) using either two- or three-jets combinations:

- Two-jets case: for each pair of light jets $\{j_1, j_2\}$, the four-momenta of the W boson and top quark candidates are found as $p_W = p_{j_1} + p_{j_2}$ and $p_{t_{had}} = p_W + p_{b_{had}}$, respectively. From these, the masses m_W and m_t are computed. The optimal combination is selected by minimizing the quantity

  $$\Delta = |m_W - 80.4 \text{ GeV}| + |m_t - 172.5 \text{ GeV}|$$

  where each mass difference is evaluated with respect to the nominal mass value.

- Three-jets case: for each triplet of light jets $\{j_1, j_2, j_3\}$, the compatibility with a hadronic W boson decay is checked by considering all possible two-jet combinations among the three jets, including the full three-jet combination, with invariant masses in the W mass window, $60 < m_{comb} < 100$ GeV. The top quark candidate is then reconstructed by combining the W boson candidate with b_{had}, namely $p_{t_{had}} = p_W + p_{b_{had}}$. The optimal combination is selected by minimizing only the top quark mass difference

  $$\Delta_t = \left| m_t^{(3)} - 172.5 \text{ GeV} \right|,$$

  since in the three-jet combination the third jet might be associated with gluon radiation and may distort the reconstructed W boson mass.

The overall optimal combination is then selected as the one yielding the smallest mass difference, either Δ or Δ_t, over all possible two- and three-jet configurations. The hadronic top candidate is then required to satisfy $120 < m_{t_{\text{had}}} < 220$ GeV. Events in which the best combination involves three light jets are subsequently rejected, as the hadronic polarimeter reconstruction requires exactly two distinct quark directions (Section 3.2.4).

The leptonic top quark candidate is reconstructed identically in both the boosted and resolved topologies, by summing the four-momenta of the W boson and the b_{lep}-jet. However, since only the transverse momentum of the neutrino is accessible through the missing transverse energy E_T^{miss}, its longitudinal component p_z^ν must be inferred. This is achieved by exploiting the four-momentum conservation of the

process $W \to \ell\nu$ and imposing the W boson mass constraint ($m_W = 80.385$ GeV) on the lepton-neutrino system:

$$m_W^2 = (p_\ell^2 + p_\nu^2) = m_\ell^2 + m_\nu^2 + 2(E_\ell E_\nu - \vec{p}_\ell \vec{p}_\nu)$$

where $m_\nu \approx 0$. This leads to a quadratic equation that can be solved for p_z^ν, allowing for the reconstruction of the W candidate. Finally, the leptonic top quark four-momentum is obtained as

$$p_{t_{\text{lep}}} = p_\ell + p_\nu + p_{b_{\text{lep}}}$$

3.2.3 Angular observables reconstruction

The analysis reconstructs the relevant angular observables required for the measurement of spin correlation coefficients. Each observable is defined as the cosine of the angle θ between the momentum of a selected decay product a of the top (or antitop) quark and a chosen spin-quantization axis i of the parent particle, $\cos\theta_a^i$ (Eq. 2.5.17). The decay angles are naturally evaluated in the respective top and antitop rest frames, but the spin axes must be defined in a common reference system in order to allow for meaningful correlation measurements.

In this analysis, a two-stage Lorentz boost procedure is employed. First, the full event is boosted into the $t\bar{t}$ rest frame using

$$\vec{\beta}_{t\bar{t}} = -\frac{\vec{p_t} + \vec{p_{\bar{t}}}}{E_t + E_{\bar{t}}}$$

where $(\vec{p_t}, E_t)$ and $(\vec{p_{\bar{t}}}, E_{\bar{t}})$ denote the four-momenta of the top and antitop quarks in the laboratory frame. In the new frame, the pair is produced back-to-back with equal and opposite momenta, $\vec{p_t^*} = -\vec{p_{\bar{t}}^*} = \vec{p^*}$. The magnitude $|\vec{p^*}| \equiv p^*$ is stored as a kinematic variable and will be used in the second stage of the analysis. The $t\bar{t}$ rest frame provides a natural common basis for defining the spin axes: the helicity basis $\{\hat{k}, \hat{r}, \hat{n}\}$ (Section 2.5.4) is adopted, with the $\hat{k}$ axis defined by the top quark momentum. The same basis is used for both the top and antitop. Then, a second boost is performed from the $t\bar{t}$ rest frame to the individual parent rest frame. It is given by

$$\vec{\beta}_t = -\frac{\vec{p^*}}{E_t^*}, \quad \vec{\beta}_{\bar{t}} = \frac{\vec{p^*}}{E_{\bar{t}}^*}$$

where E_t^* and $E_{\bar{t}}^*$ are the respective energies of the top and antitop quarks in the $t\bar{t}$ rest frame. With the helicity basis choice, this boost is performed along the particle momentum direction and therefore does not induce a Wigner rotation of the spin quantization axis, but rather preserves its orientation. This allows the momenta of the decay products to be consistently projected onto the spin axes, yielding the observables $\cos\theta_{\hat{k}}^a, \cos\theta_{\hat{r}}^a$ and $\cos\theta_{\hat{n}}^a$ required for the spin correlation coefficients computation.

3.2.4 Optimal hadronic polarimeter

The remaining issue is how to select the top quark spin polarimeter among its daughter particles. As stated in Section 2.5.1, the spin analysing power is maximal for charged leptons and down quarks, $\alpha_{\ell^+,\bar{d}} = 1$. Although these particles are perfectly correlated with the spin of the top quark, their experimental observation in top quark decays presents very different challenges. In semileptonic events, the leptonic side provides a well-defined lepton direction, while the hadronic is more challenging: after parton showering and hadronisation, the two quarks from the W boson decay, and in particular the down-type quark of interest, cannot be unambiguously identified.

The analysis explores three methods for constructing a hadronic spin analyzer by combining the directions of q and $\bar{q}'$ in the $W \to q\bar{q}'$ decay: the *optimal hadronic polarimeter* method (chosen for the analysis), the *soft jet* method and the *down-type quark* method.

The optimal hadronic polarimeter construction requires an additional boost, other than the two presented in Section 3.2.3, to the W boson rest frame, where the angle between the reversed b-quark direction ($\hat{z} = -\hat{b}$) and one of the two light quarks (or jets) is computed. This angle is denoted as the W boson helicity angle θ_W and is illustrated for clarity in Figure 3.2.3.

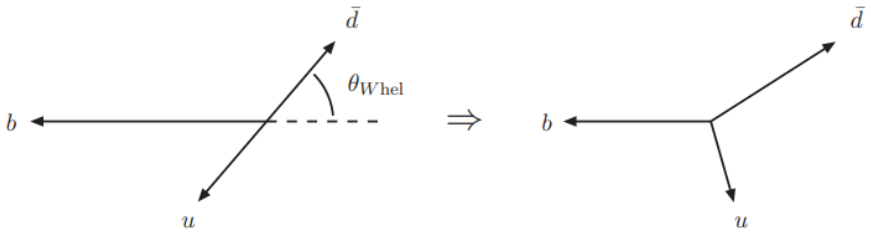

Figure 3.2.3: The three-quark top decay system ($t \to Wb \to q\bar{q}'b$, with $q = u$-type and $\bar{q}' = \bar{d}$-type) as viewed in the W rest frame (left) and boosted back into the parent top rest frame (right). The angle $\theta_{W_{hel}}$, defined as the direction of the d-quark with respect to $-\hat{b}$, is shown in the picture.

In the W boson rest frame, the decay is not symmetric because of the V–A structure of the weak interaction. The distribution of $\cos\theta_W$ indeed depends on the W boson's polarization, as follows:

$$\frac{1}{\Gamma}\frac{d\Gamma}{d\cos\theta_W} = \frac{3}{8}f_R(1+\cos\theta_W)^2 + \frac{3}{8}f_L(1-\cos\theta_W)^2 + \frac{3}{4}f_0(1-\cos\theta_W^2).$$

The quantities $f_R \simeq 0, f_L \simeq 0.30$ and $f_0 \simeq 0.7$ [75] represent the right-handed, left-handed and longitudinal helicity fractions of the W boson in the top quark

frame. For a given measured value of $\cos\theta_W$, this distribution is evaluated at both $\pm|\cos\theta_W|$, corresponding to the two possible assignments of the down-type quark to the harder or softer jet. The resulting values are then normalized to obtain the probabilities p_{hard} and p_{soft}, which quantify the likelihood that the harder or softer jet originates from the down-type quark. After boosting back to the top quark rest frame, the two light jets are ordered by momentum and combined into a weighted polarimeter vector, which represents the optimal hadronic polarimeter:

$$\vec{q}_{opt} = p_{\text{hard}}\hat{q}_{\text{leading}} + p_{\text{soft}}\hat{q}_{\text{subleading}}.$$

Here, $\hat{q}_{\text{leading}}$ and $\hat{q}_{\text{subleading}}$ are the unit vectors of the leading and subleading quarks's three-momenta. The lenght of $\vec{q}_{opt}$ is a measure of the spin analyzing power of this polarimeter, which is evaluated at LO to be $\alpha_{\text{opt}} = 0.64$ [76, 77].

In the soft-jet method, the down-type quark is approximated by selecting the softer of the two light jets in the top rest frame. In this case, the spin analyzing power is $\alpha_{\text{soft}} \simeq 0.5$.

Finally, the down-quark method selects the down-type quark from $W \to u\bar{d}$ or $W \to c\bar{s}$ based on event record. While this would provide maximal analyzing power ($\alpha_d = 1$), it requires explicit identification of the down quark, making this technique very hard to replicate at detector level, given the current status of flavor tagging. In contrast, the implemented analysis framework is designed to operate on generic light jets rather than flavor-tagged quarks. By using the optimal hadronic polarimeter, the analysis mimics what is experimentally accessible and avoids relying on truth labels.

3.3 Measurement of the spin correlation coefficients

As discussed in Section 2.5.3, the reconstruction of the top quark pair spin density matrix relies on quantum tomography using many similar pp collision events yielding $t\bar{t}$ pairs. The Rivet routine described in Section 3.2 indeed runs over many simulated $t\bar{t}$ events. It enables the reconstruction of the events in both semileptonic and dileptonic decay channels but, most importantly, it stores the relevant angular observables needed to compute the elements of the spin density matrix, as discussed in Section 3.2.3. These observables are saved as `ROOT` outputs and later processed with a `Python` script to extract the spin correlation coefficients C_{ij} as in Eq. 2.5.22. The chosen spin quantization basis for this computation is the helicity basis (Section 2.5.4). For each decay channel, the final state particle is selected as discussed in Section 3.2.4, which determines the spin analysing power used in the determination of C_{ij} coefficients.

The measurement of the spin density matrix components has been performed for both semileptonic and dileptonic channels (see next sections). A more detailed

study is presented for the semileptonic case, where both parton and particle levels are analyzed. Results are finally compared with the latest CMS measurements.

3.3.1 Extraction of C_{ij} coefficients using semileptonic events

The measurement of the spin correlation coefficients C_{ij} is performed at both parton and particle level for semileptonic $t\bar{t}$ decays. For this decay channel, $\alpha_a\alpha_b = -0.64$. It is carried out inclusively, which means without further requirements on the kinematic properties of the event, and in kinematic regions defined by selections on two observables: the invariant mass of the $t\bar{t}$ system and the top quark scattering angle θ in $t\bar{t}$ rest frame. In particular, the binning used to define the $m_{t\bar{t}}$ regions is $\{0, 400, 600, 800, 1000\}$ GeV, while for $|\cos\theta|$ it is $\{0, 0.4, 1\}$. The choice of these observables is motivated by their direct connection to the entanglement properties of the $t\bar{t}$ system, as they define the phase-space regions where correlations are stronger (Fig. 2.5.2) and entanglement is expected (Fig. 2.5.3). In particular, regions with $|\cos\theta| < 0.4$, especially at large invariant mass, exhibit enhanced entanglement. Optimizing these observables for the measurement of the spin correlation coefficients therefore enables their study in the most sensitive regions.
All results are reported with their statistical uncertainty, obtained via error propagation.

At parton level, inclusive results are shown in Figure 3.3.1. Figures 3.3.2 and 3.3.3 report the values obtained by selecting different $m_{t\bar{t}}$ regions first without cuts on $\cos\theta$ and imposing $|\cos\theta| < 0.4$, respectively. The results with $|\cos\theta| > 0.4$ are reported in Appendix A.

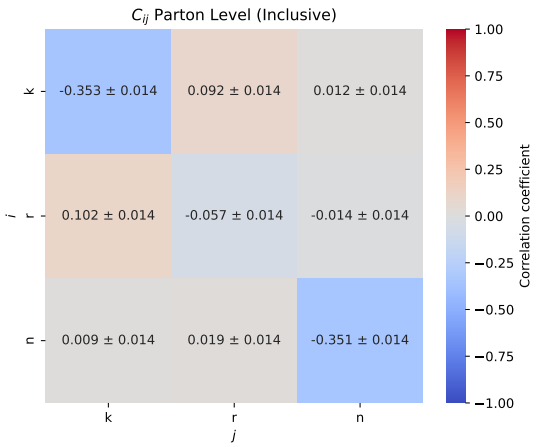

Figure 3.3.1: Results of the inclusive spin correlation coefficients C_{ij} at parton level for the semileptonic decay channel.

The binning of $m_{t\bar{t}}$ and $|\cos\theta|$ is chosen also to replicate the one employed in the latest CMS measurement of the C_{ij} coefficients [6], allowing for a direct comparison and validation of the obtained results. Good consistency is observed, except for an overall sign difference in the matrix elements. This discrepancy arises from the choice of helicity basis: in this analysis, the helicity axis is defined by the top quark direction and used for both top and antitop, whereas CMS defines the helicity basis separately for the two particles. In general, the small differences observed with respect to the CMS measurements are consistent with statistical fluctuations.

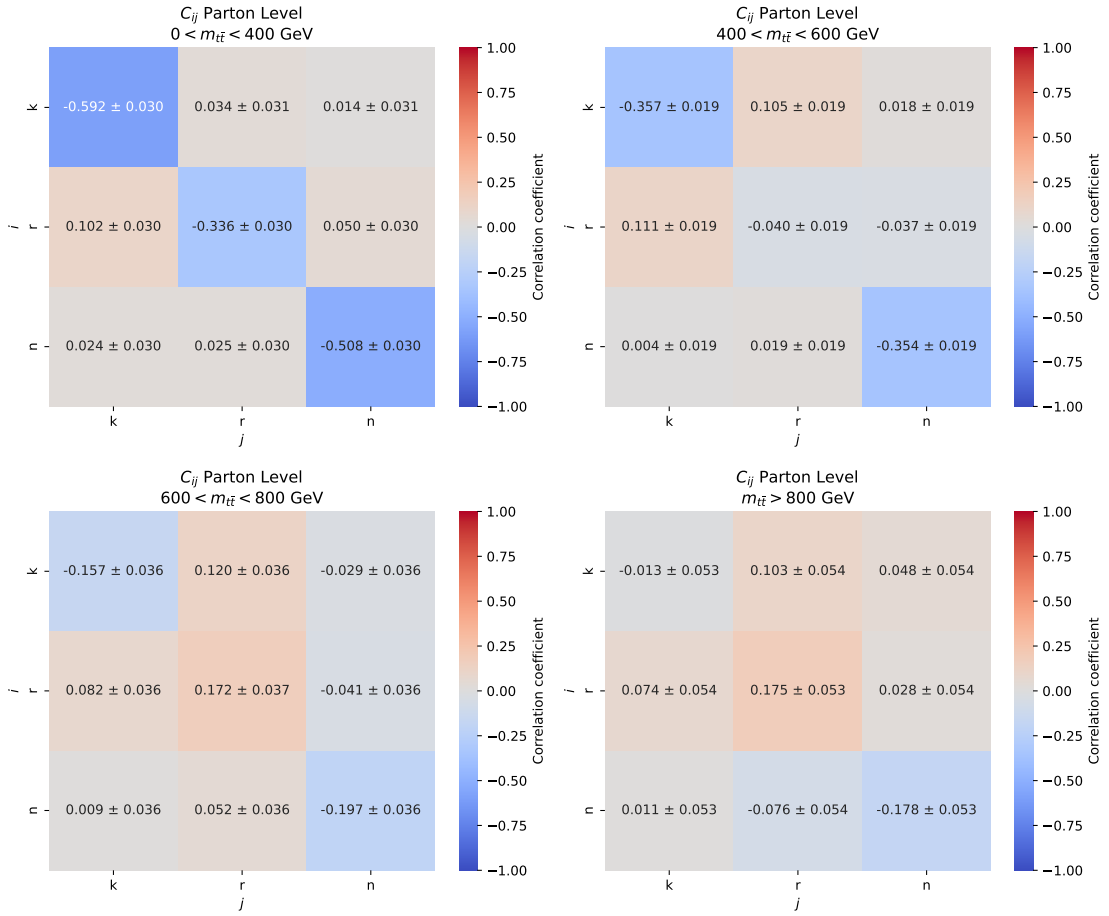

Figure 3.3.2: Results of the spin correlation coefficients C_{ij} at parton level for the semileptonic decay channel for different $m_{t\bar{t}}$ regimes.

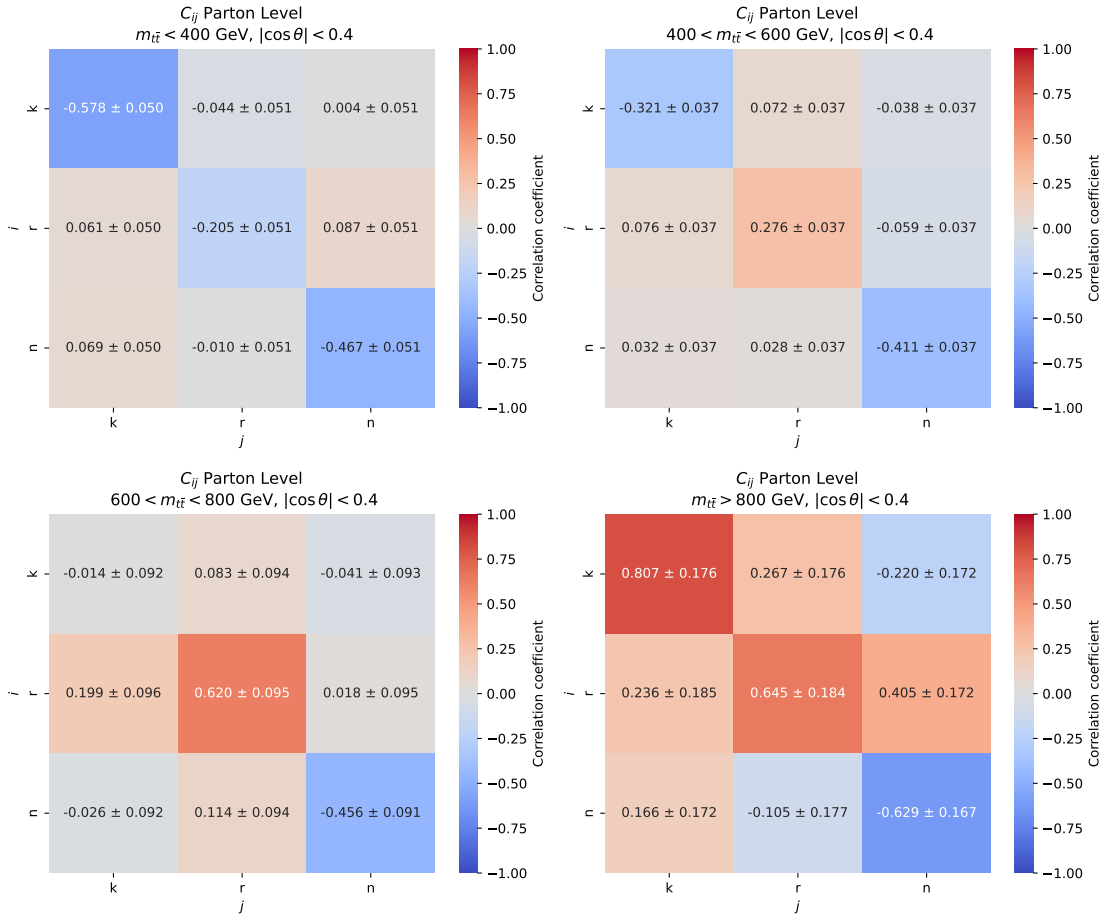

Figure 3.3.3: Results of the spin correlation coefficients C_{ij} at parton level for the semileptonic decay channel for different $m_{t\bar{t}}$ regimes and $|\cos\theta| < 0.4$.

Notably, the near-threshold ($m_{t\bar{t}} < 400$ GeV) and high-boosted ($m_{t\bar{t}} > 800$ GeV with $|\cos\theta < 0.4|$) regions exhibit the largest spin correlations between top and antitop quarks in the $t\bar{t}$ system, as expected in literature from Figure 2.5.2. These enhanced correlations are reflected in the entanglement and concurrence measures, which are found to be particularly high in these regions [51].

At particle level, spin correlation coefficients are computed for both resolved and boosted decay topologies. For each topology, the same selections on $m_{t\bar{t}}$ and $\cos\theta$ applied at parton level are considered. Representative results for the resolved selection are illustrated in Figure 3.2.1. The boosted topology is defined in the high-invariant-mass region, $m_{t\bar{t}} \gtrsim 600 - 800$ GeV. Unfortunately, due to the $p_T > 350$ GeV requirement and the additional analysis cuts, only 2% of the events survive the boosted selection (see Figure 3.2.1).

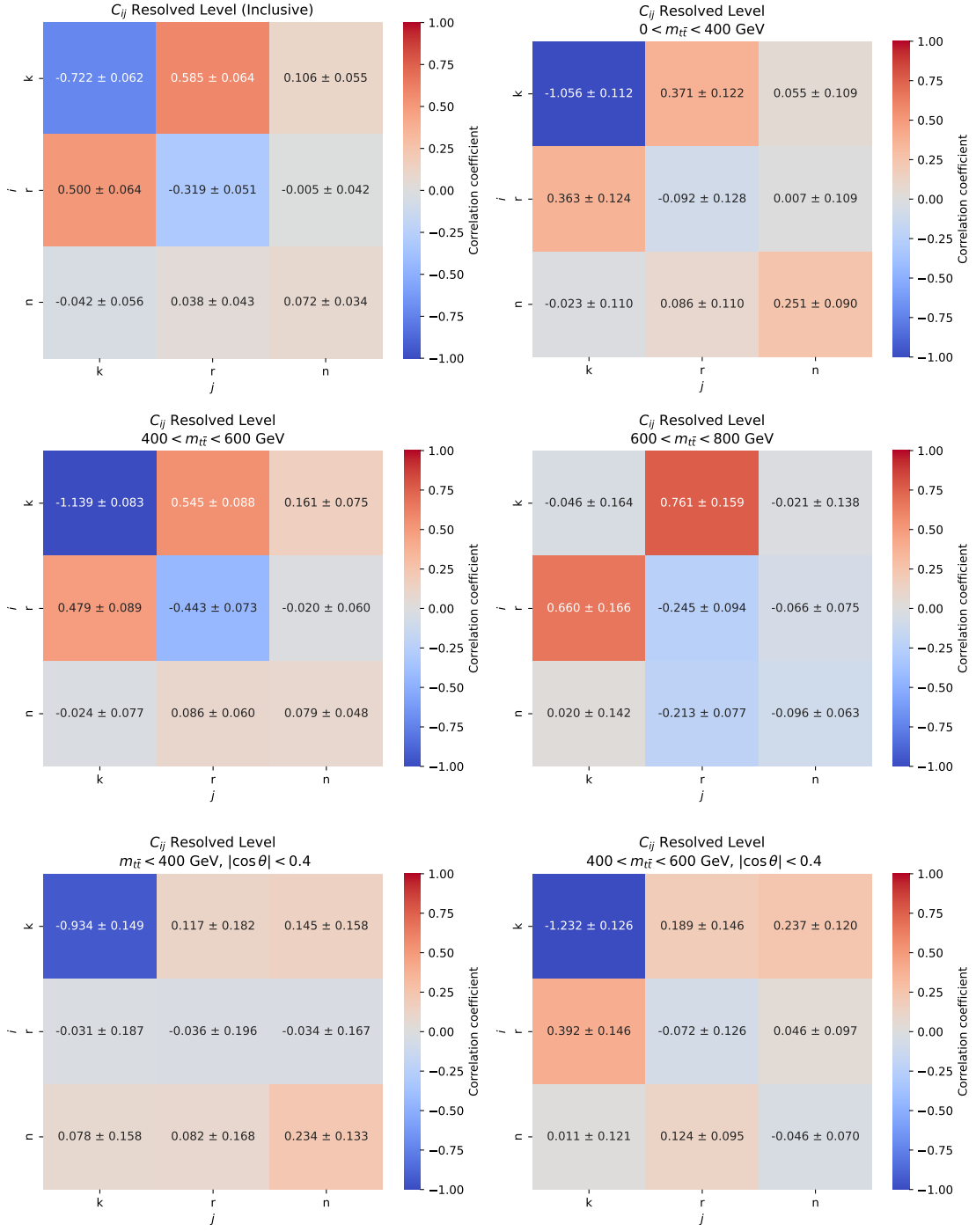

Figure 3.3.4: Results of the spin correlation coefficients C_{ij} at particle level for the semileptonic decay channel in the resolved topology. Different kinematic selections are considered: inclusive, $m_{t\bar{t}} < 400$ GeV (with and without $|\cos\theta| < 0.4$ cut), $400 < m_{t\bar{t}} < 600$ GeV (with and without $|\cos\theta| < 0.4$ cut) and $600 < m_{t\bar{t}} < 800$ GeV.

Consequently, the results obtained for the boosted case are affected by large statistical uncertainties and are less reliable. For this topology, the results corresponding to the inclusive, $600 < m_{t\bar{t}} < 800$ GeV and $m_{t\bar{t}} > 800$ GeV selections are reported in Figure 3.3.5. The values found for the correlation coefficients in the $m_{t\bar{t}} > 800$ GeV region with $|\cos\theta| < 0.4$ can be found in the Appendix A.

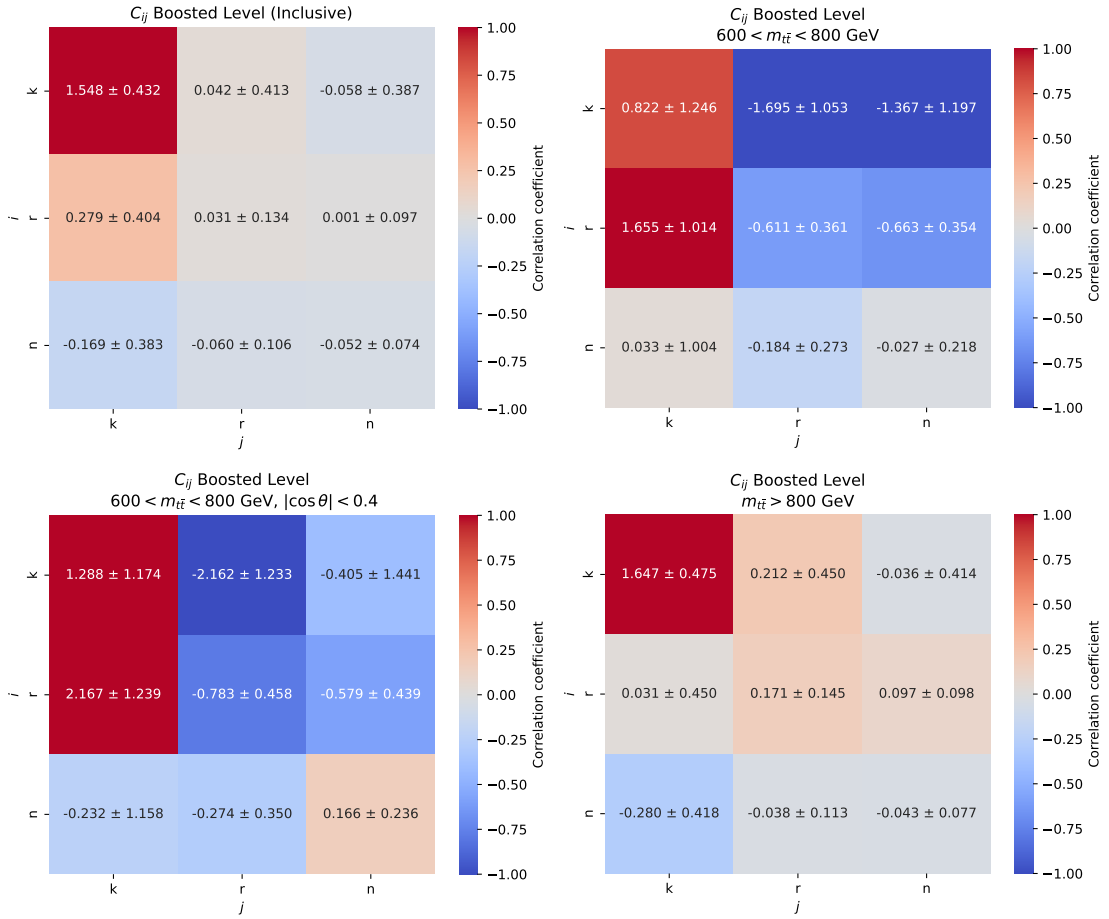

Figure 3.3.5: Results of the spin correlation coefficients C_{ij} at parton level for the semileptonic decay channel for different $m_{t\bar{t}}$ regimes and $|\cos\theta| < 0.4$.

Considering the C_{ij} results for these two topology regimes with respect to the parton level case, it is possible to observe that the reconstruction and event selection significantly distort the spin density matrix at particle level. Consequently, a statistical analysis will be required to remove these effects and recover the parton-level results. Since the resolved and boosted topologies have been explicitly implemented to target the enhanced spin correlations expected in the near-threshold and high-energy regimes, further improvements in the reconstruction and selection

strategy could be developed to better preserve the spin information and enhance sensitivity to entanglement observables at particle level.

3.3.2 Extraction of C_{ij} coefficients using dileptonic decays

In the dileptonic decay channel of the $t\bar{t}$ system, both top quarks decay leptonically, resulting in a final state containing two charged leptons, two neutrinos and two b quarks. In this analysis, the final state is reconstructed only at parton level, with the two leptons as spin analyzers. Therefore, $\alpha_a\alpha_b = -1$. The correlation coefficients are computed according to the same selections used in Section 3.3.1, namely the inclusive selection and in regions defined by cuts applied on $m_{t\bar{t}}$ and $|\cos\theta|$. Representative results for the dileptonic channel are shown in Figure 3.3.6 and are consistent with the measurements reported by the CMS collaboration [7].

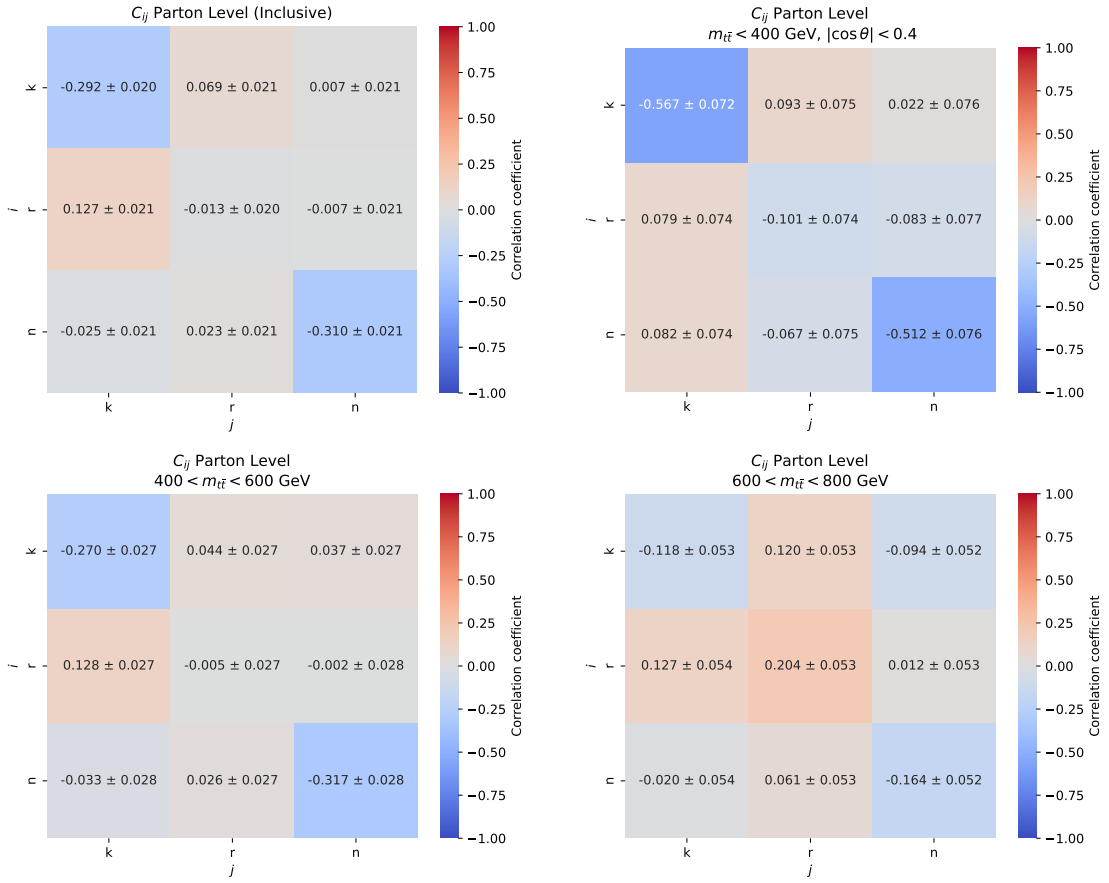

Figure 3.3.6: Results of the spin correlation coefficients C_{ij} at parton level for the dileptonic decay channel for different $m_{t\bar{t}}$ regimes and $|\cos\theta| < 0.4$. The measurements are shown with their statistical uncertainty, obtained via error propagration.

Since the C_{ij} coefficients describe intrinsic properties of the $t\bar{t}$ spin density matrix, they are independent of the decay mode and are therefore expected to be consistent across different final states. Indeed, the results obtained in the dileptonic channel are compatible, within statistical uncertainties, with those from the semileptonic channel. The combined parton-level results from both decay channels are presented in Appendix A.

The precision of the measurements, however, differs between the two channels. The dileptonic mode is affected by reduced event statistics due to its smaller branching fraction, resulting in larger statistical uncertainties. To investigate this effect, a dedicated study was performed using an extended sample of 690,000 dileptonic events. The significant reduction in uncertainties, reported in Table 5, confirms that the observed limitations are primarily driven by statistical constraints rather than by intrinsic reconstruction effects.

Table 5: Inclusive spin correlation coefficients C_{ij} obtained at parton level for the dileptonic channel, using a sample of 690k dileptonic-only events. The measured values are shown with the corresponding statistical uncertainties.

C_{ij} Dileptonic Channel			
	k	r	n
k	-0.313 ± 0.004	0.105 ± 0.004	0.000 ± 0.004
r	0.102 ± 0.004	-0.049 ± 0.004	-0.007 ± 0.004
n	0.003 ± 0.004	0.001 ± 0.004	-0.315 ± 0.004

The results presented in this section, as well as the previous one, exhibit good agreement with the latest CMS measurements [6, 7], validating the Rivet routine described in Section 3.2.

3.4 Computation of quantum magic for the $t\bar{t}$ system

In this section, a study of quantum magic in the $t\bar{t}$ system is presented. This observable is computed directly from the measured spin correlation coefficients reported in Section 3.3, according to Eq. 2.5.40. It is then evaluated in various kinematic regions of the $t\bar{t}$ system, following the same binning in $m_{t\bar{t}}$ and $|\cos\theta|$ used in the spin correlations measurement.

At parton level, the computation is performed for both dileptonic and semileptonic decay channels, with the corresponding results shown in Figure 3.4.1 and Figure 3.4.2. Without the cut on $|\cos\theta|$, the highest value of M_2 is observed at the production threshold of the $t\bar{t}$ pair, for both final states. When the scattering

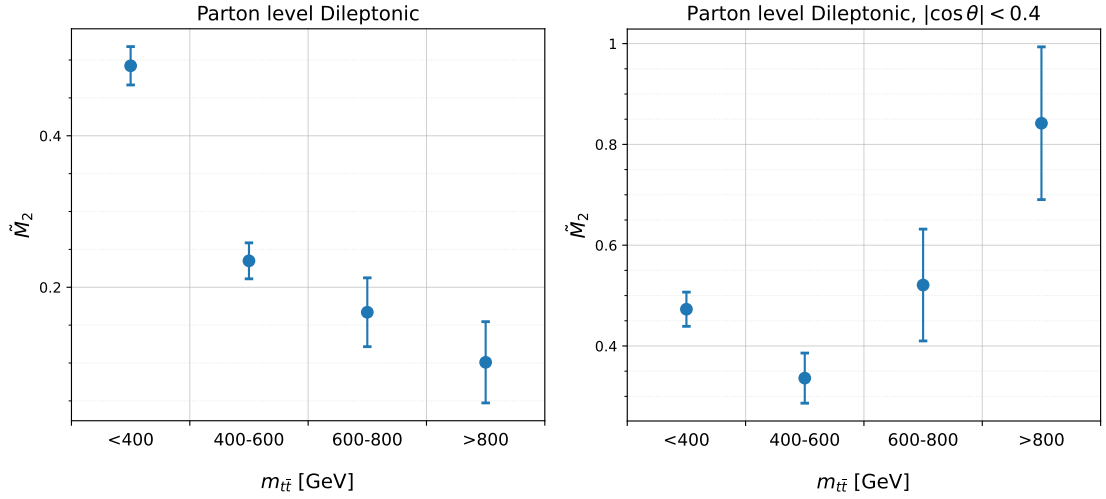

Figure 3.4.1: Results for M_2 in bins of $m_{t\bar{t}}$, obtained using the spin correlation coefficients measured at parton level in the dileptonic channel, shown without (left) and with (right) $|\cos\theta| < 0.4$ cut applied. The measured values are are displayed with their statistical uncertainties (error bars).

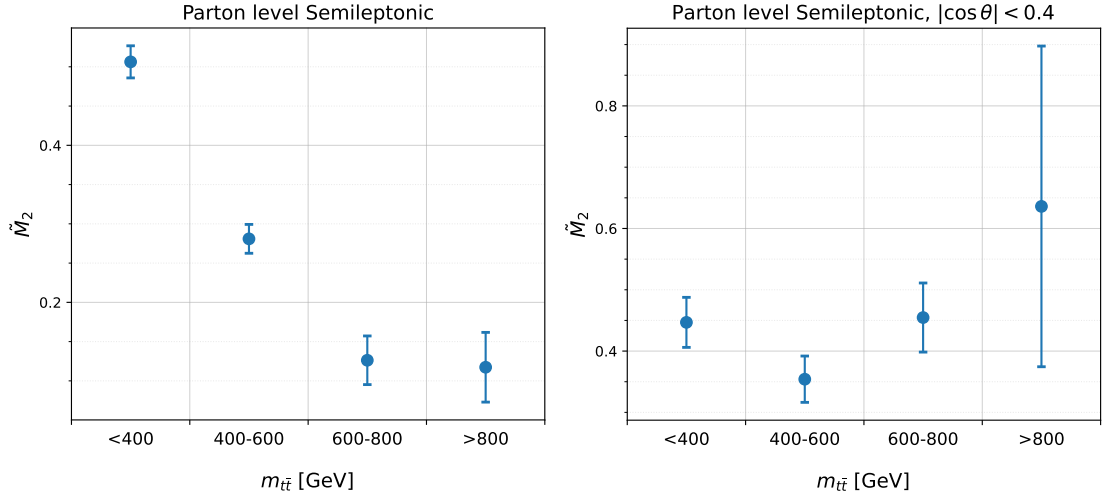

Figure 3.4.2: Results for M_2 in bins of $m_{t\bar{t}}$, obtained using the spin correlation coefficients measured at parton level in the semileptonic channel, shown without (left) and with (right) $|\cos\theta| < 0.4$ cut applied. The measured values are are displayed with their statistical uncertainties (error bars).

angle is restricted to $|\cos\theta| < 0.4$, the observed M_2 behavior seems to be inverted. These results are found to be in agreement with recent CMS measurement, presented in Section 2.5.7, providing further validation of the Rivet analysis routine.

The $m_{t\bar{t}} > 800$ GeV region, especially with the additional $\cos\theta$ cut, suffers from low statistics, explaining the large error bar.

At particle level, magic values are extracted in the semileptonic channel for both resolved and boosted topologies. However, as discussed in Section 3.3.1, the boosted topology suffers from limited statistics, making the magic measurement unreliable. For this reason, only the results obtained for the resolved case are considered and reported in Figure 3.4.3. The $m_{t\bar{t}} > 800$ GeV bin is not reported, since it is related to the boosted regime.

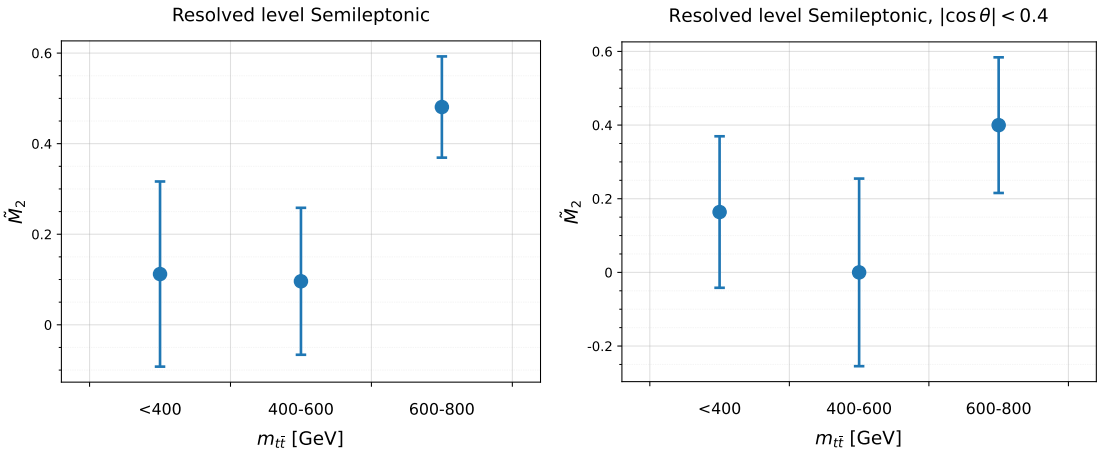

Figure 3.4.3: Results of M_2 in bins of $m_{t\bar{t}}$ in the semileptonic channel for the resolved topology, without (left) and with (right) $|\cos\theta| < 0.4$ cut. Statistical error bars are displayed.

4 Discriminating Toponium Formation in $t\bar{t}$ events

This chapter presents the analysis performed for the second part of the thesis, which has been carried out as part of an Erasmus traineeship in collaboration with *CEA Paris-Saclay*, France. This work constitutes the central contribution of the study published on arXiv as *Extracting a Toponium Signal at the LHC with Spin and Quantum Information Tools* `https://arxiv.org/abs/2602.23426v1`. This stage investigates whether spin and quantum observables can be used to discriminate between standard $t\bar{t}$ production and $t\bar{t}$ events which include toponium formation effects at threshold. This restricts the analysis to the invariant mass region $m_{t\bar{t}} < 355$ GeV. The same Rivet framework presented in Section 3.2 is applied to the respective Monte Carlo samples, generated only in the dileptonic channel. This final state is chosen for its clean signature and direct sensitivity to top and antitop spins, suitable for this preliminary study. The analysis is performed at parton level and begins with the reconstruction of the spin density matrix for both systems, followed by the computation of some quantum observables. Then a detailed study of the separation power of kinematic, angular and quantum information-inspired observables is conducted. Finally, a Boosted Decision Tree (BDT) is trained and tested to combine these observables and enhance the separation between toponium signal and conventional $t\bar{t}$ background.

4.1 Monte Carlo simulation and event reconstruction

The datasets used in this analysis are generated using Monte Carlo simulations without including detector effects and are studied at parton level. For the purpose of the analysis, two samples are required: one for conventional SM $t\bar{t}$ events and an additional sample that reproduces toponium effects in the threshold region of $t\bar{t}$ production. Both are simulated at a center-of-mass energy of $\sqrt{s} = 13$ TeV, with $t\bar{t}$ pairs decaying in the dileptonic final state:

$$t\bar{t} \to W^+bW^-\bar{b} \to l^+\nu bl^-\bar{\nu}\bar{b}.$$

The standard $t\bar{t}$ sample is generated as described in Section 3.1. For the toponium sample, the hard-scattering process $pp \to t\bar{t}$ and the subsequent decays are generated using `MG5_aMC@NLO` [78]. Toponium formation effects are incorporated at LO through a recently developed event-reweighting procedure applied to the standard Monte Carlo events [13]. This is applied exclusively in the near-threshold region of the $t\bar{t}$ invariant mass, where non-relativistic dynamics dominate and bound-state effects are expected to appear. The kinematic distributions of the system and

spin correlations are modified only in this region. The events from both samples are subsequently passed to `Pythia` for parton showering and hadronisation (see Section 3.1) and the full event records are stored in HEPMC format [79] for processing with the Rivet routine described in Section 3.2. The reconstruction of the $t\bar{t}$ system is performed at parton level and final-state particles, namely leptons and b-quarks used for the selection cuts described in Section 4.1.1, are assigned to their parent top or antitop quarks using truth-level decay information from the event record.

As in the previous analysis, the top and antitop quarks are the last ones in the event record, taken after gluon radiation and right before their decay. Their momenta therefore include the effects of final-state radiation (FSR), although this has no significant impact on the observables considered in the analysis. All the decay products are instead before FSR at born level, so photons close to leptons are not considered.

The number of events for each sample is reported in Table 6. To enable a meaningful comparison between the two systems, the analysis is restricted to the region close to the $t\bar{t}$ production threshold, where toponium effects are present. The $t\bar{t}$ sample is generated in a broader invariant mass range and its statistics is significantly reduced after this selection. It should be noted that, in the toponium generation, `MG5_aMC@NLO` does not populate the invariant mass region above 350 GeV. However, parton shower effects induce a smearing of the $m_{t\bar{t}}$ distribution, leading to a partial repopulation of the phase space at slightly larger $m_{t\bar{t}}$ values. For this reason, events with $m_{t\bar{t}} < 355$ GeV are selected, which also allows the recovery of additional events in the reduced $t\bar{t}$-only sample.

	$t\bar{t}$	Toponium
Total	3.15 million	292 327
After $m_{t\bar{t}}$ cut	93 048	292 327

Table 6: Number of events before and after $m_{t\bar{t}} < 355$ GeV selection cut, for conventional $t\bar{t}$ and toponium samples.

4.1.1 Normalization and final-state analysis cuts

The event samples obtained via MC generation are not scaled to physical cross sections and luminosities. To obtain realistic expected event yields, the samples are normalized using the production cross sections $\sigma_{t\bar{t}} = 833.9$ pb and $\sigma_{\text{toponium}} = 6.43$ pb, an integrated luminosity of $140\,\text{fb}^{-1}$ and a dileptonic branching ratio of $BR = 0.105$. These cross section values correspond to NNLO computation for standard $t\bar{t}$ [33] and LO for toponium [42]. Each event is assigned an individual

generator-level weight[4] ω_i in the Rivet analysis, representing the probability of that event in the simulated sample and accounting for effects such as PDF variations or scale choices, and scaled by the normalization factor N, defined as

$$N = \frac{\sigma \cdot L \cdot BR}{\sum_i \omega_i}$$

The normalized contribution of each event is therefore given by $N\omega_i$. This procedure is applied throughout the analysis to construct the distributions of the relevant observables and to compute the performance metrics. Figure 4.1.1 shows a comparison of the $m_{t\bar{t}}$ distributions for the $t\bar{t}$ and toponium samples correctly normalized, before and after the $m_{t\bar{t}} < 355$ GeV cut.

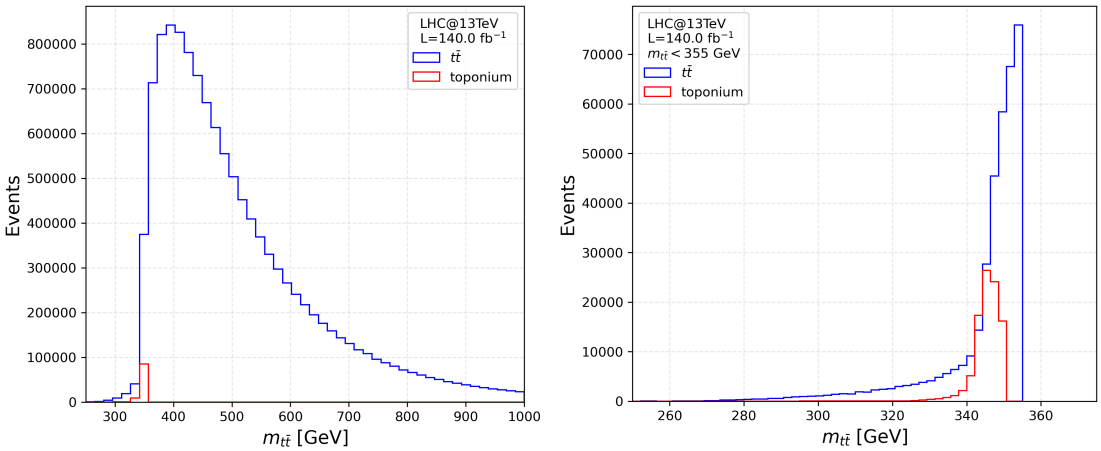

Figure 4.1.1: Distribution of the invariant mass $m_{t\bar{t}}$ for both $t\bar{t}$ and toponium samples before and after applying the $m_{t\bar{t}} < 355$ GeV cut. The simulated number of events, after the $m_{t\bar{t}}$ cut and weighted by the physical normalization, can be found in Table 8, under *Total*.

The analysis also applies selection criteria similar to those used in collider experiments analyzing real data in the dilepton final state. The lepton requirements are either:

1. both with $|\eta| < 2.5$ and at least one with $p_{\mathrm{T}} > 25$ GeV;
2. both with $|\eta| < 2.5$ and $p_{\mathrm{T}} > 20$ GeV.

[4]It corresponds to the relative probability of producing a specific event according to the theoretical model used in the simulation as a function of the matrix element, scale and PDF choices.

The first selection is used to simulate a single lepton trigger requirement adopted during the 2022-2025 Run3 data taking by the ATLAS experiment [80], while the second one mimics a dilepton trigger.

These lepton selections are combined with criteria on the b-quarks. In a $t\bar{t}$ event, at least two b-quarks are generated. The requirements on these objects are $p_{\mathrm{T}} > 25$ GeV and $|\eta| < 2.5$. The pseudorapidity range reflects the practical limitation of b-tagging algorithms, which are typically applied only within the central region of the detector. Table 7 reports the number of events from the MC samples in the invariant mass region $m_{t\bar{t}} < 355$ GeV for the standard $t\bar{t}$ sample and for the toponium sample. Table 8 presents the expected number of events after normalisation. The event counts are shown both before and after the application of the previously described lepton and b-quark selection cuts.

	$t\bar{t}$	Toponium	$\varepsilon_{\mathrm{c}}^{t\bar{t}}$	$\varepsilon_{\mathrm{c}}^{\mathrm{topo}}$
Total	93048	292327	2.95%	100%
Selection (1)	74020	239965	2.35% (79.6%)	82.1%
Selection (a)	54085	190574	1.72% (58.1%)	65.2%
Selection (2)	58298	189154	1.85% (62.7%)	64.7%
Selection (b)	42395	149385	1.35% (45.6%)	51.1%

Table 7: Number of events from the MC samples in $m_{t\bar{t}} < 355$ GeV region, before (*Total*) and after applying different final-state selection cuts: (1) $|\eta| < 2.5$ for both leptons and $p_T > 25$ GeV for at least one lepton; (a) same as (1) with additional $|\eta| < 2.5$ and $p_T > 25$ GeV requirements for both b-quarks; (2) $|\eta| < 2.5$ and $p_T > 20$ GeV for both leptons; (b) same as (2) with additional $|\eta| < 2.5$ and $p_T > 25$ GeV requirements for both b-quarks. The corresponding cut efficiency for $t\bar{t}$ ($\varepsilon_{\mathrm{c}}^{t\bar{t}}$) and toponium ($\varepsilon_{\mathrm{c}}^{\mathrm{topo}}$) is reported in the table, including both the $m_{t\bar{t}}$ and final-state cuts. The values in parentheses are computed with respect to the $t\bar{t}$ count after $m_{t\bar{t}}$ cut.

	$t\bar{t}$	Toponium
Total	364083.6	94520.5
Selection (a)	211992.8	61619.9
Selection (b)	166174.4	48301.9

Table 8: Event yields in $m_{t\bar{t}} < 355$ GeV region, after normalization and different final-state selection cuts: (a) $|\eta| < 2.5$ for both leptons and $p_T > 25$ GeV for at least one lepton, $|\eta| < 2.5$ and $p_T > 25$ GeV for both b-quarks; (b) $|\eta| < 2.5$ and $p_T > 20$ GeV for both leptons, same requirements of (a) for the b-quarks.

As will be shown in Section 4.4, the final-state selection cuts do not distort the distributions of the observables under study, as their effect is limited to a reduction in statistics.

4.2 Measurement of spin correlations for $t\bar{t}$ and toponium systems

This section and the following one investigate whether spin correlations, together with quantum observables, can be used to discriminate between standard $t\bar{t}$ production and $t\bar{t}$ production in the presence of toponium effects. The underlying idea is that the formation of a toponium bound state near threshold inevitably modifies the spin structure of the $t\bar{t}$ system and, consequently, the quantum information encoded in the final state. The strategy adopted for the measurement of the correlation coefficients follows that used in Section 3.3. The analysis is restricted to the $m_{t\bar{t}} < 355$ GeV region without requirements $\cos\theta$.

The spin density matrix has been reconstructed for the $t\bar{t}$ sample, for the toponium sample and for their weighted combination using the corresponding cross section values reported in Section 4.1.1. The weighted combination provides a realistic representation of actual collision events, in which the toponium signal is superimposed on a significant $t\bar{t}$ background. The results for the spin correlation coefficients are shown in Table 9. As can be seen from the table, the spin

Table 9: Spin correlation coefficients C_{ij} for dileptonic $t\bar{t}$ production near threshold ($m_{t\bar{t}} < 355$ GeV), shown for the standard $t\bar{t}$ sample, the toponium sample and their weighted combination (*Combined*). The values are shown with the corresponding statistical uncertainty, computed via error propagation.

	$t\bar{t}$	Toponium	Combined
C_{kk}	-0.5003 ± 0.0097	-0.9594 ± 0.0053	-0.5954 ± 0.0077
C_{kr}	0.0635 ± 0.0098	0.0113 ± 0.0056	0.0527 ± 0.0079
C_{kn}	-0.0034 ± 0.0099	0.0027 ± 0.0055	-0.0021 ± 0.0079
C_{rk}	0.0766 ± 0.0098	0.0094 ± 0.0056	0.0626 ± 0.0079
C_{rr}	-0.3903 ± 0.0098	-0.8965 ± 0.0053	-0.4951 ± 0.0078
C_{rn}	-0.0145 ± 0.0098	-0.0040 ± 0.0055	-0.0123 ± 0.0079
C_{nk}	0.0133 ± 0.0098	-0.0030 ± 0.0056	0.0100 ± 0.0078
C_{nr}	0.0007 ± 0.0098	0.0030 ± 0.0055	0.0012 ± 0.0079
C_{nn}	-0.5547 ± 0.0097	-0.9224 ± 0.0053	-0.6308 ± 0.0077

correlation coefficients yields very different values for the $t\bar{t}$ and toponium samples, especially for the diagonal terms, which vary by nearly a factor of two. This highlights the distinct spin structure of the two systems. For the toponium sample, the C-matrix approaches $-\mathbb{I}_3$, reflecting the bound-state nature of toponium formation near threshold, where the spin correlations of the top and antitop are strongly enhanced. For continuum $t\bar{t}$ production, the correlations between top and

antitop spins are weaker, reflecting a more independent production of the two particles. The combined results illustrate the overall enhancement of spin correlations induced by toponium, as would be observed in a real measurement.

4.3 Computation of quantum observables for $t\bar{t}$ and toponium systems

Using the spin correlation coefficients measured in the previous section (Table 9), it is possible to study quantum observables. The purpose of this analysis is to examine whether the modifications in spin correlations caused by toponium formation translate into measurable differences in the reconstructed quantum state. If this is the case, then these observables may offer additional insight beyond spin correlation measurements and could help in probing toponium effects in $t\bar{t}$ production.

The observables considered are the entanglement measure $D^{(1)}$ and the magic quantity M_2, computed using Eq. 2.5.29 and Eq. 2.5.40, respectively. Although $D^{(1)}$ provides the optimal entanglement marker at threshold, which is the region of interest, the additional measures $D^{(k)}, D^{(r)}$ and $D^{(n)}$ are also evaluated using Eq. 2.5.30, Eq. 2.5.31 and Eq. 2.5.32. Their values have been determined for the $t\bar{t}$ sample, for the toponium sample and for their weighted combination, defined in Section 4.2. The results are reported in Table 10. As shown in the table,

Table 10: Measured values of $D^{(1)}, D^{(k)}, D^{(r)}, D^{(n)}$ and M_2 for dileptonic $t\bar{t}$ production near threshold ($m_{t\bar{t}} < 355$ GeV), shown for the standard $t\bar{t}$ sample, the toponium sample and their weighted combination (*Combined*). The values are shown with the corresponding statistical uncertainty, obtained via error propagation.

	$t\bar{t}$	Toponium	Combined
$D^{(1)}$	-0.4818 ± 0.0057	-0.9261 ± 0.0031	-0.8188 ± 0.0027
$D^{(k)}$	0.1482 ± 0.0056	0.2865 ± 0.0030	0.2531 ± 0.0027
$D^{(n)}$	0.2216 ± 0.0056	0.3284 ± 0.0030	0.3026 ± 0.0027
$D^{(r)}$	0.1120 ± 0.0056	0.3112 ± 0.0031	0.2631 ± 0.0027
M_2	0.5481 ± 0.0051	0.1525 ± 0.0069	0.3537 ± 0.0047

all the observables take distinct values for the $t\bar{t}$ and toponium samples. In the presence of toponium, the entanglement measures $D^{(i)}$ (with $i = 1, k, r, n$) are significantly enhanced with respect to the continuum $t\bar{t}$ case. This behaviour can be traced back to their dependence on the diagonal components of the spin correlation matrix, which were found to increase by nearly a factor of two when

toponium effects are included. By contrast, quantum magic exhibits an opposite trend: as entanglement increases, magic is reduced when considering toponium formation. For all quantities, the weighted combination of $t\bar{t}$ and toponium remains enhanced relative to the continuum case, showing that these quantum observables would provide sensitivity also in more realistic experimental conditions.

Notably, for all samples the entanglement witness $D^{(1)}$ satisfies the condition $D^{(1)} < -1/3$, confirming that $t\bar{t}$ system near threshold is indeed entangled 2.5.5. Another ensemble-level quantity inspired by quantum magic will be introduced and studied in Section 4.4.2.

4.4 Study of per-event discriminating observables

As discussed in Section 4.2, the formation of toponium alters the spin structure of $t\bar{t}$ compared to the continuum. While the previous sections focused on the extraction of single integrated quantities, such as spin correlation coefficients and quantum information measures, the present analysis adopts a per-event approach, exploiting the characteristic distortions induced by the formation of a bound state in the angular and kinematic distributions of the decay products.

This section presents a detailed study of a set of observables which could probe these variations, investigating their ability to discriminate between standard $t\bar{t}$ production and toponium formation. They are grouped into two main classes: kinematics-based observables (Section 4.4.1) and quantum information-inspired ones (Section 4.4.2). All observables are constructed on an event-by-event basis, allowing both for individual performance studies and for their use in a multivariate analysis. In addition, the correlations among the variables are studied.
The analysis is performed in the $m_{t\bar{t}} < 355$ GeV region and compares the distributions of the observables for the $t\bar{t}$ and toponium samples, previously described in Section 4.1. All variables are initially shown without physical normalization and final-state selections to highlight intrinsic differences between continuum $t\bar{t}$ and toponium production. Normalization and cuts are applied afterward to test whether these effects remain visible in a more realistic scenario (see Section 4.4.4).

4.4.1 Kinematic observables

This section explores observables derived from $t\bar{t}$ kinematics, investigating whether they are modified in the presence of toponium. Standard kinematic and angular variables are first examined. Subsequently, some observables sensitive to correlations between the top and antitop momenta are studied.

The first standard observables to be considered are evaluated in the laboratory

frame and include the magnitudes of the individual three-momenta, their transverse component, their projections onto the x and z axes and the magnitude of the total momentum of the system, $\vec{p}_{t\bar{t}}$. Their distributions provide an overview of the event kinematics for both $t\bar{t}$ and toponium samples and are shown in Figure 4.4.1.

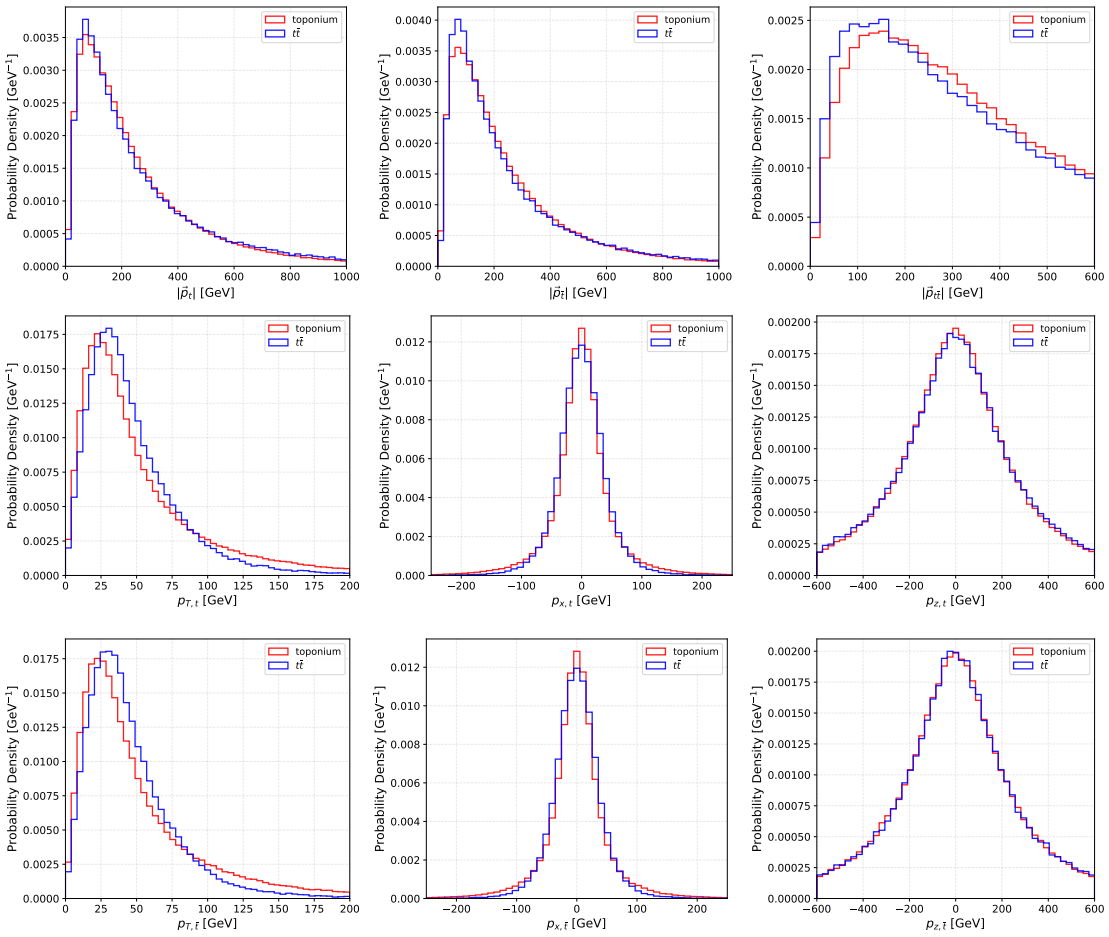

Figure 4.4.1: Probability density distributions of various kinematic variables derived from the momenta of the top and antitop quarks in the laboratory frame, $\vec{p}_t$ and $\vec{p}_{\bar{t}}$. These include the magnitudes of the individual momenta, their transverse component p_T and their projection onto the x and z axes. Also shown is the distribution of the magnitude of the total momentum of the $t\bar{t}$ system, where $\vec{p}_{t\bar{t}} = \vec{p}_t + \vec{p}_{\bar{t}}$. Results are presented for conventional $t\bar{t}$ events and simulated toponium-only events, for $m_{t\bar{t}} < 355$ GeV.

This study indicates that the only significant differences between the two systems appear in the transverse momenta p_T of the top and antitop quarks, which are shifted towards higher values in continuum $t\bar{t}$, and in the magnitude of the

total momentum $|\vec{p}_{t\bar{t}}|$, which shows the opposite trend and suggests that toponium is more boosted in the laboratory frame compared to conventional $t\bar{t}$.

Angular separations between the top and antitop quarks in the laboratory frame could be sensitive to toponium formation and are therefore explored. They include ΔR, $\Delta\phi$ and $\Delta\eta$, defined in Section 3.2.1. The magnitude of the top quark momentum in the $t\bar{t}$ rest frame, denoted as p^*, is also studied. All distributions are displayed in Figure 4.4.2 and exhibit significant differences between $t\bar{t}$ and toponium samples. In particular, ΔR and $\Delta\phi$ are peaked towards lower values for

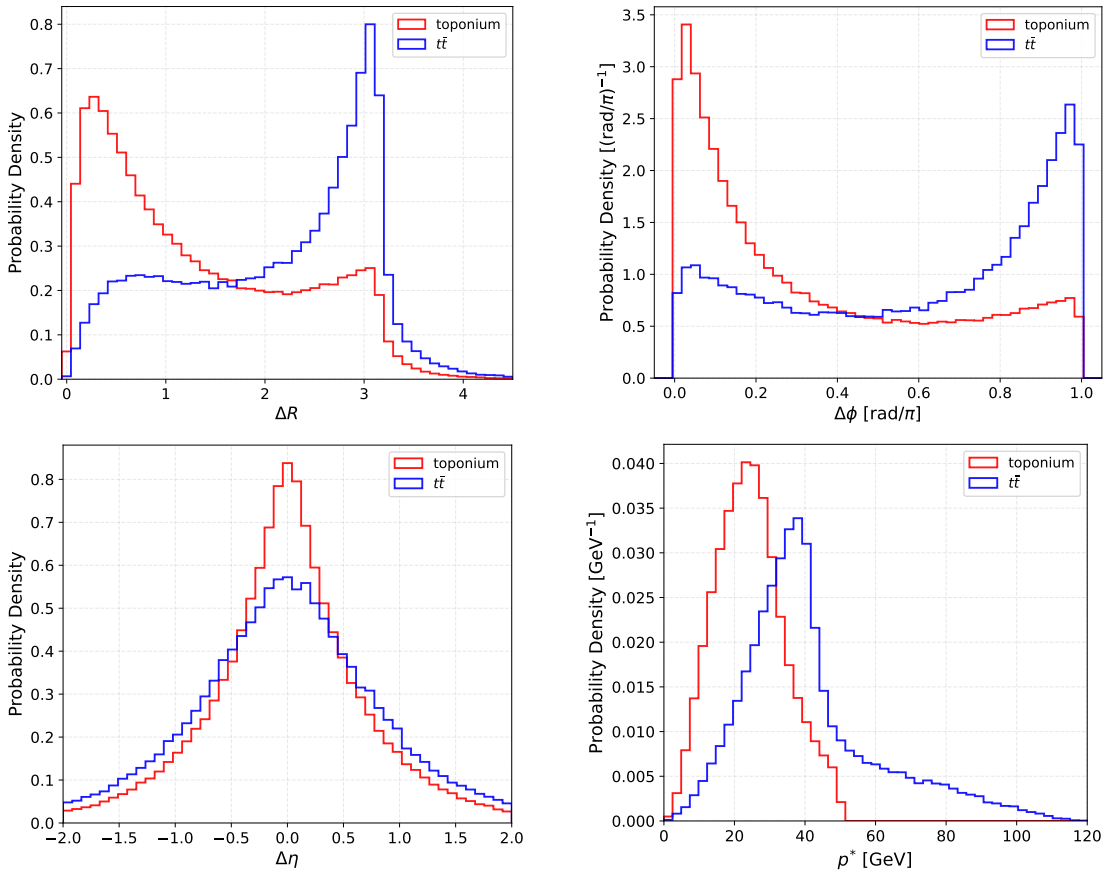

Figure 4.4.2: Probability density distributions of the variables ΔR, $\Delta\phi$, $\Delta\eta$ and p^* for conventional $t\bar{t}$ events without toponium effects and simulated toponium-only events, for $m_{t\bar{t}} < 355$ GeV.

toponium events, which tend to have the top quarks closer together. By contrast, in the continuum case the top quarks tend to be produced more separately. The combined information of ΔR and $\Delta\phi$, which is embedded in $\Delta\eta$, does not improve the separation compared to the individual variables. The variable p^* is also very sensitive to the different production regimes, as will be proved later in the analysis.

For toponium, it peaks at ≈ 20 GeV, in agreement with the simulation results of [13]. It must be noted that the sharp cutoff in p^* distribution is a Monte Carlo artifact due to modeling limitations. In particular, the simulated spectrum is reliable only in the phase-space region where the top quarks are non-relativistic, unless a more accurate matching prescription is implemented [13, 81]. For this reason, events with $p^* \gtrsim 35$ GeV will be considered unreliable in the analysis.

The second part of the kinematic study involves the so-called b_i observables (with $i = 1, 2, 3, 4$), which go beyond the standard kinematic quantities treated above by providing normalized event-by-event measures of momentum correlations between the top and antitop quarks. They are dimensionless scalar observables built from the reconstructed three-momenta $\vec{p}_t$ and $\vec{p}_{\bar{t}}$ of the top and antitop quarks in the laboratory frame, the beam direction $\hat{p}$ and the normal to the production plane $\hat{n} \equiv \hat{z}$. They are defined so as to have definite transformation properties under discrete symmetries, such as CP, and have been shown to significantly enhance sensitivity to new physics in the $t\bar{t}$ channel, including heavy neutral Higgs bosons (X) in $pp \to t\bar{t}X$, where they enable discrimination between scalar and pseudoscalar contributions [82, 83]. For this reason, they are well-suited to probe $t\bar{t}$ bound state signals, whose formation is expected to modify spin-dependent momentum correlations in a characteristic way, making them particularly interesting for to this study.

Specifically, they are constructed by projecting the top and antitop three-momenta onto the transverse plane relative to the beam (b_1), the production plane (b_2), and the $\hat{x}$ (b_3) and $\hat{z}$ (b_4) directions, and normalising by the appropriate momentum magnitudes, which ensures $b_i \in [-1, 1]$. Their explicit expressions are:

$$\begin{aligned} b_1 &= \frac{(\vec{p}_t \times \hat{p}) \cdot (\vec{p}_{\bar{t}} \times \hat{p})}{p_t^T \, p_{\bar{t}}^T} \quad & b_2 &= \frac{(\vec{p}_t \times \hat{n}) \cdot (\vec{p}_{\bar{t}} \times \hat{n})}{|\vec{p}_t| \, |\vec{p}_{\bar{t}}|} \\ b_3 &= \frac{p_t^x \, p_{\bar{t}}^x}{p_t^T \, p_{\bar{t}}^T} & b_4 &= \frac{p_t^z \, p_{\bar{t}}^z}{|\vec{p}_t| \, |\vec{p}_{\bar{t}}|} \end{aligned} \tag{4.4.1}$$

As a result, they probe the correlations between the top and antitop quark momenta in different geometric configurations. The observable b_1 is directly sensitive to azimuthal correlations arising from the production dynamics; b_2, instead, isolates momentum components lying within the production plane, probing correlations associated with the scattering geometry. Finally, b_3 and b_4 directly correlate the x- and z-components of the three-momenta, providing complementary sensitivity along the transverse and longitudinal directions.

The resulting distributions are shown in Figure 4.4.3. For all four observables, the probability density is enhanced in some specific regions of phase space, namely near unity for b_1 and b_4 and close to zero for b_2 and b_3. Most importantly, with the

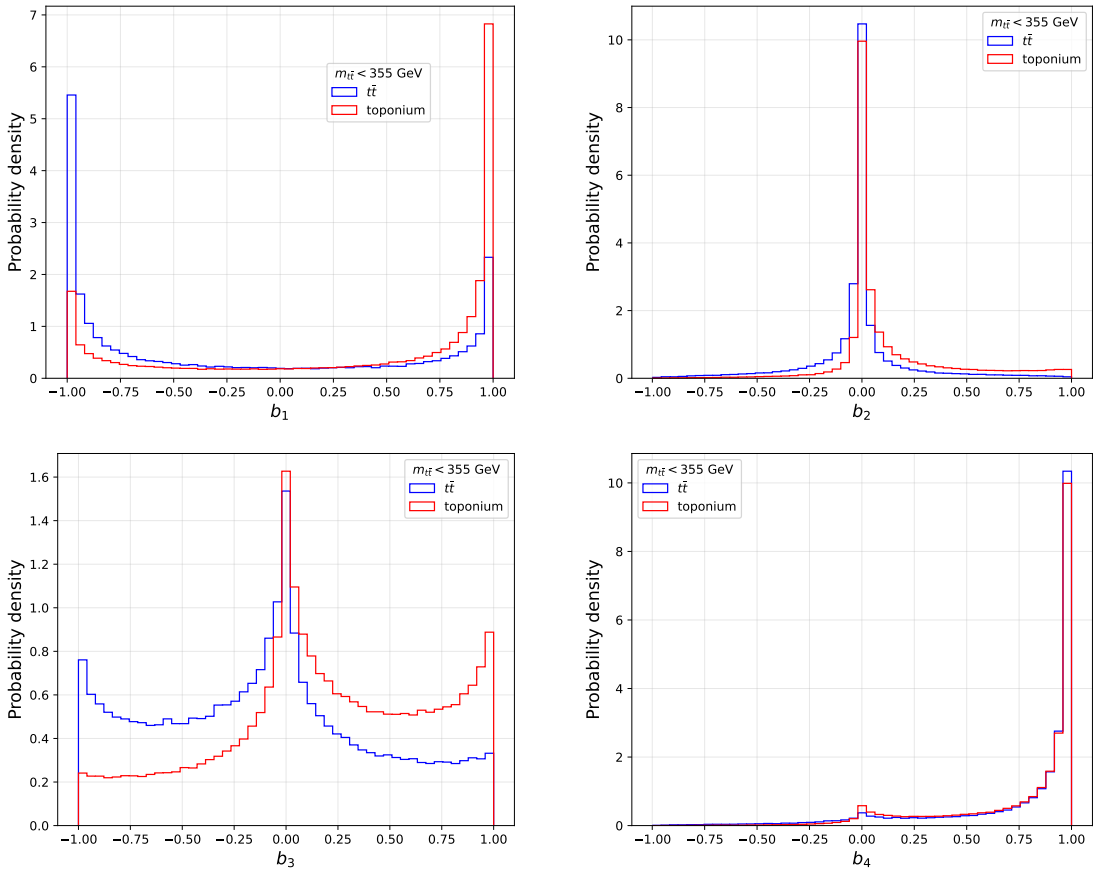

Figure 4.4.3: Probability density distributions of the variables b_1, b_2, b_3, and b_4 for conventional $t\bar{t}$ events without toponium effects ($t\bar{t}$) and simulated toponium-only events, for $m_{t\bar{t}} < 355$ GeV.

exception of b_4, the distributions exhibit significant differences between the two samples, characterized by asymmetric shapes. This confirms that distinct correlations between the top and antitop momenta arise in the two production regimes, as previously observed using angular observables. A representative example is provided by b_2, which by construction is positive (negative) if the top and antitop are emitted in the same (opposite) hemiplane. Near production threshold, the limited available phase space causes the $t\bar{t}$ pair to be typically produced at rest, with b_2 reasonably peaking at zero. For momentum conservation, the top and antitop quarks are emitted back-to-back in the laboratory frame, which translates into a distribution asymmetric towards neagative b_2 values for the continuum $t\bar{t}$ sample. By contrast, b_2 tends towards positive values for toponium, suggesting a boost for this particle that brings the top and antitop quarks closer to each other in the

same hemiplane. This tiny effect corresponds to the boost of $|\vec{p}_{t\bar{t}}|$ for toponium in Figure 4.4.1.

The excesses of events in specific regions of the b_i distributions could provide additional sensitivity to toponium contributions, provided that detector resolution effects do not significantly distort their shapes. A more realistic analysis will be presented in Section 4.4.4, where normalisation is applied to both datasets and the weighted combination of $t\bar{t}$ and toponium events is shown in the plots.

4.4.2 Quantum Information-inspired observables

Quantum Information (QI) observables are intrinsically statistical quantities, defined at the ensemble level rather than on an event-by-event basis, in contrast to standard kinematic variables. In this section, *QI-inspired* observables are instead constructed from per-event spin correlation coefficients and their ability to discriminate between toponium and continuum $t\bar{t}$ production is studied. Although these quantities do not correspond to genuine QI measures, they can be evaluated on an event-by-event basis and used as inputs to a multivariate analysis for signal-background discrimination, as discussed in Section 4.5.

The per-event spin correlation coefficients are built from the original definition of Eq.2.5.22, without averaging on all the events:

$$C_{ij} = -9 \cos\theta_i^a \cos\theta_j^b \tag{4.4.2}$$

where i, j are taken from the helicity basis $\{\hat{k}, \hat{r}, \hat{n}\}$ and a, b refer to the decay products of the top and antitop quarks, respectively. The factor 9, coming from the integration over the phase space in the statistical measure of C_{ij}, is kept for better visualisation. The factor -1 comes as usual from the product of the spin analyzing powers of the two leptons, $\alpha_a \alpha_b = -1$. The distributions for the per-event diagonal coefficients are displayed in Figure 4.4.4. As can be observed from the plots, all observables peak at zero, while differences between the continuum $t\bar{t}$ and toponium samples emerge only in the asymmetric tails of the distributions. For toponium, the higher event density for negative coefficients values suggests that the top quarks are preferentially emitted in the same hemiplane, as already discussed in Section 4.4.1. Such asymmetries are not observed for the off-diagonal coefficients, shown in Fig. 4.4.5. This behavior is consistent with the statistical analysis presented in Section 4.2, where the diagonal coefficients were found to exhibit the largest differences between the two samples.

Starting from the spin correlation coefficients, additional per-event quantum-inspired observables can be constructed. These include the differences between the

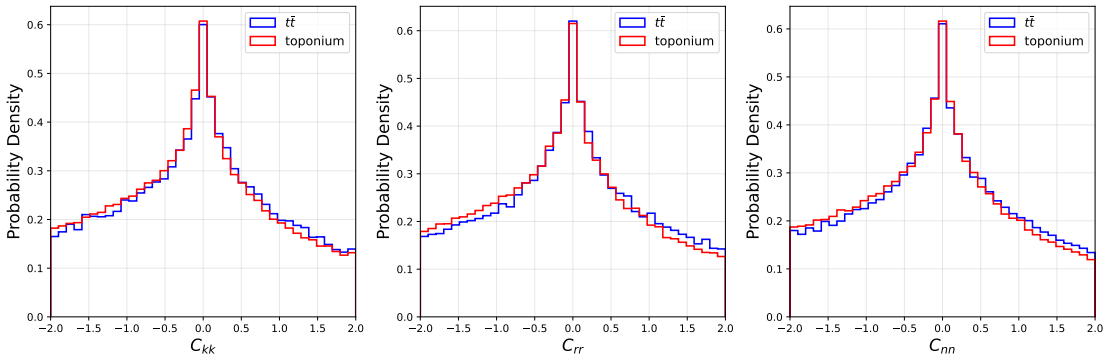

Figure 4.4.4: Probability density distributions of the per-event diagonal correlation coefficients C_{kk}, C_{rr}, C_{nn} for conventional $t\bar{t}$ events without toponium effects ($t\bar{t}$) and simulated toponium-only events, for $m_{t\bar{t}} < 355$ GeV.

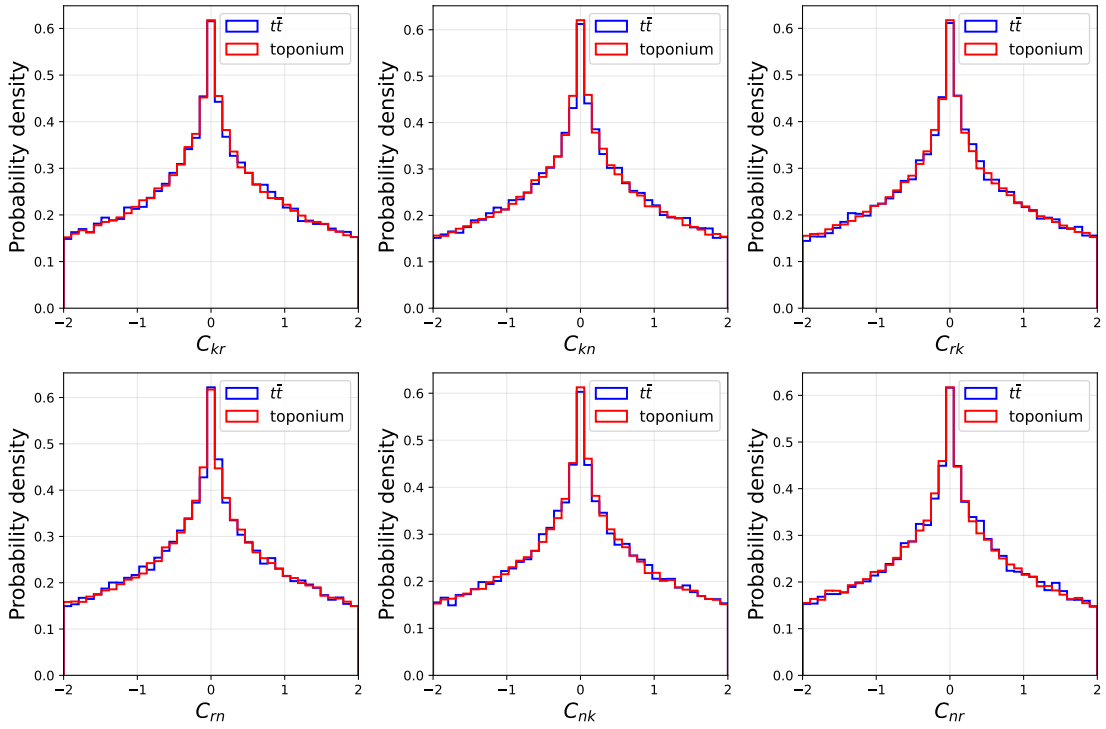

Figure 4.4.5: Probablity density distributions of the per-event off-diagonal correlation coefficients C_{ij}, with $i, j \in \{k, r, n\}$, $i \neq j$. Results are shown for conventional $t\bar{t}$ events without toponium effects ($t\bar{t}$) and simulated toponium-only events, for $m_{t\bar{t}} < 355$ GeV.

diagonal coefficients, to investigate whether combining these quantities enhances the asymmetries observed at the single-coefficient level, as well as observables derived from the standard entanglement and magic measures. The distributions

of the diagonal differences are shown in Figure 4.4.6. In this case, only the $C_{rr}-C_{nn}$ observable appears to provide a slight discriminating power.

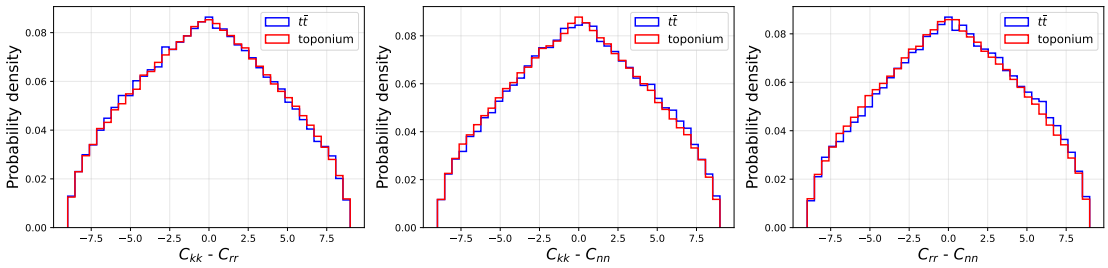

Figure 4.4.6: Probability density distributions of $C_{kk} - C_{rr}$, $C_{kk} - C_{nn}$ and $C_{rr} - C_{nn}$ for conventional $t\bar{t}$ events without toponium effects ($t\bar{t}$) and simulated toponium-only events, for $m_{t\bar{t}} < 355$ GeV.

Concerning the quantities related to entanglement, two variables are considered. The first, denoted as $D^{(1)\text{evt}}$, is constructed exactly as $D^{(1)}$ in Eq. 2.5.29, with the only difference that the correlation coefficients are evaluated per event. The second is a kinematic quantity related to $D^{(n)}$, $\cos\theta'$. It appears in Eq. 2.5.35, which expresses $D^{(n)}$ by averaging over the distribution of the decay products of the $t\bar{t}$ pairs. In this case, $\cos\theta'$ is not averaged but used as a per-event variable, so that the per-event analogue of $D^{(n)}$ would be:

$$D^{(n)\text{evt}} = -3\cos\theta' \tag{4.4.3}$$

where the factor 3 plays the same role as the factor 9 in Eq. 4.4.2. An alternative definition of $D^{(n)\text{evt}}$ could be given using the per-event spin spin correlation coefficients. Figure 4.4.7 shows the distributions of $D^{(1)\text{evt}}$ and $\cos\theta'$, which exhibit different slopes for the two samples. $D^{(n)\text{evt}}$ is expected to have a slope opposite to that of $D^{(1)\text{evt}}$, given the minus sign in Eq. 4.4.3.

Last, the per-event implementation of the quantum magic measure follows the same approach adopted for $D^{(1)\text{evt}}$. It is constructed indeed using the original Eq. 2.5.40, with the spin correlation coefficients defined in Eq. 4.4.2, from which the factor 9 is removed to improve the visualisation. The distribution of the M_2^{evt} observable is shown in Figure 4.4.8 in the left panel. As evident from the plot, this variable does not provide a significant separation between the two systems. By construction, it does not preserve the tail differences observed in the per-event distributions of the correlation coefficients, shown in Figure 4.4.4. In fact, the C_{ij} terms enter in the observable's computation through even powers, causing positive and negative contributions to compensate each other and washing out the tail asymmetries.

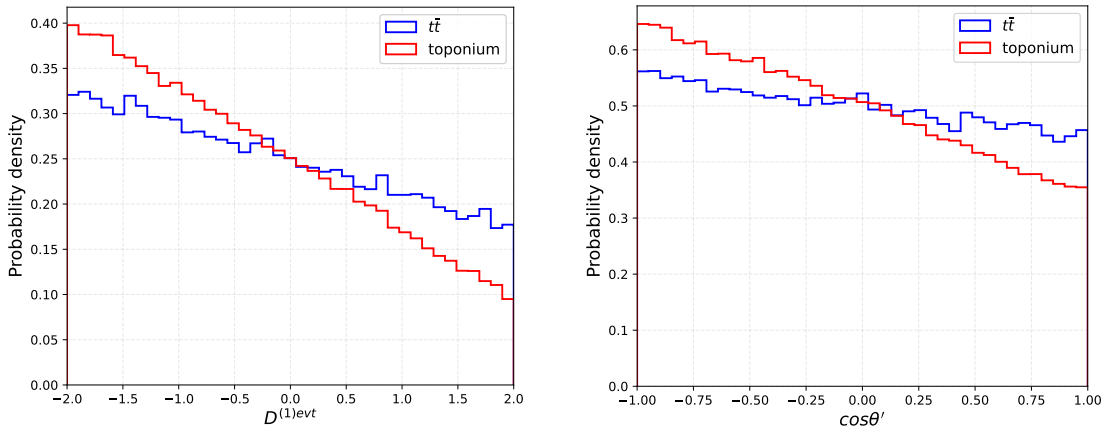

Figure 4.4.7: Probability density distributions of the variables $D^{(1)\text{evt}}$ and $\cos\theta'$ for conventional $t\bar{t}$ events without toponium effects ($t\bar{t}$) and simulated toponium-only events, for $m_{t\bar{t}} < 355$ GeV.

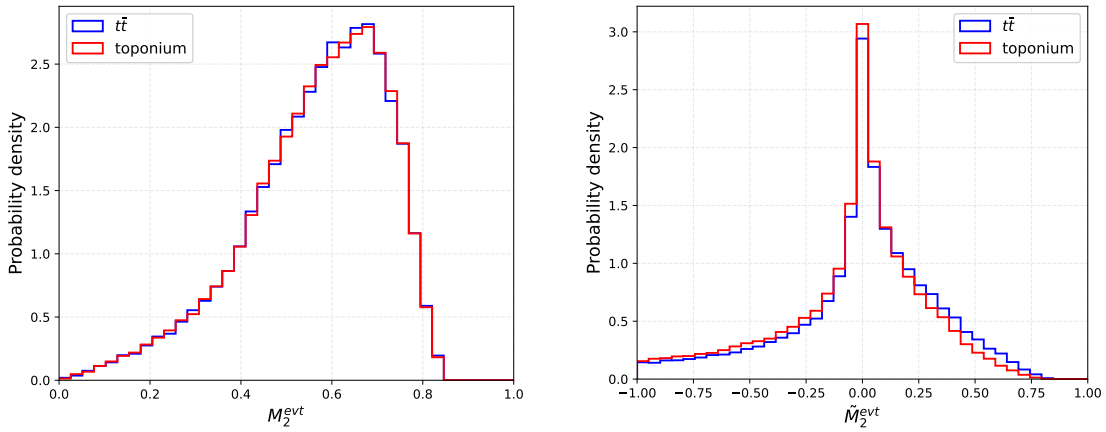

Figure 4.4.8: Probability density distributions of the variables M_2^{evt} and $\widetilde{M}_2^{\text{evt}}$ for conventional $t\bar{t}$ events without toponium effects ($t\bar{t}$) and simulated toponium-only events, for $m_{t\bar{t}} < 355$ GeV. $\widetilde{M}_2^{\text{evt}}$ shows an improved separation power compared to M_2^{evt}.

To recover sensitivity to these differences, a new magic-inspired observable $\widetilde{M}_2^{\text{evt}}$ is introduced by redefining the per-event magic variable in a way that preserves the sign of the spin correlation coefficients. Its expression is given by:

$$\widetilde{M}_2^{\text{evt}} = -\log_2 \left(\frac{1 + \sum_{i,j\in\{k,r,n\}} \text{sgn}\left(\cos\theta_i^a \cos\theta_j^b\right) \left(\cos\theta_i^a \cos\theta_j^b\right)^4}{1 + \sum_{i,j\in\{k,r,n\}} \text{sgn}\left(\cos\theta_i^a \cos\theta_j^b\right) \left(\cos\theta_i^a \cos\theta_j^b\right)^2} \right) \tag{4.4.4}$$

The corresponding distribution is shown in Figure 4.4.8 in the right panel: the asymmetry information is indeed preserved, yielding a slightly better sensitivity

compared to M_2^{evt}.

For completeness, this new observable has been evaluated also on the ensemble, as done for magic and entanglement in Section 4.3. This redefined quantity, $\widetilde{M_2}$, is obtained by statistically averaging over the events, yielding the expression:

$$\widetilde{M_2} = -\log_2 \left(\frac{1 + \sum_{i,j \in \{k,r,n\}} \text{sgn}\left(\langle \cos\theta_i^a \cos\theta_j^b \rangle\right) \left(\langle \cos\theta_i^a \cos\theta_j^b \rangle\right)^4}{1 + \sum_{i,j \in \{k,r,n\}} \text{sgn}\left(\langle \cos\theta_i^a \cos\theta_j^b \rangle\right) \left(\langle \cos\theta_i^a \cos\theta_j^b \rangle\right)^2} \right). \quad (4.4.5)$$

The measured values of M_2 and $\widetilde{M_2}$ for conventional $t\bar{t}$, toponium and their weighted combination are shown in Table 11. At the ensemble level, the new variable $\widetilde{M_2}$ appears to be particularly powerful in discriminating between the different contributions.

Table 11: Measured values of M_2 and $\widetilde{M_2}$ for dileptonic $t\bar{t}$ production near threshold ($m_{t\bar{t}} < 355$ GeV), shown for the standard $t\bar{t}$ sample, the toponium sample and their weighted combination.

	$t\bar{t}$	Toponium	Combined
M_2	0.5481 ± 0.0051	0.1525 ± 0.0069	0.3537 ± 0.0047
$\widetilde{M_2}$	-1.4524 ± 0.0658	0.3716 ± 0.0193	1.4895 ± 0.0533

4.4.3 Performance and correlations

In this section, the performance of some of the single variables studied in the previous part (Section 4.4) is presented, together with their correlations. The performance of each variable is evaluated using *Receiver Operating Characteristic* (ROC) curves, which provide a standard method to illustrate the discriminating power of a *classifier*, in this case is a single variable. These curves show the background rejection $1 - \varepsilon_B$, where ε_B is the background efficiency, as a function of the signal efficiency ε_S. Each point of the curve corresponds to a specific selection cut applied to the distribution of the variable for signal and background, yielding the respective efficiencies: by varying this threshold, the final ROC curve is obtained. This method allows the classifiers to be ranked according to the *Area Under the Curve* (AUC): the larger the AUC, the better the performance. Specifically, an AUC of 0.5 indicates a classifier with no predictive power, equivalent to random guessing, while an AUC of 1 represents perfect separation. The AUC serves as a key *Figure of Merit* (FoM), providing a quantitative measure of the variable's performance. More generally, these metrics allow for the evaluation of the discriminant according to various criteria.

The analysis is performed without applying physical normalization, which is not required for ROC curve evaluation, and without imposing final-state selection cuts. In this context, the background is represented by the $t\bar{t}$ events, while toponium-only events consitute the signal contribution. Figure 4.4.9 compares the ROC curves for some standard kinematic variables $(\Delta R, \Delta\phi, p^*)$, for the b_i observables (b_1, b_2, b_3) and for QI-inspired variables $(D^{(1)\text{evt}}, \widetilde{M}_2^{\text{evt}}, \cos\theta')$. The variables b_4 and M_2^{evt} have also been studied but, as expected from their distributions in Figures 4.4.3 and 4.4.8, are not found to be useful discriminants. In particular, both variables yield an AUC only slightly above 0.5, indicating performance close to that of a random classifier. They are therefore excluded from the analysis.

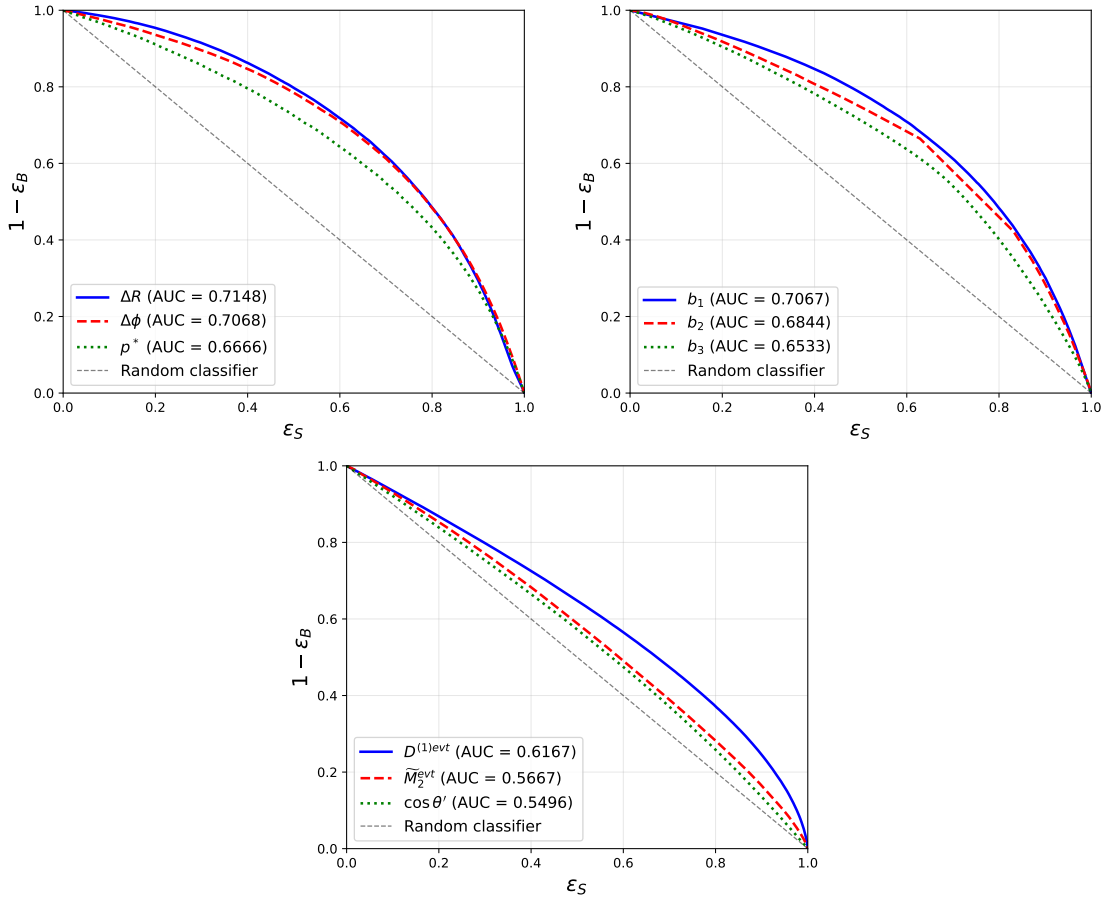

Figure 4.4.9: ROC curves for the kinematic variables $\Delta R, \Delta\phi, p^*$ (top left), the b_i observables (top right) and the QI-inspired variables $D^{(1)\text{evt}}, \widetilde{M}_2^{\text{evt}}, \cos\theta'$ (bottom). All variables refer to Section 4.4 and the study of p^* restricts to the region with $p* < 35$ GeV. The dashed line corresponds to a random guessing (AUC = 0.5).

As evident in the plots, the kinematic variables ΔR and $\Delta\phi$ describing the angular separation between the two final-state leptons in the transverse plane, together with b_1, exhibit the strongest discriminating power, reflecting the particular angular correlations induced by bound-state formation. Among these, the ROC curves of b_1 an $\Delta\phi$ are basically identical, reflecting their very high correlation as observed in the correlation matrix in Figure 4.4.10. The kinematic variables b_1, b_3 and p^* also yield good separation, confirming that kinematic variables constructed only from reconstructed top-quark momenta retain sensitivity to the production mechanism. It is relevant to note that the study of p^* is restricted to the region $p^* < 35$ GeV, where the variable is reliably modeled; in this region, p^* is found to be the most powerful classifier among those considered. In contrast, the QI-inspired variables display overall lower discriminating performance when considered individually, with $D^{(1)\text{evt}}$ emerging as the most useful observable for distinguishing the toponium signal from the $t\bar{t}$ background.

In Figure 4.4.10, the correlations among these variables are shown. It can be observed that b_1, b_2 and b_3 are highly correlated with each other, meanwhile showing relevant anti-correlations also with the angular observables ΔR and $\Delta\phi$. The last two are, in turn, very correlated with each other, explained by the fact that they probe closely related features of the dileptonic angular configuration. By contrast, the QI-inspired observables $D^{(1)\text{evt}}$, $\widetilde{M}_2^{\text{evt}}$ and $\cos\theta'$ exhibit weak correlations with all the above kinematic variables and moderate correlations among themselves. This suggests that these observables encode information that is not fully captured by the purely kinematic variables, motivating the use of a multivariate approach (Section 4.5) to exploit the different correlations and combine any complementary information.

For completeness, the correlation plots among the considered observables are shown in Appendix C.

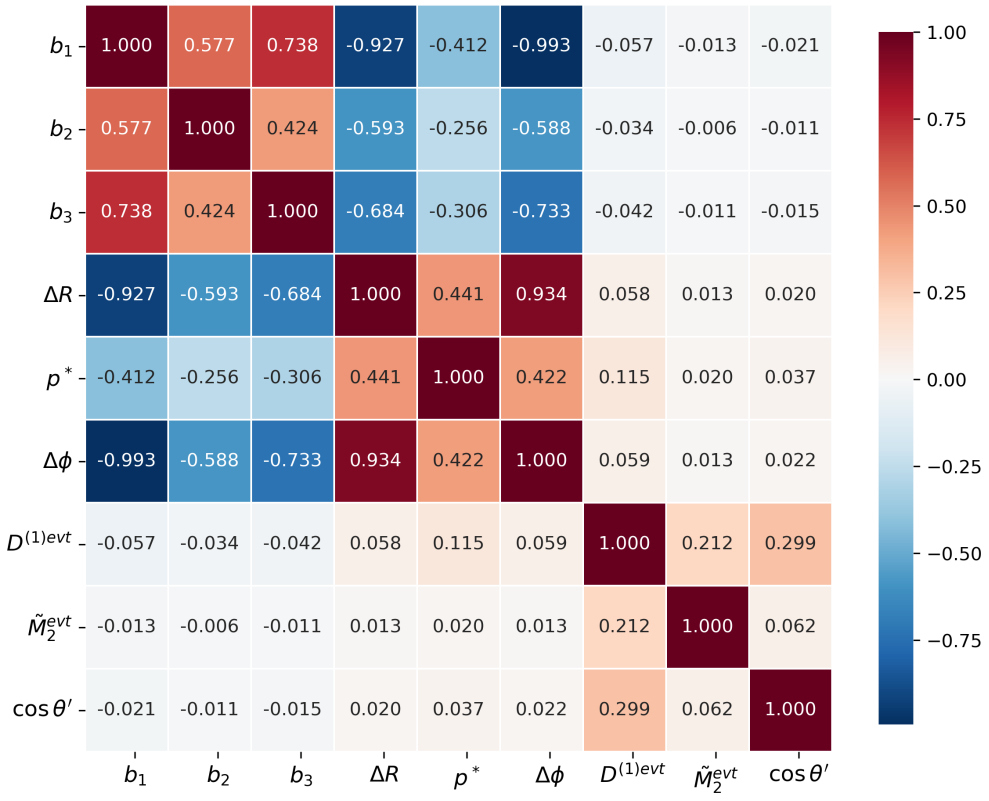

Figure 4.4.10: Correlation matrix of all variables, with $m_{t\bar{t}} < 355$ GeV and $p^* < 35$ GeV. It considers all input variables that will be employed in the BDT analysis in Section 4.5.

4.4.4 Impact of normalization and final-state analysis cuts

This section presents a more realistic analysis, obtained by applying the physical normalization and final-state selection cuts described in Section 4.1.1 to the distributions of the most sensitive variables. The focus is on evaluating the impact of these procedures on both the observables and their performance.

Figure 4.4.11 shows the physically normalized distributions of the b_1, b_2, b_3, and b_4 observables for standard $t\bar{t}$ production, for $t\bar{t}$ events including toponium effects and for their weighted combination based on the respective cross sections. Figure 4.4.12 displays the distributions of ΔR, $\Delta\phi$, $p^\star$, $D^{(1)\mathrm{evt}}$, $\cos\theta'$ and $\widetilde{M}_2^{\mathrm{evt}}$.

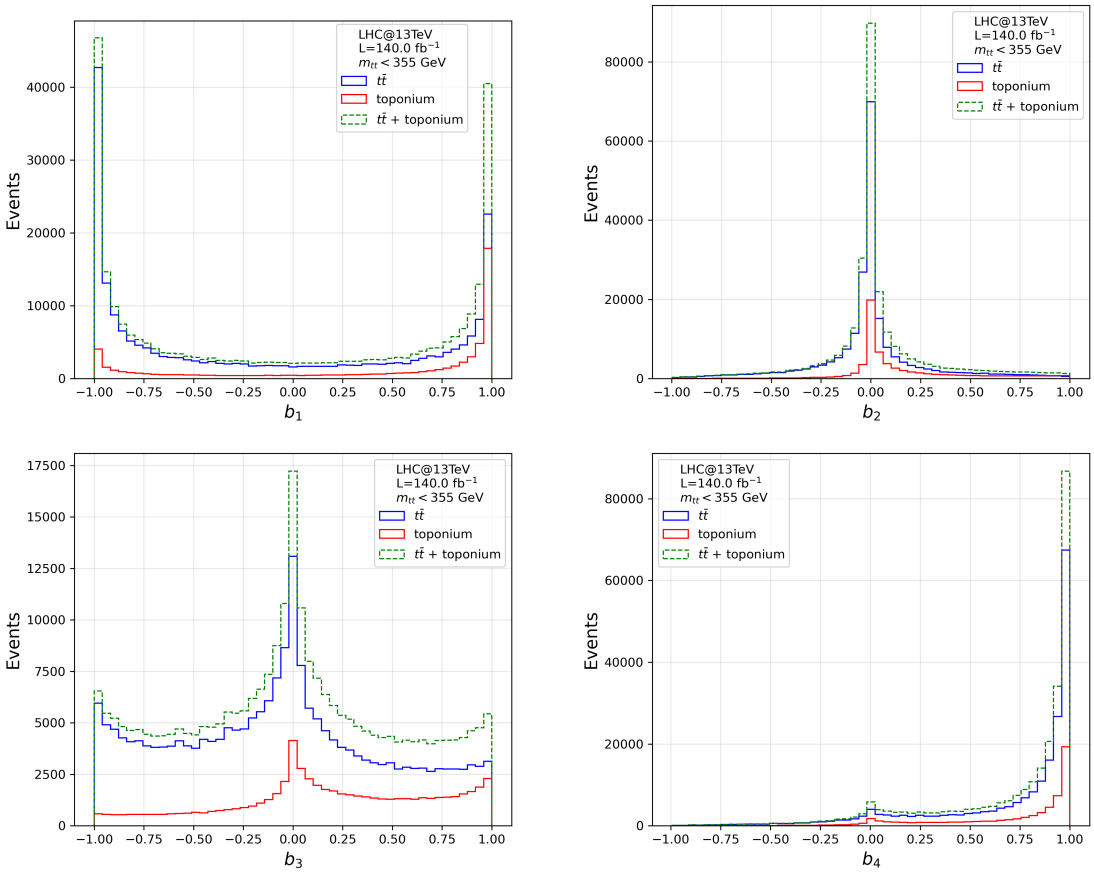

Figure 4.4.11: Distributions of the variables b_1, b_2, b_3, and b_4 for conventional $t\bar{t}$ events without toponium effects ($t\bar{t}$), simulated toponium-only events and $t\bar{t}$ events including toponium effects ($t\bar{t}$ + toponium), after normalization (see Section 4.1.1). Selection cuts are applied: $m_{t\bar{t}} < 355$ GeV for all events; $p_T > 25$ GeV for at least one lepton and $|\eta| < 2.5$ for both leptons; and $p_T > 25$ GeV and $|\eta| < 2.5$ for both b quarks.

Compared to the results of Section 4.4, the normalization procedure results in a simple rescaling of the distributions, without distorting their shapes or altering their physical interpretation. The weighted combination of $t\bar{t}$ and toponium events highlights the excesses that could emerge in experimental data and serve as potential signatures of toponium formation. However, as previously shown in the $m_{t\bar{t}}$ distribution in Figure 4.1.1, the toponium signal appears as a subtle enhancement near threshold over the large continuum $t\bar{t}$ background, emphasizing the experimental challenge of its observation. For these plots to be representative of a more realistic analysis, selection cuts on the dileptonic final state are also applied, namely $p_T > 25$ GeV for at least one lepton and $|\eta| < 2.5$ for both leptons, and $p_T > 25$ GeV and $|\eta| < 2.5$ for both b quarks.

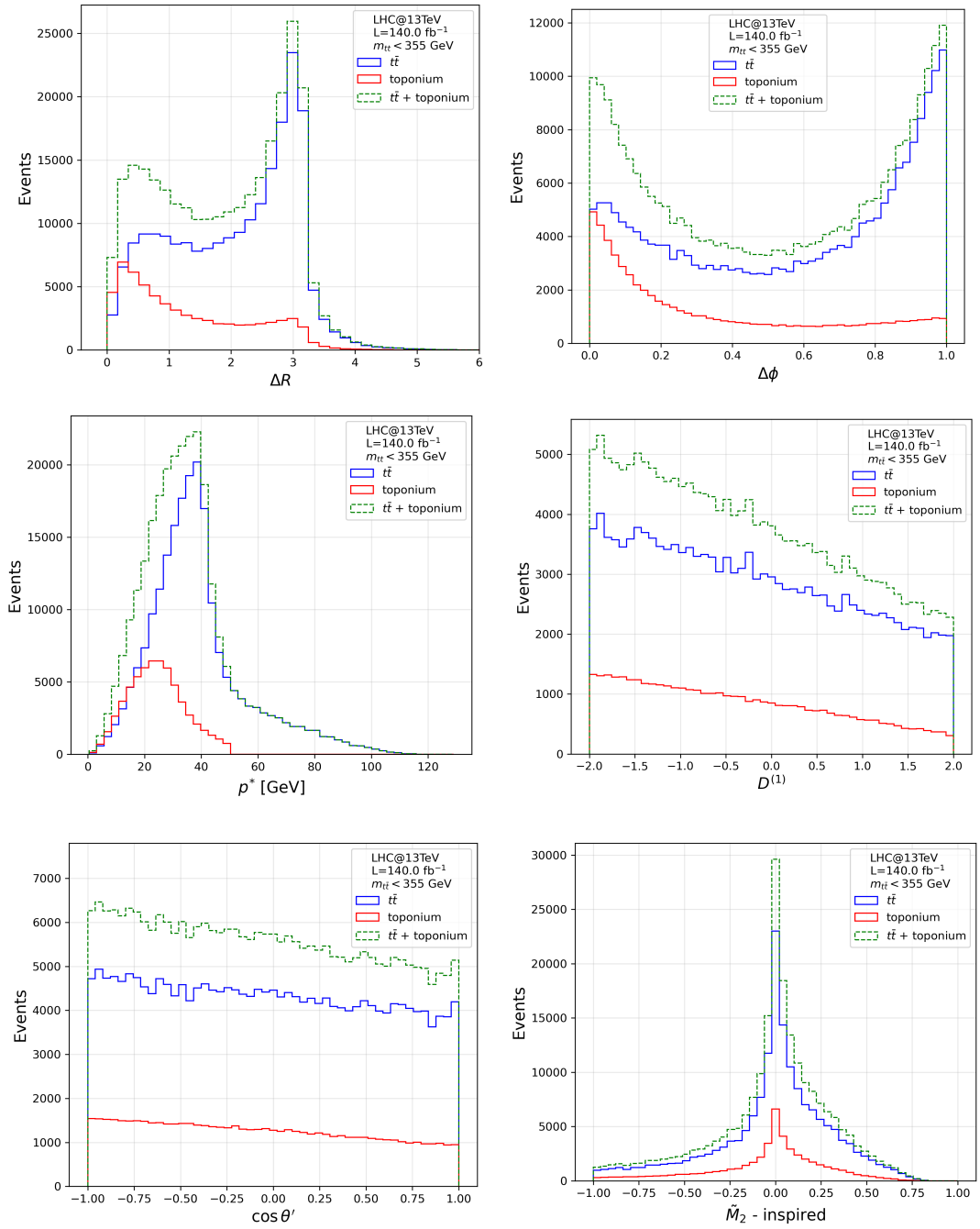

Figure 4.4.12: Normalized distributions for conventional $t\bar{t}$ events without toponium effects, simulated toponium-only events and their weighted combination ($t\bar{t}$+toponium), for ΔR, $\Delta\phi$, p^*, $D^{(1)\text{evt}}$, $\cos\theta'$ and $\widetilde{M}_2^{\text{evt}}$. Selection cuts on the final states are applied, specifically the selection (a) of Table 8.

The impact of different cut scenarios (Section 4.1.1) on the distributions is illustrated for b_3 (for toponium) and $\Delta\phi$ (for $t\bar{t}$) in Figure 4.4.13, showing only a reduction in event statistics without significant change in shape.

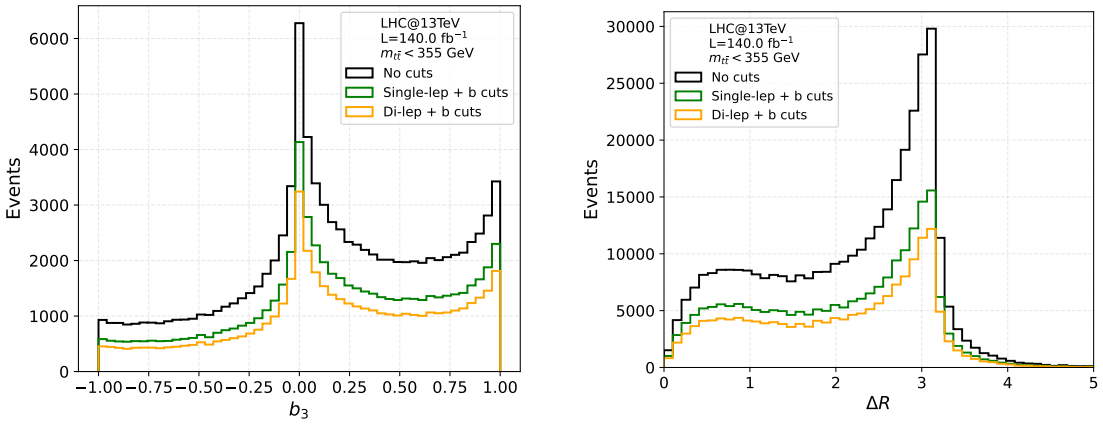

Figure 4.4.13: Distributions of the variable b_3 (for toponium-only events) and ΔR (for conventional $t\bar{t}$ events), after physical normalization (see Section 4.1.1) and for $m_{t\bar{t}} < 355$ GeV. Three cut scenarios are displayed: no cuts applied on leptons and b-quarks (*No cuts*); $p_T > 25$ GeV for at least one lepton, $|\eta| < 2.5$ for both leptons, $p_T > 25$ GeV and $|\eta| < 2.5$ for both b quarks (*Single-lep + b cuts*); $p_T > 20$ GeV and $|\eta| < 2.5$ for both leptons, $p_T > 25$ GeV and $|\eta| < 2.5$ for both b quarks (*Di-lep + b cuts*).

Finally, the effect of final-state selection requirements on the performance of the variables in discriminating toponium signal from $t\bar{t}$ background is shown for b_3 in Figure 4.4.14. As can be observed in the plot, the AUC for the b_3 observable after the cuts is not significantly reduced. Moreover, the single-lepton and dilepton trigger requirements do not have significant impacts on the performance.

To conclude this study, the application of final-state analysis selections, also combined with physical normalization, does not distort the distributions of the observables, but only rescales them and reduces the available statistics, with only a slight impact on performance. Moreover, the selection based on the dilepton trigger leads to only a small reduction in statistics compared to the single-lepton trigger, which is therefore adopted for the remaining part of the analysis.

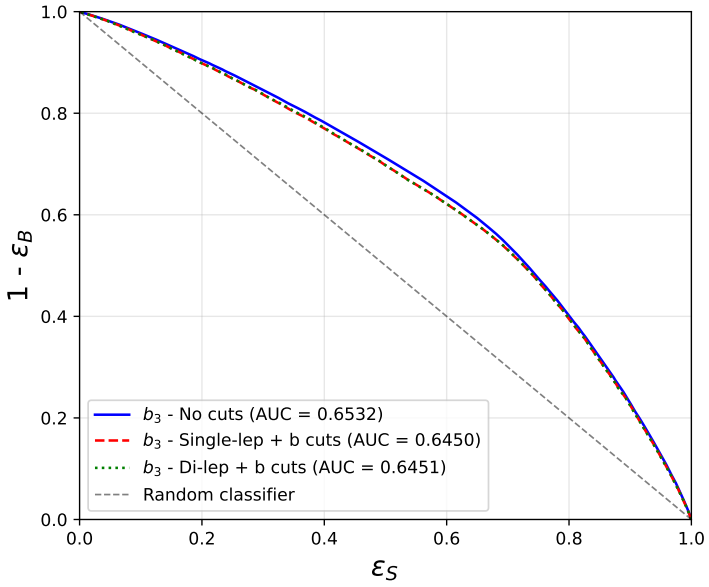

Figure 4.4.14: ROC curves for the b_3 observable in the three cut scenarios: no cuts on the final states (*No cuts*), selection (a) (*Single-lep + b cuts*) and selection (b) (*Di-lep + b cuts*) of Table 8.

4.5 BDT implementation

Section 4.4 investigated the sensitivity of single variables to the presence of toponium in $t\bar{t}$ events. In this section, these variables are combined within a multivariate analysis (MVA) based on Boosted Decision Trees (BDTs), with the aim of further enhancing the discrimination between the toponium signal and the dominant $t\bar{t}$ background. The BDT method is first introduced, followed by a description of the two-BDT approach used in the analysis. Different BDT classifiers are constructed using various configurations of input variables. Finally, the performance of each classifier is evaluated using multiple metrics and after applying final-state selection cuts.

4.5.1 Multivariate Analysis

MVA refers to a class of statistical techniques employed to analyse datasets by combining multiple variables and is widely used in high energy physics to enhance the separation between rare signal processes and large background contributions. These methods rely on a *supervised training* procedure, in which an algorithm is exposed to simulated samples with known signal and background labels (*training sample*) and learns to distinguish between the two classes. The goal is to construct a *classifier* that combines several discriminating variables into a single function,

which assigns each event a score corresponding to its probability of belonging to the signal or background class. As the selection on one variable depends simultaneously on the others, the classifier is in general non-linear. Figure 4.5.1 illustrates the difference between traditional rectangular or linear cuts and non-linear cuts achievable with MVA techniques, like Boosted Decision Trees (BDTs) and Neural Networks (NNs).

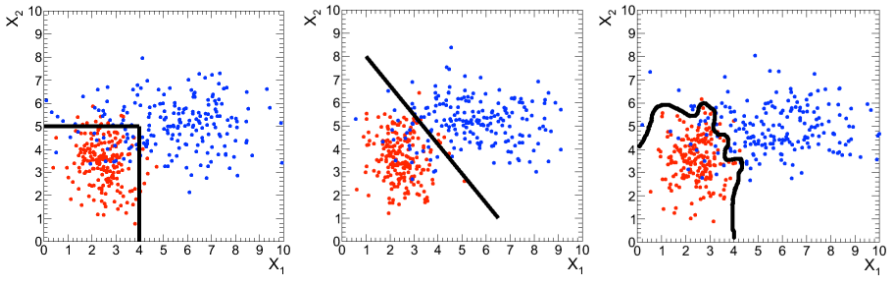

Figure 4.5.1: Different decision boundaries for signal (red) and background (blue) event classification. From the left: rectangular, linear (*Fisher discriminant*) and non-linear (BDT, NN) cuts.

4.5.2 Boosted Decision Trees (BDTs)

Among MVA techniques, the BDT method is the one adopted for this analysis. A *Decision Tree* (DT) is a machine learning algorithm with a binary tree structure that classifies events through a series of binary decisions on input variables. The training process starts from the *root node*, where the full dataset is split into two subsets according to a threshold condition on a selected discriminating variable. This procedure is applied recursively: at each node, the algorithm selects a variable x_i and the corresponding cut $x_i > c$ that maximizes a separation criterion between signal and background events. The same variable may be used at several nodes, while others might not be used at all. Node splitting continues until some stopping condition is reached, such as a maximum tree depth or a minimum number of events per node specified in the configuration. The ending decisions (*leaf nodes*) label the outputs according to the two classes under consideration, for example signal (S) and background (B), depending on the majority of events that end up in the respective nodes. A schematic view of a decision tree is shown in Figure 4.5.2.

However, single trees are highly unstable (*weak*), as small statistical fluctuations in training data could lead to very different trees. Moreover, they are prone to overfitting. To improve stablity and performance, a *boosting* algorithm is employed. *Boosted Decision Trees* (BDTs) iteratively combine many weak decision

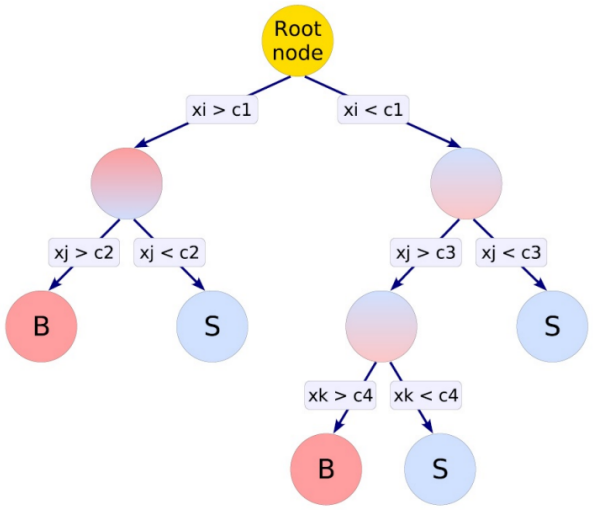

Figure 4.5.2: Scheme of a Decision Tree (DT).

trees into a single, robust classifier, characterized by a more stable response to fluctuations in the training sample and an enhanced performance with respect to the single tree. The algorithm starts by training an initial tree and looking at where it fails; misclassified events are given more importance, in a way that depends on the boosting algorithm used; a new tree is then trained on the reweighted events to fix the classification errors of the previous classifier. This procedure is repeated iteratively, each tree learning from the previous one and providing a small correction to the overall classifier. The final output of the BDT is a single discriminant function, which assigns each event a score reflecting its likelihood of belonging to the signal or background class. A schematic representation of the method is shown in Figure 4.5.3.

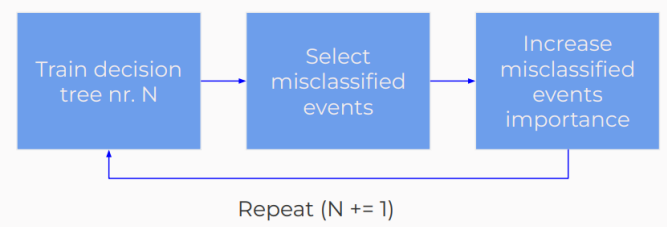

Figure 4.5.3: Generic scheme of a BDT algorithm.

The performance of a BDT classifier is evaluated by applying the trained model to an independent MC sample not used during training (*testing sample*) and comparing its output distribution to that obtained on the training sample. This comparison allows one to assess the presence of possible *overtraining*, which occurs

when the classifier learns statistical fluctuations specific to the training sample rather than general features of the underlying physical processes. If overtraining is observed, it can be mitigated by optimising the algorithm hyperparameters, such as the maximum tree depth, the number of trees, or the minimum number of events per node, or by increasing the sample statistics.

The BDT classifiers used in this work are implemented within the `XGBoost` framework [84] with the `gbtree` booster option. Further details on the method provided in Appendix B.

4.5.3 BDT strategy

This section presents the BDT strategy adopted in the analysis to enhance the separation between the toponium signal and the $t\bar{t}$ background. Several BDT configurations are investigated, differing in the choice of input variables:

- the full set of observables whose performance has been studied in Section 4.4.3, namely the kinematic variables ΔR, $\Delta\phi$, p^*, and b_1, b_2, b_3, together with the QI-related observables $D^{(1)\text{evt}}$, $\widetilde{M}_2^{\text{evt}}$, and $\cos\theta'$ (*All variables*);
- one excluding the quantum-information-inspired variables (*No QI variables*);
- one excluding p^* (*No* p^*);
- one restricted to the variables $D^{(1)\text{evt}}$ and $\cos\theta'$.

For configurations including p^*, a two-stage BDT training strategy is adopted, since the simulated toponium p^* spectrum is only reliable in phase-space regions with $p^* < 35$ GeV (see Section 4.4.1). In particular, events with $p^* < 35$ GeV are evaluated using a BDT trained with p^* included as an input variable, while events with $p^* \geq 35$ GeV are evaluated using a separate BDT trained without p^*, ensuring a consistent treatment of events across the full p^* spectrum. The final discriminant score is taken from the corresponding classifier according to the event's p^* value. In this procedure, all simulated events are randomly split into equal training and testing samples.

In the following, the two-BDT implementation for the *All variables* configuration is presented. The final-state selection (a) from Table 8 is applied to the $t\bar{t}$ and toponium samples, in order to show the results in a more realistic analysis scenario. Figure 4.5.4 shows the *feature importance* obtained from the two-BDT strategy, quantifying the relative contribution of each input variable (*feature*) to the model's classification performance and highlighting the observables that carry the most relevant information. For $p^* < 35$ GeV, where it is included as a BDT

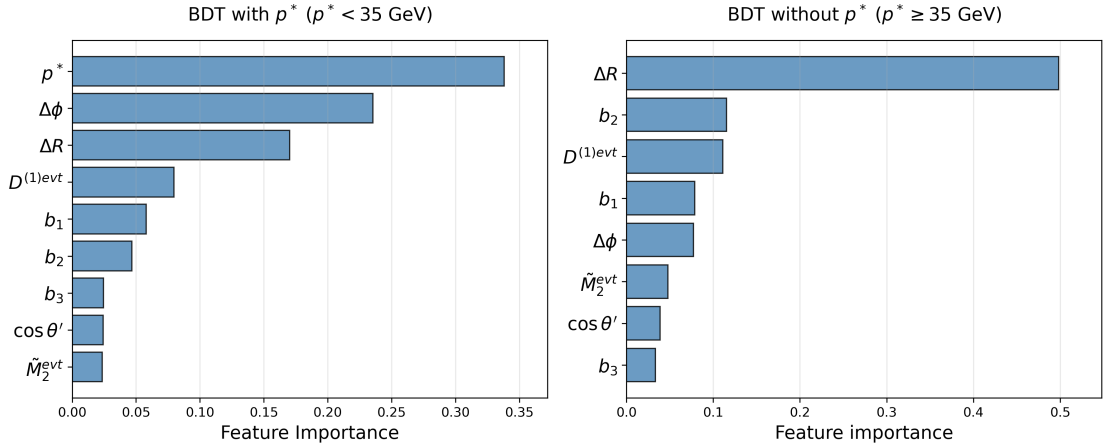

Figure 4.5.4: Feature importance obtained from the two BDT strategies: (left) BDT with p^* included among the input variables, for $p^* < 35$ GeV; (right) BDT with p^* excluded from input set of variables, for $p^* \geq 35$ GeV.

input, p^* emerges as the most important feature followed by ΔR and $\Delta\phi$, reflecting its sensitivity to near-threshold production. The observable $D_{\text{evt}}^{(1)}$ ranks above b_1, b_2 and b_3, showing that spin-sensitive variables provide a non-negligible contribution once correlations between variables are properly accounted for. In the complementary region, defined by $p^* \geq 35$ GeV and with a BDT trained on all input variables except for p^*, ΔR dominates the ranking, followed by b_2 and $D_{\text{evt}}^{(1)}$. Again, the major contribution from the QI-inspired comes from the $D_{\text{evt}}^{(1)}$ observable. While correlations, previously shown in Figure 4.4.10, provide useful insight into how the variables are related to each other, they alone do not indicate how much each variable actually contributes to separating signal and background. The BDT approach is particularly useful in this context, as it can exploit complex correlations and rank the variables according to their actual discriminating power when combined in an overall classifier.

Figure 4.5.5 shows the BDT score distributions for the toponium signal and the $t\bar{t}$ background, obtained with the BDT trained including $p^\star$ ($p^\star < 35$ GeV) and excluding it ($p^\star \geq 35$ GeV). The combined BDT score distribution is presented in Figure 4.5.6. In both figures, the distributions are shown separately for the training and testing samples: the agreement between training and testing validates the procedure and illustrates that no significant overtraining is observed. The final distributions for all input variables configurations, across various final-state selection scenarios, are shown in Appendix D.

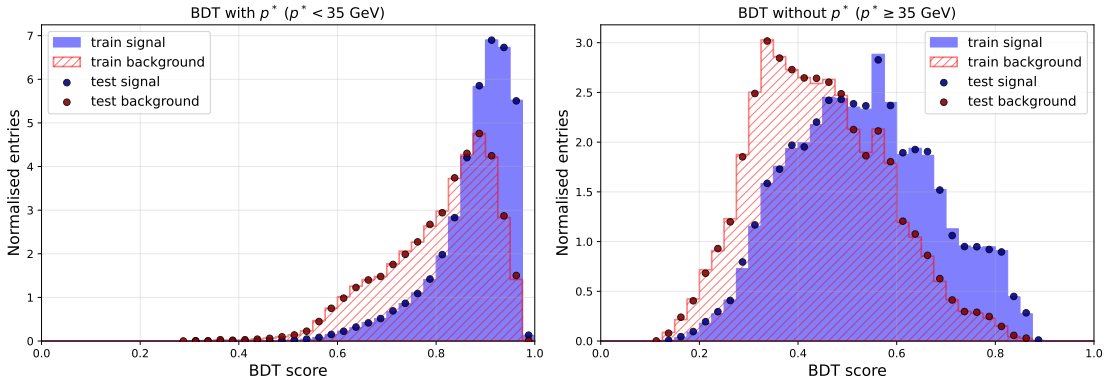

Figure 4.5.5: BDT score distributions for the toponium signal and $t\bar{t}$ background for the *All variables* configuration, shown for the BDT trained including p^* ($p^* < 35$ GeV) (left) and the BDT trained without p^* ($p^* \geq 35$ GeV) (right). The distributions are provided for both training and testing samples.

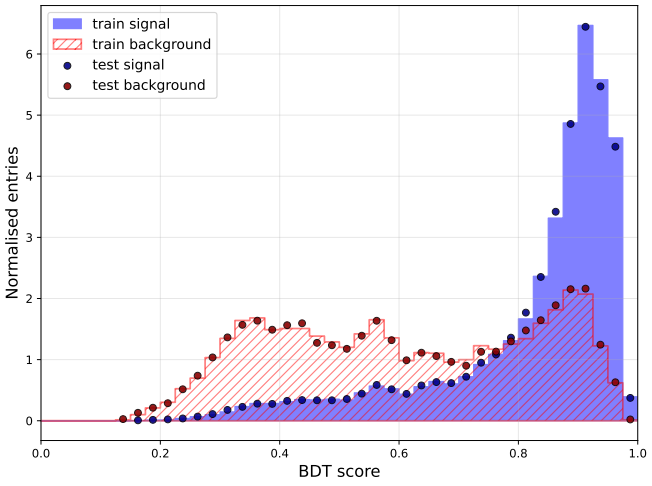

Figure 4.5.6: Final BDT score distribution for the *All variables* configuration, achieved with the two-stage strategy. The distribution for the toponium signal and the $t\bar{t}$ background is shown both for training and testing samples.

4.5.4 Performance

The performance of the BDT configurations defined in Section 4.5.3 is evaluated using two figures of merit: the AUC of the respective ROC curves and the signal significance at the optimal working point, as defined later.

The ROC curves for the different BDT configurations are shown in Figure 4.5.7, alongside those obtained from each input variable individually. Both results are

produced after applying selection (a) from Table 8 on the events. This first analysis allows to compare the performance of the classifiers visually and by means of their AUC values, which quantify the overall separation power between signal and background. The multivariate approach consistently outperforms any single

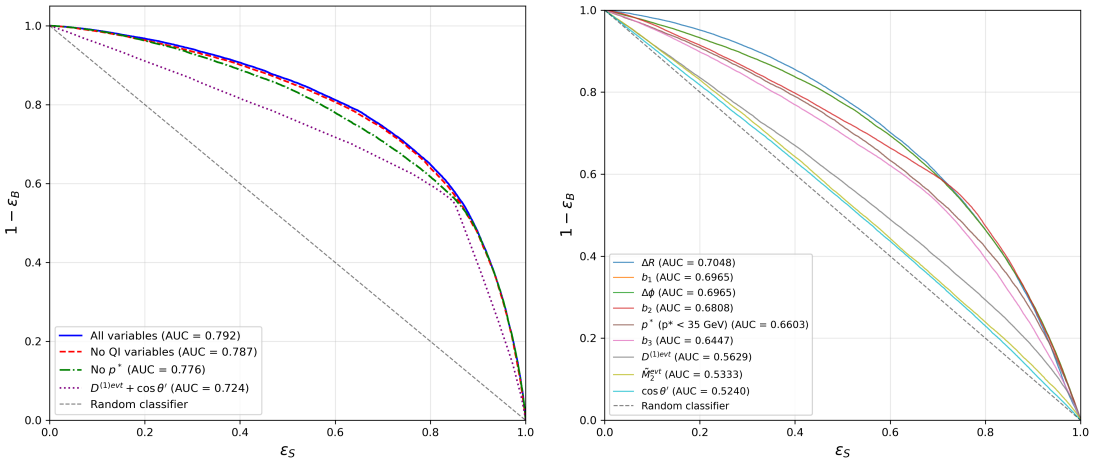

Figure 4.5.7: ROC curves for the different BDT configurations (left), alongside the ROC curves for the individual input variables (right). The corresponding AUC values are reported in the legend. Final-state selection (a) from Table 8 is applied.

observable, demonstrating the gain achieved by combining individual contributions within a unified classifier. Among the BDT configurations, the one trained on the full set of observables yields the best overall performance, while progressively reducing the input set leads to a gradual degradation in the discriminating power. Excluding the quantum-information-inspired variables has a limited impact on the ROC curve; however, their inclusion still yields a measurable gain, suggesting that their contribution is complementary to the remaining observables. By contrast, removing p^* results in a more visible loss, in agreement with its high ranking in the feature importance analysis (Figure 4.5.4) and its sensitivity to the near-threshold production dynamics. The configuration based solely on $D^{(1)\text{evt}}$ and $\cos\theta'$ shows the largest degradation, confirming that spin-correlation-related observables alone do not provide sufficient separation power. The ROC curve for this configuration exhibits a visible "kink" at high signal efficiencies ($\varepsilon_S \approx 0.85$), arising from the discrete structure of the tree-based classifier when operating on a restricted feature space (see Appendix D).

The effect of final-state selection cuts on AUC values for the different BDT configurations is illustrated in Table 12. As evident from the table, the application of these criteria on the events lead to a mild reduction of the overall performance.

The second part of the performance evaluation aims to quantify the achievable

	No cuts	(a)	(b)
(1)	0.8047	0.7923	0.7920
(2)	0.7989	0.7872	0.7869
(3)	0.7892	0.7760	0.7760
(4)	0.7409	0.7239	0.7229

Table 12: Effect of final-state selection cuts from Table 8 on AUC values associated with the BDT configuration studied: (1)*All variables*, (2) *No QI variables*, (3) *No* p^* and (4) $D^{(1)\text{evt}}$ and $\cos\theta'$.

statistical sensitivity in a more realistic analysis scenario. To this end, figures of merit that translate the classifier output into experimentally meaningful quantities are introduced. In particular, the expected *significance* is used to quantify the statistical strength of the toponium signal relative to the $t\bar{t}$ background. This metric measures the number of standard deviations by which the signal exceeds the background fluctuation, thus providing a measure of the potential for discovery or the achievable precision of a measurement.

For each BDT configuration, the significance estimators are evaluated as a function of the output score threshold by scanning its full range. At each step of the scan, the expected signal and background yields are computed as:

$$S = \sigma_{\text{toponium}} \cdot L \cdot \text{BR} \cdot \varepsilon_S, \qquad B = \sigma_{t\bar{t}} \cdot L \cdot \text{BR} \cdot \varepsilon_B, \tag{4.5.1}$$

where ε_S and ε_B are the efficiencies at the chosen threshold (considering the events above it), while σ, L and BR denote the cross-sections, integrated luminosity and branching ratio, respectively, as defined in Section 4.1.1. The *optimal working point* is then defined as the specific threshold that maximizes the value of a given significance estimator. In particular, three significance estimators are employed as figures of merit:

$$\frac{S}{\sqrt{B}}, \qquad \frac{S}{\sqrt{S+B}}, \qquad \frac{S}{\sqrt{S+B+\sigma_S^2}}. \tag{4.5.2}$$

The first represents the statistical significance in the absence of systematic effects, the second accounts for statistical fluctuations in both signal and background, while the third further provides a more realistic scenario by incorporating a typical 20% relative systematic uncertainty on the signal normalization ($\sigma_S = 0.2S$). This value is taken from the existing measurements of toponium [16] and includes also the impact of the background normalization.

Table 13 summarizes the performance at the optimal working point for the different BDT configurations after the application of final-state selection criteria, using the significance above. These results confirm the trends already observed in the ROC curves, with the best overall performance achieved by combining kinematic and spin-sensitive observables within a global framework.

	ε_S	ε_B	$S/\sqrt{B}$	$S/\sqrt{S+B}$	$S/\sqrt{S+B+\sigma_S^2}$	BDT score cut
(1)	0.665	0.228	37.619	37.202	4.955	0.835
(2)	0.643	0.219	37.092	36.680	4.954	0.844
(3)	0.792	0.375	34.944	34.663	4.949	0.777
(4)	0.830	0.428	34.249	33.996	4.947	0.797

Table 13: Performance metrics at the optimal working point for various BDT configurations (Section 4.5.3) after selection (a) from Table 8: (1) *All variables*; (2) *No QI variables*; (3) *No* p^*; (4) a configuration using only $D^{(1)\text{evt}}$ and $\cos\theta'$. The signal uncertainty is assumed to be $\sigma_S = 0.2\,S$. The optimal BDT score cut for each configuration is also shown.

The comparison among configurations also allows one to assess the relative impact of kinematic and quantum-information-inspired observables on the classifier performance. From the significance values, it is possible to quantify the gain associated with each contribution. In particular, including p^* among the input variables increases the significances $S/\sqrt{B}$ and $S/\sqrt{S+B}$ by $7,1\%$ (and $9,3\%$ in the no-cuts scenario) with respect to the BDT trained without it. By contrast, the inclusion of QI-related variables leads to a milder, although still not negligible, improvement of $1,4\%$ (and $3,3\%$ in the no-cuts scenario) relative to BDT trained using kinematic-only variables. The third estimator, $S/\sqrt{S+B+\sigma_S}$, is stable across the different input choices. For completeness, Table 14 shows the effect of the final-state selection cuts on the different significance estimators for the *All variables* BDT configuration.

	ε_S	ε_B	$S/\sqrt{B}$	$S/\sqrt{S+B}$	$S/\sqrt{S+B+\sigma_S^2}$	BDT score cut
No cuts	0.648	0.200	39.236	38.751	4.959	0.835
(a)	0.665	0.227	37.619	37.202	4.955	0.835
(b)	0.686	0.242	37.632	37.228	4.955	0.825

Table 14: Signal and background efficiencies, significance metrics and optimal BDT score cuts for different selection scenarios (Table 8) for the *All variables* BDT configuration.

As a final validation step, it has been verified that variations in the BDT hyperparameters have a negligible impact on the overall performance, confirming the robustness of the analysis strategy and ensuring that the conclusions do not depend on a specific tuning choice.

Conclusions

The unique properties of the top quark, in particular its extremely short lifetime, allow its spin information to be directly transferred to the angular distributions of its decay products, providing direct access to its bare spin properties. The recent observation of entanglement in $t\bar{t}$ pairs by the ATLAS and CMS experiments marked the birth of a new research field, based on the application of quantum information concepts to fundamental particles at the highest achievable energies, thus opening the door to exploring quantum observables at colliders. In this context, this thesis has investigated spin correlations and quantum observables in $t\bar{t}$ production at the LHC at a center-of-mass energy of $\sqrt{s} = 13$ TeV, interpreting the $t\bar{t}$ pair as an ideal two-qubit system.

A primary achievement of this work is the implementation of a versatile analysis software within the Rivet framework, capable of reconstructing the spin density matrix in $t\bar{t}$ events in both the semileptonic and dileptonic decay channels at parton level. The reconstruction has been further extended to a realistic particle-level study for semileptonic final states, addressing both boosted and resolved topologies. Importantly, the routine is fully compatible with Monte Carlo simulations used by the ATLAS collaboration and directly interfaced with Pythia, ensuring that the analysis can be readily applied to realistic LHC simulation workflows and future experimental studies. The reconstruction has been validated against CMS measurements by comparing the extracted spin correlation coefficients and quantum magic results. Good agreement is observed both inclusively and in selected kinematic regions, confirming the expected enhancements in spin correlations near the high-energy and threshold regimes.

The framework has been applied to study the $t\bar{t}$ production threshold and the formation of the pseudo-bound state known as toponium. The effects of toponium formation on spin and quantum observables are investigated in dileptonic $t\bar{t}$ events at parton level, using both event-averaged and per-event variables and combining kinematic and spin related variables. Bound-state effects significantly alter the spin correlation matrix, with an enhancement of its diagonal elements and the entanglement measures $D^{(i)}$, while reducing quantum magic, M_2. Among per-event variables, kinematic observables display the strongest discriminating power. The angular separations ΔR and $\Delta\phi$ between the leptons, together with b_1, exhibit the highest separation performance, reflecting the particular angular correlations induced by bound-state formation. The variable p^* emerges as the most powerful single classifier in the $p^* < 35$ GeV region, where it is reliably modeled. In contrast, quantum information-inspired variables show lower individual performance, with $D^{(1)}_{\text{evt}}$ being the most disciminating. A new per-event observable, $\widetilde{M}_2^{\text{evt}}$, inspired by quantum magic, is introduced to enhance the sensitivity to the difference between

top-quark pair and toponium production in the tails of the angular distributions employed to reconstruct the spin density matrix. Although it performs better than M_2^{evt} in event-by-event discrimination, its overall separation power remains limited.

Correlation studies reveal that kinematic variables b_1, b_2, b_3 are highly correlated with each other and anti-correlated with ΔR and $\Delta\phi$, while exhibiting weak correlations with QI-inspired observables. Their combination in a BDT analysis significantly enhances the separation power between non-resonant $t\bar{t}$ and toponium samples compared to any single observable and several input variable configurations have been tested to quantify the relative impact of different sets of observables on the overall discriminating performance. It is observed that including p^* increases standard signal significances by 9.3% compared to BDTs trained without it, while QI-inspired variables bring a mild but not negligible improvement to the separation performance, adding a 3.3% relative to the configuration using only kinematic variables. Finally, the impact of final-state selections, chosen to emulate a realistic ATLAS analysis in the dilepton channel, has been evaluated on both individual observables and BDT score distributions, resulting in a global rescaling and a reduction in statistics, with only a moderate loss of the discriminating performance. The results shown for this part of the thesis constitute the core part of the paper *Extracting a Toponium Signal at the LHC with Spin and Quantum Information Tools*, published on arXiv `https://arxiv.org/abs/2602.23426v1`.

Overall, during the course of this thesis, a flexible and robust framework was developed for studying spin correlations and quantum observables in $t\bar{t}$ production at the LHC and is available on GitLab. The results obtained in the study of the top-quark pair production in the threshold region highlight the potential of combining kinematic and quantum-information-inspired observables to probe bound-state effects. The particle-level reconstruction in the semileptonic channel, developed for both boosted and resolved topologies, opens the way for future extensions of the toponium analysis, which to date has been studied exclusively in dileptonic events. Finally, this work provides a guide for future measurements by the ATLAS and CMS collaborations, where including detector effects, systematic uncertainties and potential BSM contributions will be essential to perform the measurement of toponium production.

Appendix

A Additional C_{ij} measurements

Measurements of the spin density matrices at parton level in the semileptonic channel are presented for different $m_{t\bar{t}}$ regions with $|\cos\theta| > 0.4$ (first and second row). The bottom row shows the results at particle level in the boosted topology for the boosted topology for $m_{t\bar{t}} > 800$ GeV and $|\cos\theta| < 0.4$ (left panel) as well as the inclusive correlation matrix obtained at parton level from the statistical combination of semileptonic and dileptonic measurements (right panel).

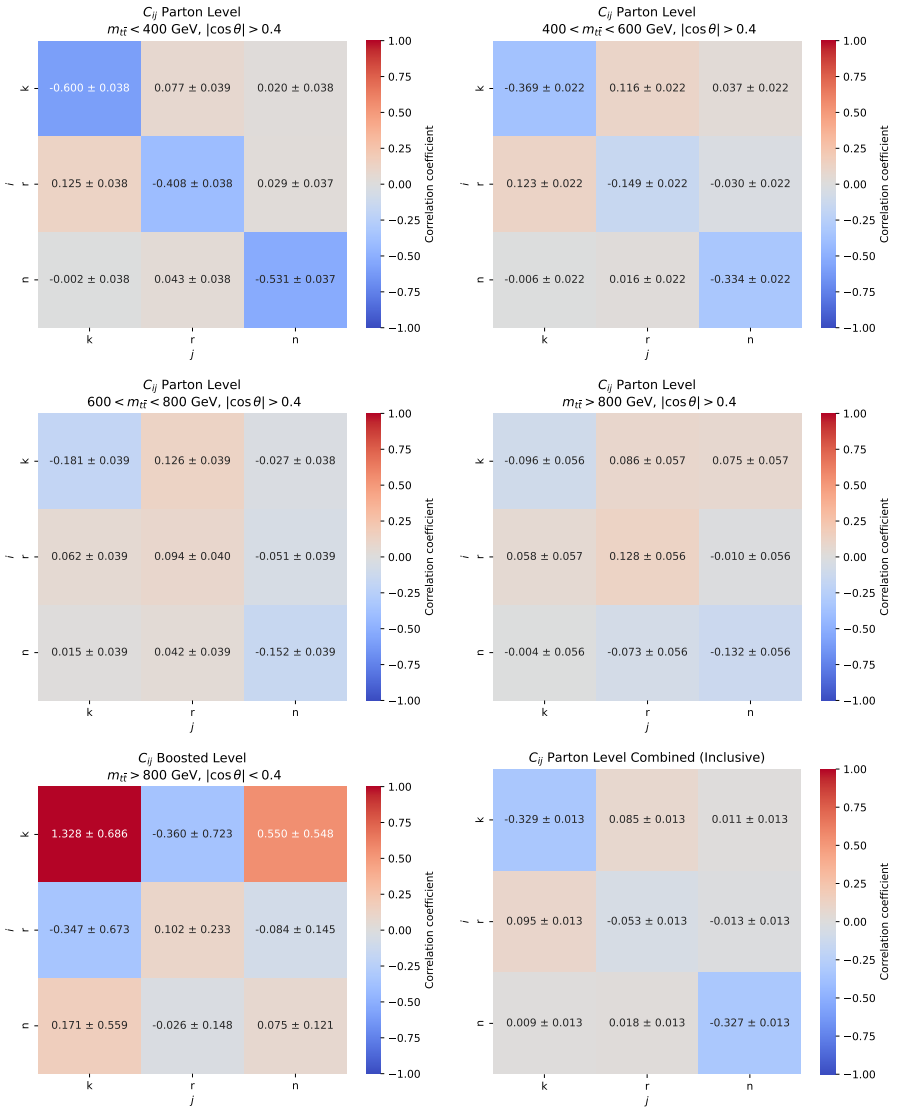

B XGBoost framework

The classifiers used in this work are implemented using the `XGBoost` framework [84], which stands for *eXtreme Gradient Boosting*. It is based on the gradient boosting method, which builds a strong classifier with prediction function $F(x)$ by sequentially adding weak decision trees,

$$F(x) = \sum_{m=1}^{M} \eta f_m(x; a_m), \tag{B.1}$$

where $f_m(x; a_m)$ represents the m-th decision tree with internal parameters a_m, η is the global learning rate and M is the total number of trees. The parameters a_m are determined by minimizing a loss function $\mathcal{L}(y, F(x))$, which quantifies the deviation between the model prediction and the true label y of the training sample. At each iteration m, a new decision tree $f_m(x)$ is trained to approximate the negative gradient of the loss function with respect to the current model prediction $F_{m-1}(x)$. This gradient indicates the direction in which the prediction should be modified to most effectively reduce the loss, such that each tree corrects the residual errors of the existing ensemble and the model iteratively improves. For the binary classification tasks in this analysis, the binary log-loss function is used:

$$\mathcal{L}(y_i, F(x_i)) = -\big[y_i \log \sigma(F(x_i)) + (1 - y_i) \log(1 - \sigma(F(x_i)))\big], \tag{B.2}$$

where $\sigma(F) = (1 + e^{-F})^{-1}$ is the sigmoid function. In this context, the model output $F(x)$ represents the logarithm of the signal-to-background ratio. The final output is transformed via $\sigma(F)$ into a probability-like score, where values closer to unity correspond to more signal-like events. The term *Extreme* in `XGBoost` refers to the inclusion of advanced features and optimizations, such as explicit regularization to reduce overfitting.

The performance and generalization of the `XGBoost` classifier depend on several hyperparameters controlling the model complexity. In particular, η and M determine the strength and number of boosting iterations, while the maximum tree depth limits the complexity of the individual learners. Additional regularization parameters are used to reduce overfitting and all hyperparameters are optimized on the training dataset.

C Single-variable correlation plots

Two-dimensional correlation plots of the single variables described in Section 4.4. The first and third columns show the results for toponium, whereas the second and fourth columns refer to conventional $t\bar{t}$ production. Each toponium plot is displayed alongside the corresponding $t\bar{t}$ plot.

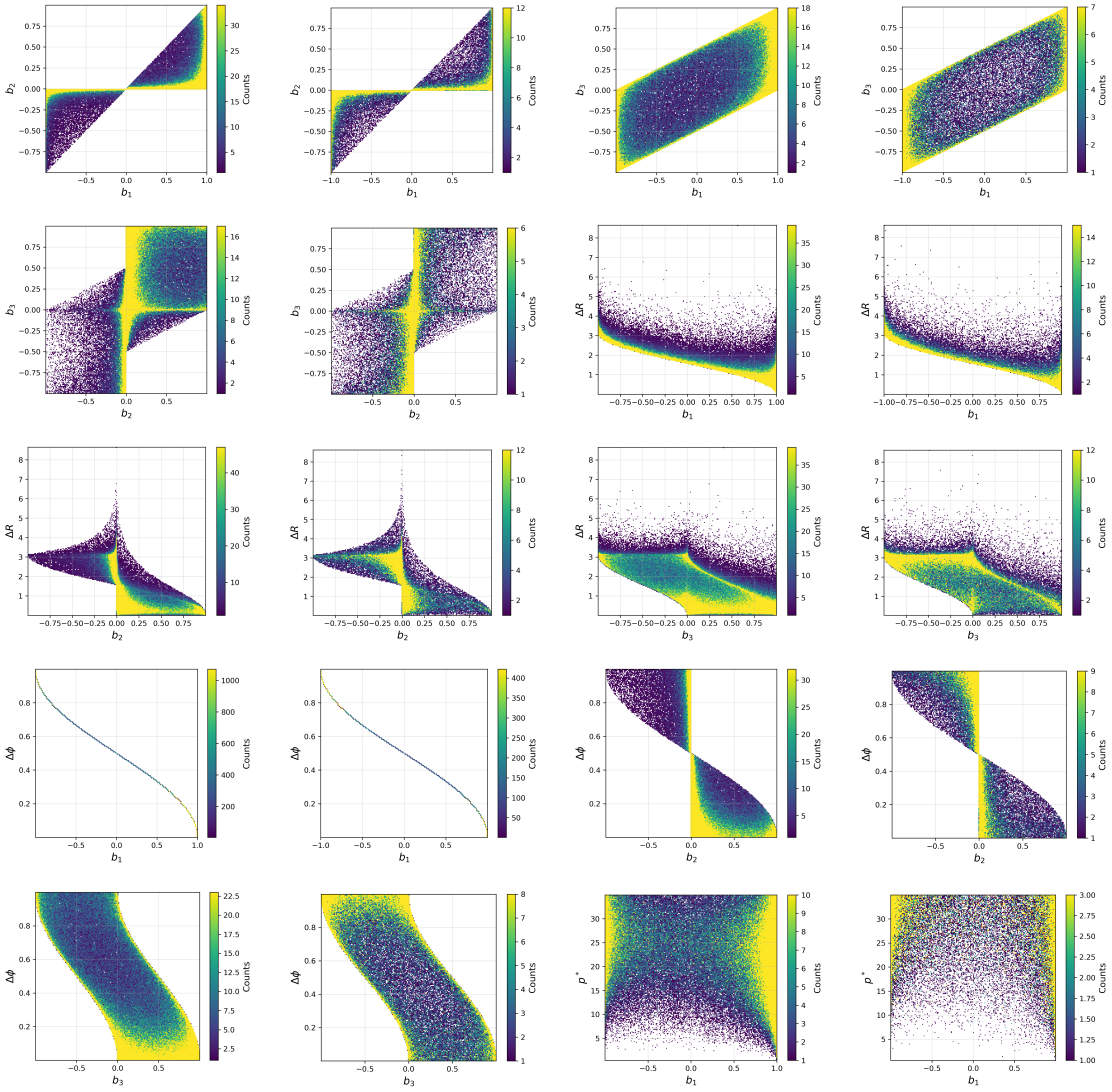

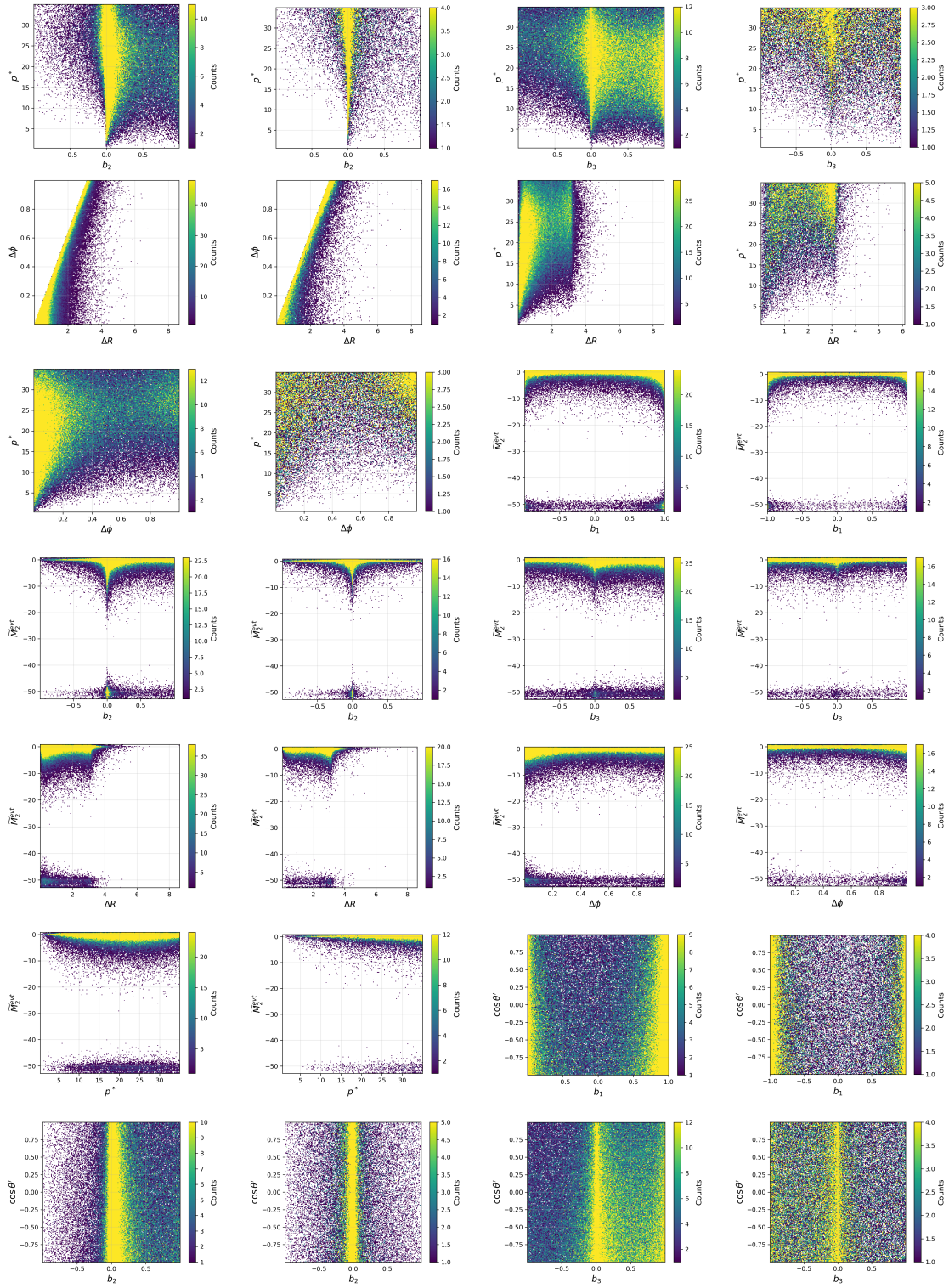
p*
b2
Counts
p*
b2
Counts
p*
b3
Counts
p*
b3
Counts
Δφ
ΔR
Counts
Δφ
ΔR
Counts
p*
ΔR
Counts
p*
ΔR
Counts
p*
Δφ
Counts
p*
Δφ
Counts
M̄2evt
b1
Counts
M̄2evt
b1
Counts
M̄2evt
b2
Counts
M̄2evt
b2
Counts
M̄2evt
b3
Counts
M̄2evt
b3
Counts
M̄2evt
ΔR
Counts
M̄2evt
ΔR
Counts
M̄2evt
Δφ
Counts
M̄2evt
Δφ
Counts
M̄2evt
p*
Counts
M̄2evt
p*
Counts
cos θ'
b1
Counts
cos θ'
b1
Counts
cos θ'
b2
Counts
cos θ'
b2
Counts
cos θ'
b3
Counts
cos θ'
b3
Counts

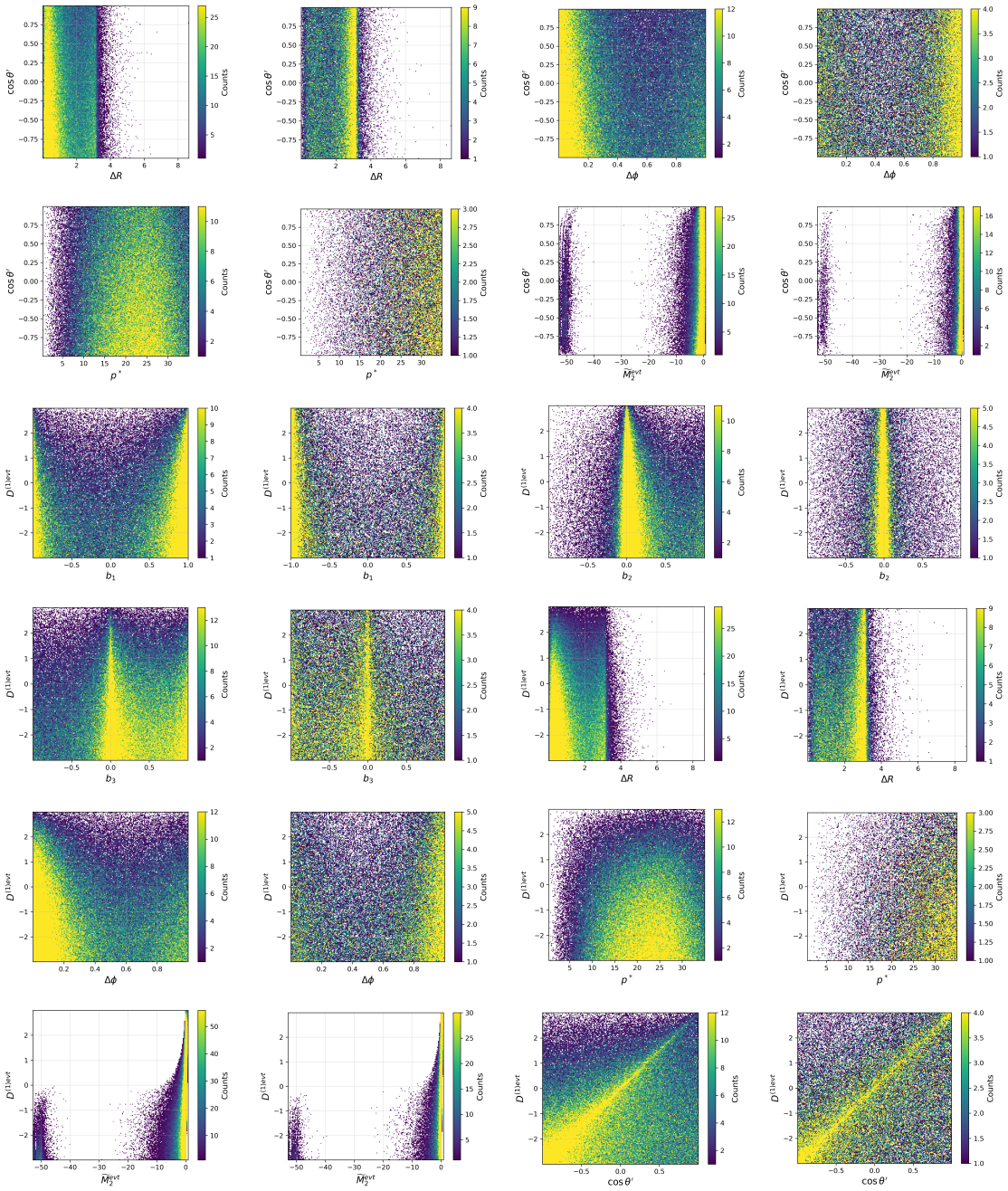
cos θ'
ΔR
Δφ
p*
M̄²evt
D(1)evt
b1
b2
b3
cos θ'
Counts

D BDT Score Distributions with final-state cuts

The BDT score distributions for the input variable configurations from Section 4.5.3 are reported below for different final-state selection selection scenarios taken from Table 8. From top to bottom, the plots correspond to the different input configurations (in order, *All variables*, *No* p^*, *No QI variables*, $D^{(1)\text{evt}} + \cos\theta'$), while from left to right they represent the applied selections: no cuts, selection (a) and selection (b).

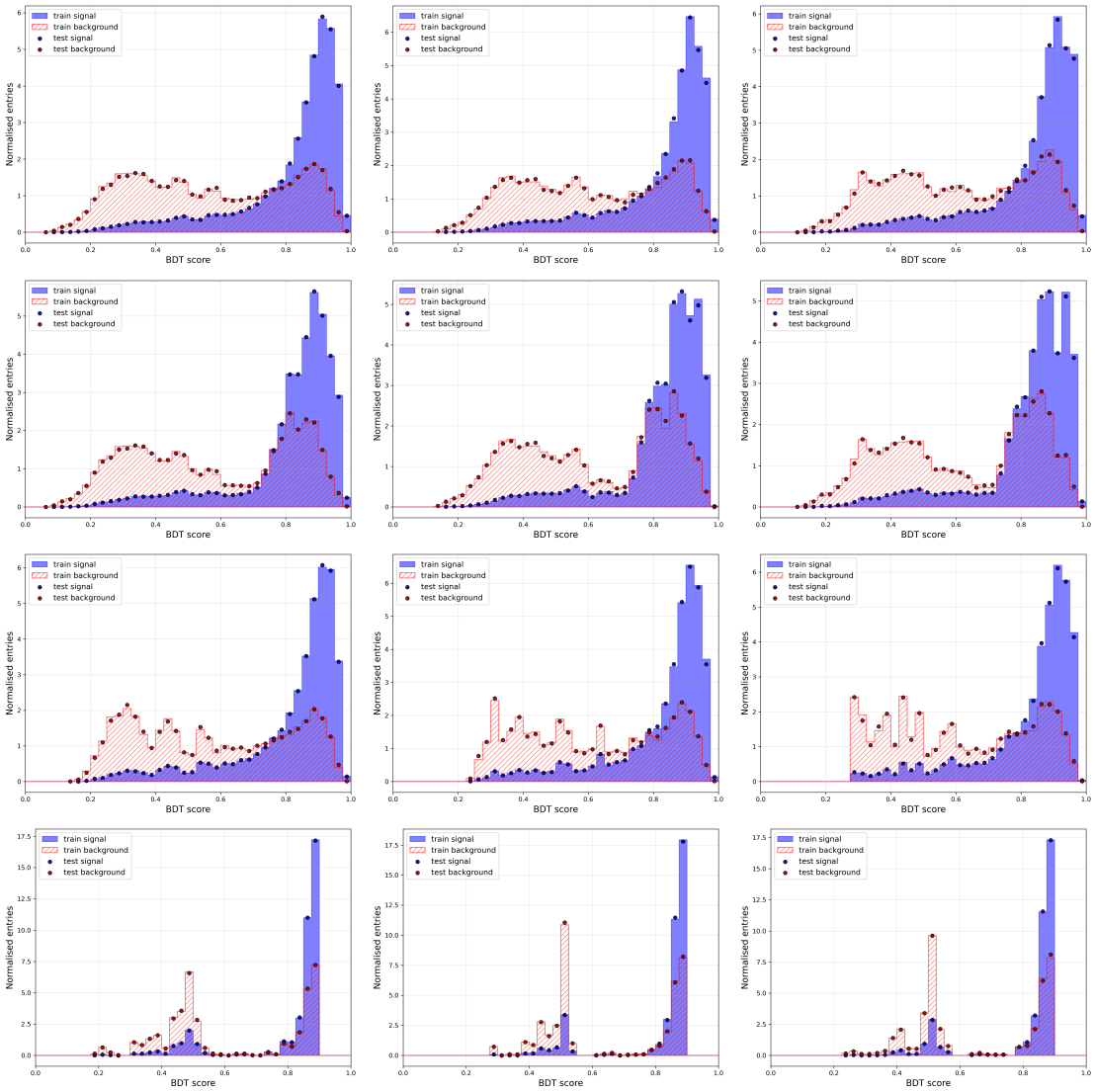

Acknowledgements

I would like to express my sincere gratitude to my supervisor, Federica Fabbri, for guiding me step by step throughout this journey with constant support and dedication. She always encouraged me to think critically and explore ideas with independence and confidence, helping me to believe in my abilities. Her passion for research and inspiring approach to challenges has been a constant source of motivation and has shaped my growth as both a person and a researcher.

I would also like to warmly thank my co-supervisor, Frédéric Déliot, for welcoming me to CEA and giving me the opportunity to truly experience the world of research in a different country and environment. His constant presence, support and contagious enthusiasm made me feel at home and inspired me as a researcher, helping me to make the most of this experience.

Infine, desidero ringraziare tutte le persone che amo e che mi hanno accompagnata in questo percorso, rendendolo davvero speciale. La mia famiglia, per tutto l'amore e il sostegno incondizionato. Martino, per essere stato al mio fianco in ogni momento. I miei amici di Parma - Ale, Lu, Diego, Edo, Richard, Brake, Fara e Pot - con cui ho condiviso tutto in questi anni. Gli amici di Bologna, che hanno reso questo periodo indimenticabile, con un grazie speciale a Martina e Lucia. Infine, tutti i miei amici di Salso e Fidenza, per essere sempre rimasti.
I ringraziamenti verranno implementati nella versione stampata :)

References

[1] S. Abachi et al. "Observation of the Top Quark". In: *Physical Review Letters* 74.14 (1995), pp. 2632–2637. DOI: 10.1103/PhysRevLett.74.2632.

[2] F. Abe et al. "Observation of Top Quark Production in $p\bar{p}$ Collisions with the Collider Detector at Fermilab". In: *Physical Review Letters* 74.14 (1973), pp. 2626–2631. DOI: 10.1103/PhysRevLett.74.2626.

[3] CMS Collaboration. *Measurements of $t\bar{t}$ Spin Correlations and Top-Quark Polarization Using Dilepton Final States in pp Collisions at $\sqrt{s} = 7$ TeV*. 2014. arXiv: 1311.3924 [hep-ex]. URL: https://arxiv.org/abs/1311.3924.

[4] ATLAS Collaboration. *Measurements of spin correlation in top-antitop quark events from proton-proton collisions at $\sqrt{s} = 7$ TeV using the ATLAS detector*. 2014. arXiv: 1407.4314 [hep-ex]. URL: https://arxiv.org/abs/1407.4314.

[5] ATLAS Collaboration. "Measurements of top quark spin observables in $t\bar{t}$ events using dilepton final states in $\sqrt{s} = 8$ TeV pp collisions with the ATLAS detector". In: *Journal of High Energy Physics* 2017.3 (2017). ISSN: 1029-8479. DOI: 10.1007/jhep03(2017)113. URL: http://dx.doi.org/10.1007/JHEP03(2017)113.

[6] CMS Collaboration. *Measurements of polarization and spin correlation and observation of entanglement in top quark pairs using lepton+jets events from proton-proton collisions at $\sqrt{s} = 13$ TeV*. 2024. arXiv: 2409.11067 [hep-ex]. URL: https://arxiv.org/abs/2409.11067.

[7] CMS Collaboration. *Measurement of the top quark polarization and spin correlations using dilepton final states in proton-proton collisions at 13 TeV*. 2019. arXiv: 1907.03729 [hep-ex]. URL: https://arxiv.org/abs/1907.03729.

[8] ATLAS Collaboration. "Observation of quantum entanglement with top quarks at the ATLAS detector". In: *Nature* 633.8030 (Sept. 2024), pp. 542–547. ISSN: 1476-4687. DOI: 10.1038/s41586-024-07824-z. URL: http://dx.doi.org/10.1038/s41586-024-07824-z.

[9] CMS Collaboration. "Observation of quantum entanglement in top quark pair production in proton–proton collisions at $\sqrt{s} = 13$ TeV". In: *Reports on Progress in Physics* 87.11 (Oct. 2024), p. 117801. DOI: 10.1088/1361-6633/ad7e4d. URL: https://doi.org/10.1088/1361-6633/ad7e4d.

[10] *Observation of magic states of top quark pairs produced in proton-proton collisions at* $\sqrt{s} = 13$ TeV. Tech. rep. Geneva: CERN, 2025. URL: https://cds.cern.ch/record/2926751.

[11] CMS Collaboration. "Differential cross section measurements for the production of top quark pairs and of additional jets using dilepton events from pp collisions at $\sqrt{s} = 13$ TeV". In: *Journal of High Energy Physics* 2025.2 (Feb. 2025). ISSN: 1029-8479. DOI: 10.1007/jhep02(2025)064. URL: http://dx.doi.org/10.1007/JHEP02(2025)064.

[12] ATLAS Collaboration. "Inclusive and differential cross-sections for dilepton $t\bar{t}$ production measured in $\sqrt{s} = 13$ TeV pp collisions with the ATLAS detector". In: *Journal of High Energy Physics* 2023.7 (July 2023). ISSN: 1029-8479. DOI: 10.1007/jhep07(2023)141. URL: http://dx.doi.org/10.1007/JHEP07(2023)141.

[13] Benjamin Fuks, Kaoru Hagiwara, Kai Ma, and Ya-Juan Zheng. "Simulating toponium formation signals at the LHC". In: *The European Physical Journal C* 85.2 (2025), p. 157. DOI: 10.1140/epjc/s10052-025-13853-3. arXiv: 2411.18962 [hep-ph].

[14] Fabio Maltoni, Claudio Severi, Simone Tentori, and Eleni Vryonidou. *Quantum detection of new physics in top-quark pair production at the LHC*. 2024. arXiv: 2401.08751 [hep-ph]. URL: https://arxiv.org/abs/2401.08751.

[15] CMS Collaboration. "Observation of a pseudoscalar excess at the top quark pair production threshold". In: *Reports on Progress in Physics* 88.8 (Aug. 2025), p. 087801. ISSN: 1361-6633. DOI: 10.1088/1361-6633/adf7d3. URL: http://dx.doi.org/10.1088/1361-6633/adf7d3.

[16] ATLAS Collaboration. *Observation of a cross-section enhancement near the* $t\bar{t}$ *production threshold in* $\sqrt{s} = 13$ *TeV pp collisions with the ATLAS detector*. 2026. arXiv: 2601.11780 [hep-ex]. URL: https://arxiv.org/abs/2601.11780.

[17] ATLAS Collaboration. "Observation of a new particle in the search for the Standard Model Higgs boson with the ATLAS detector at the LHC". In: *Physics Letters B* 716.1 (Sept. 2012), pp. 1–29. ISSN: 0370-2693. DOI: 10.1016/j.physletb.2012.08.020. URL: http://dx.doi.org/10.1016/j.physletb.2012.08.020.

[18] Murray Gell-Mann. "A Schematic Model of Baryons and Mesons". In: *Phys. Lett.* 8 (1964), pp. 214–215. DOI: 10.1016/S0031-9163(64)92001-3.

[19] G. Zweig. "An SU(3) model for strong interaction symmetry and its breaking. Version 1". In: (Jan. 1964). DOI: 10.17181/CERN-TH-401.

[20] Henry W. Kendall. "Deep inelastic scattering: Experiments on the proton and the observation of scaling". In: *Rev. Mod. Phys.* 63 (3 July 1991), pp. 597–614. DOI: 10.1103/RevModPhys.63.597. URL: https://link.aps.org/doi/10.1103/RevModPhys.63.597.

[21] J. -E. Augustin et al. "Discovery of a Narrow Resonance in e^+e^- Annihilation". In: *Phys. Rev. Lett.* 33 (23 Dec. 1974), pp. 1406–1408. DOI: 10.1103/PhysRevLett.33.1406. URL: https://link.aps.org/doi/10.1103/PhysRevLett.33.1406.

[22] J. J. Aubert et al. "Experimental Observation of a Heavy Particle J". In: *Phys. Rev. Lett.* 33 (23 Dec. 1974), pp. 1404–1406. DOI: 10.1103/PhysRevLett.33.1404. URL: https://link.aps.org/doi/10.1103/PhysRevLett.33.1404.

[23] W. R. Innes et al. "Observation of Structure in the Υ Region". In: *Phys. Rev. Lett.* 39 (20 Nov. 1977), pp. 1240–1242. DOI: 10.1103/PhysRevLett.39.1240. URL: https://link.aps.org/doi/10.1103/PhysRevLett.39.1240.

[24] Sheldon L. Glashow. "Partial-symmetries of weak interactions". In: *Nuclear Physics* 22.4 (1961), pp. 579–588. ISSN: 0029-5582. DOI: https://doi.org/10.1016/0029-5582(61)90469-2. URL: https://www.sciencedirect.com/science/article/pii/0029558261904692.

[25] Steven Weinberg. "A Model of Leptons". In: *Phys. Rev. Lett.* 19 (21 Nov. 1967), pp. 1264–1266. DOI: 10.1103/PhysRevLett.19.1264. URL: https://link.aps.org/doi/10.1103/PhysRevLett.19.1264.

[26] Abdus Salam. "Weak and Electromagnetic Interactions". In: *Conf. Proc. C* 680519 (1968), pp. 367–377. DOI: 10.1142/9789812795915_0034.

[27] Matthew D. Schwartz. *Quantum Field Theory and the Standard Model*. Cambridge University Press, 2013. ISBN: 9781107034730.

[28] Nicola Cabibbo. "Unitary Symmetry and Leptonic Decays". In: *Phys. Rev. Lett.* 10 (12 June 1963), pp. 531–533. DOI: 10.1103/PhysRevLett.10.531. URL: https://link.aps.org/doi/10.1103/PhysRevLett.10.531.

[29] Makoto Kobayashi and Toshihide Maskawa. "CP-Violation in the Renormalizable Theory of Weak Interaction". In: *Progress of Theoretical Physics* 49.2 (1973), pp. 652–657. DOI: 10.1143/PTP.49.652.

[30] S. Navas et al. "Review of Particle Physics". In: *Physical Review D* 110.3 (2024), p. 030001. DOI: 10.1103/PhysRevD.110.030001.

[31] John C. Collins, Davison E. Soper, and George Sterman. *Factorization of Hard Processes in QCD*. 2004. arXiv: hep-ph/0409313 [hep-ph]. URL: https://arxiv.org/abs/hep-ph/0409313.

[32] NNPDF Collaboration. "Parton distributions from high-precision collider data: NNPDF Collaboration". In: *The European Physical Journal C* 77.10 (Oct. 2017). ISSN: 1434-6052. DOI: 10.1140/epjc/s10052-017-5199-5. URL: http://dx.doi.org/10.1140/epjc/s10052-017-5199-5.

[33] Michał Czakon and Alexander Mitov. "Top++: A program for the calculation of the top-pair cross-section at hadron colliders". In: *Computer Physics Communications* 185.11 (Nov. 2014), pp. 2930–2938. ISSN: 0010-4655. DOI: 10.1016/j.cpc.2014.06.021. URL: http://dx.doi.org/10.1016/j.cpc.2014.06.021.

[34] ATLAS and CMS Collaborations. "Combination of inclusive top-quark pair production cross-section measurements using ATLAS and CMS data at $\sqrt{s} =$ 7 and 8 TeV". In: *Journal of High Energy Physics* 2023.7 (July 2023). ISSN: 1029-8479. DOI: 10.1007/jhep07(2023)213. URL: http://dx.doi.org/10.1007/JHEP07(2023)213.

[35] ATLAS Collaboration. "Measurement of the $t\bar{t}$ production cross-section in the lepton+jets channel at $\sqrt{s} = 13$ TeV with the ATLAS experiment". In: *Physics Letters B* 810 (Nov. 2020), p. 135797. ISSN: 0370-2693. DOI: 10.1016/j.physletb.2020.135797. URL: http://dx.doi.org/10.1016/j.physletb.2020.135797.

[36] ATLAS Collaboration. *ATLAS Public Physics Notes*. https://atlas.web.cern.ch/Atlas/GROUPS/PHYSICS/PUBNOTES/ATL-PHYS-PUB-2025-024/. 2026.

[37] Stefano Frixione, Eric Laenen, Patrick Motylinski, Chris White, and Bryan R. Webber. "Single-top hadroproduction in association with a W boson". In: *Journal of High Energy Physics* 2008.07 (July 2008), p. 029. DOI: 10.1088/1126-6708/2008/07/029. URL: https://doi.org/10.1088/1126-6708/2008/07/029.

[38] Victor S. Fadin and Valery A. Khoze. "Threshold Behavior of Heavy Top Production in e+ e- Collisions". In: *JETP Lett.* 46 (1987), pp. 525–529.

[39] Y. Kiyo, J. H. Kühn, S. Moch, M. Steinhauser, and P. Uwer. "Top-quark pair production near threshold at LHC". In: *The European Physical Journal C* 60.3 (Feb. 2009), pp. 375–386. ISSN: 1434-6052. DOI: 10.1140/epjc/s10052-009-0892-7. URL: http://dx.doi.org/10.1140/epjc/s10052-009-0892-7.

[40] Kaoru Hagiwara, Yukinari Sumino, and Hiroshi Yokoya. "Bound-state effects on top quark production at hadron colliders". In: *Physics Letters B* 666.1 (2008), pp. 71–76. ISSN: 0370-2693. DOI: https://doi.org/10.1016/

j.physletb.2008.07.006. URL: https://www.sciencedirect.com/science/article/pii/S0370269308008046.

[41] Benjamin Fuks. *Toponium physics at the Large Hadron Collider*. 2025. arXiv: 2505.03869 [hep-ph]. URL: https://arxiv.org/abs/2505.03869.

[42] Benjamin Fuks, Kaoru Hagiwara, Kai Ma, and Ya-Juan Zheng. "Signatures of toponium formation in LHC run 2 data". In: *Physical Review D* 104.3 (Aug. 2021). ISSN: 2470-0029. DOI: 10.1103/physrevd.104.034023. URL: http://dx.doi.org/10.1103/PhysRevD.104.034023.

[43] ATLAS Collaboration. "The ATLAS Experiment at the CERN Large Hadron Collider". In: *Journal of Instrumentation* 3.08 (Aug. 2008), S08003. DOI: 10.1088/1748-0221/3/08/S08003. URL: https://doi.org/10.1088/1748-0221/3/08/S08003.

[44] Michael A. Nielsen and Isaac L. Chuang. *Quantum Computation and Quantum Information: 10th Anniversary Edition*. Cambridge University Press, 2010. DOI: 10.1017/CBO9780511976667.

[45] Rafael Aoude, Eric Madge, Fabio Maltoni, and Luca Mantani. "Probing new physics through entanglement in diboson production". In: (July 2023). DOI: 10.48550/arXiv.2307.09675. arXiv: 2307.09675 [hep-ph].

[46] John S. Bell. "On the Einstein Podolsky Rosen paradox". In: *Physics* 1.3 (1964), pp. 195–200. DOI: 10.1103/PhysicsPhysiqueFizika.1.195.

[47] Alain Aspect, Philippe Grangier, and Gérard Roger. "Experimental Realization of Einstein-Podolsky-Rosen-Bohm Gedankenexperiment: A New Violation of Bell's Inequalities". In: *Physical Review Letters* 49.2 (1982), pp. 91–94. DOI: 10.1103/PhysRevLett.49.91.

[48] Asher Peres. "Separability Criterion for Density Matrices". In: *Physical Review Letters* 77 (1996), pp. 1413–1415. DOI: 10.1103/PhysRevLett.77.1413. arXiv: quant-ph/9604005 [quant-ph].

[49] Paweł Horodecki. "Separability criterion and inseparable mixed states with positive partial transposition". In: *Physics Letters A* 232.5 (1997), pp. 333–339. DOI: 10.1016/S0375-9601(97)00416-7. arXiv: quant-ph/9703004 [quant-ph].

[50] Ryszard Horodecki, Paweł Horodecki, Michał Horodecki, and Karol Horodecki. "Quantum entanglement". In: *Reviews of Modern Physics* 81.2 (2009), pp. 865–942. DOI: 10.1103/RevModPhys.81.865. arXiv: quant-ph/0702225 [quant-ph].

[51] Yoav Afik and Juan Ramón Muñoz de Nova. "Entanglement and quantum tomography with top quarks at the LHC". In: *European Physical Journal Plus* 136.9 (2021), p. 907. DOI: 10.1140/epjp/s13360-021-01902-1. arXiv: 2003.02280 [quant-ph].

[52] Peter W. Shor. "Polynomial-Time Algorithms for Prime Factorization and Discrete Logarithms on a Quantum Computer". In: *SIAM Journal on Computing* 26.5 (1997), pp. 1484–1509. DOI: 10.1137/S0097539795293172. URL: https://doi.org/10.1137/S0097539795293172.

[53] Daniel Gottesman. *The Heisenberg Representation of Quantum Computers*. 1998. arXiv: quant-ph/9807006 [quant-ph]. URL: https://arxiv.org/abs/quant-ph/9807006.

[54] Lorenzo Leone, Salvatore F. E. Oliviero, and Alioscia Hamma. "Stabilizer Rényi Entropy". In: *Physical Review Letters* 128.5 (Feb. 2022). ISSN: 1079-7114. DOI: 10.1103/physrevlett.128.050402. URL: http://dx.doi.org/10.1103/PhysRevLett.128.050402.

[55] Valentin Durupt, Fabio Maltoni, and Olivier Mattelaer. *Automated computation of spin-density matrices and quantum observables for collider physics*. 2025. arXiv: 2510.17730 [hep-ph]. URL: https://arxiv.org/abs/2510.17730.

[56] Matthew Baumgart and Brock Tweedie. "A New Twist on Top Quark Spin Correlations". In: *JHEP* 03 (2013), p. 117. DOI: 10.1007/JHEP03(2013)117. arXiv: 1212.4888 [hep-ph].

[57] W. Bernreuther, A. Brandenburg, Z. G. Si, and P. Uwer. "Top quark pair production and decay at hadron colliders". In: *Nucl. Phys. B* 690 (2004), pp. 81–137. DOI: 10.1016/j.nuclphysb.2004.04.019. arXiv: hep-ph/0403035 [hep-ph].

[58] Werner Bernreuther and Zong-Guo Si. "Distributions and correlations for top quark pair production and decay at the Tevatron and LHC". In: *Nucl. Phys. B* 837 (2010), pp. 90–121. DOI: 10.1016/j.nuclphysb.2010.05.001. arXiv: 1003.3926 [hep-ph].

[59] J. A. Aguilar-Saavedra and J. A. Casas. "Improved tests of entanglement and Bell inequalities with LHC tops". In: *The European Physical Journal C* 82.8 (Aug. 2022). ISSN: 1434-6052. DOI: 10.1140/epjc/s10052-022-10630-4. URL: http://dx.doi.org/10.1140/epjc/s10052-022-10630-4.

[60] Zhongtian Dong, Dorival Gonçalves, Kyoungchul Kong, and Alberto Navarro. "When the Machine Chimes the Bell: Entanglement and Bell Inequalities with Boosted $t\bar{t}$". In: *Physical Review D* 109.11 (June 2024). ISSN: 2470-0029. DOI: 10.1103/physrevd.109.115023. URL: http://dx.doi.org/10.1103/PhysRevD.109.115023.

[61] Chris D. White and Martin J. White. *The magic of entangled top quarks*. 2024. arXiv: 2406.07321 [hep-ph]. URL: https://arxiv.org/abs/2406.07321.

[62] D0 Collaboration. *Measurement of Spin Correlation in $t\bar{t}$ Production Using a Matrix Element Approach*. 2011. arXiv: 1104.5194 [hep-ex]. URL: https://arxiv.org/abs/1104.5194.

[63] D0 Collaboration. *Measurement of spin correlation in $t\bar{t}$ production using dilepton final states*. 2011. arXiv: 1103.1871 [hep-ex]. URL: https://arxiv.org/abs/1103.1871.

[64] D0 Collaboration. *Evidence for spin correlation in $t\bar{t}$ production*. 2012. arXiv: 1110.4194 [hep-ex]. URL: https://arxiv.org/abs/1110.4194.

[65] CDF Collaboration. *Measurement of $t\bar{t}$ spin correlation in $p\bar{p}$ collisions using the CDF II detector at the Tevatron*. 2011. arXiv: 1012.3093 [hep-ex]. URL: https://doi.org/10.48550/arXiv.1012.3093.

[66] ATLAS Collaboration. *Observation of Spin Correlation in $t\bar{t}$ Events from pp Collisions at $\sqrt{s} = 7$ TeV Using the ATLAS Detector*. 2012. arXiv: 1203.4081 [hep-ex]. URL: https://arxiv.org/abs/1203.4081.

[67] ATLAS Collaboration. *Measurements of top-quark pair spin correlations in the $e\mu$ channel at $\sqrt{s} = 13$ TeV using pp collisions in the ATLAS detector*. 2020. arXiv: 1903.07570 [hep-ex]. URL: https://arxiv.org/abs/1903.07570.

[68] Stefano Frixione, Giovanni Ridolfi, and Paolo Nason. "A positive-weight next-to-leading-order Monte Carlo for heavy flavour hadroproduction". In: *Journal of High Energy Physics* 2007.09 (Sept. 2007), p. 126. DOI: 10.1088/1126-6708/2007/09/126. URL: https://doi.org/10.1088/1126-6708/2007/09/126.

[69] Paolo Nason. "A New Method for Combining NLO QCD with Shower Monte Carlo Algorithms". In: *Journal of High Energy Physics* 2004.11 (Nov. 2004), pp. 040–040. ISSN: 1029-8479. DOI: 10.1088/1126-6708/2004/11/040. URL: http://dx.doi.org/10.1088/1126-6708/2004/11/040.

[70] Simone Alioli, Paolo Nason, Carlo Oleari, and Emanuele Re. "A general framework for implementing NLO calculations in shower Monte Carlo programs: the POWHEG BOX". In: *Journal of High Energy Physics* 2010.6 (June 2010). ISSN: 1029-8479. DOI: 10.1007/jhep06(2010)043. URL: http://dx.doi.org/10.1007/JHEP06(2010)043.

[71] Torbjörn Sjöstrand et al. "An introduction to PYTHIA 8.2". In: *Comput. Phys. Commun.* 191 (2015), pp. 159–177. DOI: 10.1016/j.cpc.2015.01.024. arXiv: 1410.3012 [hep-ph].

[72] Christian Bierlich et al. "Robust independent validation of experiment and theory: Rivet version 4 release note". In: *SciPost Phys. Codeb.* 36 (2024), p. 1. DOI: 10.21468/SciPostPhysCodeb.36. arXiv: 2404.15984 [hep-ph].

[73] R. Brun and F. Rademakers. "ROOT — An object oriented data analysis framework". In: *Nucl. Instrum. Meth. A* 389 (1997), pp. 81–86. DOI: 10.1016/S0168-9002(97)00048-X.

[74] Matteo Cacciari, Gavin P. Salam, and Gregory Soyez. "The anti-k_t jet clustering algorithm". In: *Journal of High Energy Physics* 2008.04 (2008), p. 063. DOI: 10.1088/1126-6708/2008/04/063. arXiv: 0802.1189 [hep-ph].

[75] CMS Collaboration. "Measurement of the W boson helicity fractions in the decays of top quark pairs to lepton + jets final states produced in pp collisions at $\sqrt{s} = 8$ TeV". In: *Physics Letters B* 762 (2016). CERN-EP-2016-118, CMS-TOP-13-008, pp. 512–534. DOI: 10.1016/j.physletb.2016.10.007. arXiv: 1605.09047 [hep-ex].

[76] Brock Tweedie. "Better Hadronic Top Quark Polarimetry". In: *Physical Review D* 90.9 (2014). PITT PACC 1315, p. 094010. DOI: 10.1103/PhysRevD.90.094010. arXiv: 1401.3021 [hep-ph].

[77] Zhongtian Dong, Dorival Gonçalves, Kyoungchul Kong, Andrew J. Larkoski, and Alberto Navarro. "Hadronic Top Quark Polarimetry with ParticleNet". In: (2024). 7 pages, 3 figures. DOI: 10.48550/arXiv.2407.01663. arXiv: 2407.01663 [hep-ph].

[78] J. Alwall et al. "The automated computation of tree-level and next-to-leading order differential cross sections, and their matching to parton shower simulations". In: *JHEP* 07 (2014), p. 079. DOI: 10.1007/JHEP07(2014)079. arXiv: 1405.0301 [hep-ph].

[79] Andy Buckley et al. "The HepMC3 event record library for Monte Carlo event generators". In: *Computer Physics Communications* 260 (Mar. 2021), p. 107310. ISSN: 0010-4655. DOI: 10.1016/j.cpc.2020.107310. URL: http://dx.doi.org/10.1016/j.cpc.2020.107310.

[80] ATLAS Collaboration. "The ATLAS Experiment at the CERN Large Hadron Collider". In: *Journal of Instrumentation* 3.08 (Aug. 2008), S08003. DOI: 10.1088/1748-0221/3/08/S08003. URL: https://doi.org/10.1088/1748-0221/3/08/S08003.

[81] Benjamin Fuks, Kaoru Hagiwara, Kai Ma, Léandre Munoz-Aillaud, and Ya-Juan Zheng. *Prospects for toponium formation at the LHC in the single-lepton mode*. 2025. arXiv: 2509.03596 [hep-ph]. URL: https://arxiv.org/abs/2509.03596.

[82] John F. Gunion, Bohdan Grzadkowski, and Xiao-Gang He. "Determining the top-antitop and ZZ Couplings of a Neutral Higgs Boson of Arbitrary CP Nature at the NLC". In: *Physical Review Letters* 77.26 (Dec. 1996), pp. 5172–5175. ISSN: 1079-7114. DOI: 10.1103/physrevlett.77.5172. URL: http://dx.doi.org/10.1103/PhysRevLett.77.5172.

[83] Duarte Azevedo, Rodrigo Capucha, António Onofre, and Rui Santos. "CP-violation, asymmetries and interferences in $t\bar{t}\phi$". In: *Journal of High Energy Physics* 2022.9 (Sept. 2022). ISSN: 1029-8479. DOI: 10.1007/jhep09(2022)246. URL: http://dx.doi.org/10.1007/JHEP09(2022)246.

[84] Tianqi Chen and Carlos Guestrin. "XGBoost: A Scalable Tree Boosting System". In: *arXiv e-prints* (2016). DOI: 10.48550/arXiv.1603.02754. arXiv: 1603.02754 [cs.LG].